

# **Design, Analysis and Implementation of Bi- Directional DC-DC Converter for HESS in DC Microgrid Applications**

Thesis

Submitted in partial fulfilment of requirements  
for the award of the degree of

**Doctor of Philosophy**  
**in**  
**Electrical Engineering**

by

**Punna Srinivas**

**(Roll No. 717014)**

Under the supervision of

**Dr. Udaya Bhasker Manthati**

Assistant Professor



**Department of Electrical Engineering**  
**National Institute of Technology, Warangal**  
**(An Institute of National Importance)**  
**Warangal - 506 004, Telangana State, India**  
**September-2021**

## **APPROVAL SHEET**

This Thesis entitled **“Design, Analysis and Implementation of Bi-Directional DC-DC Converter for HESS in DC Microgrid Applications”** by **Mr. Punna Srinivas** is approved for the degree of Doctor of Philosophy

### **Examiners**

---

---

### **Supervisor**

**Dr. Udaya Bhasker Manthati**

Assistant Professor

EED, NIT Warangal

### **Chairman**

**Prof. D. M. Vinod Kumar**

Professor,

Department of Electrical Engineering,

NIT Warangal

**Date:** \_\_\_\_\_

**DEPARTMENT OF ELECTRICAL ENGINEERING  
NATIONAL INSTITUTE OF TECHNOLOGY  
WARANGAL – 506 004, TELANGANA, INDIA**

**DEPARTMENT OF ELECTRICAL ENGINEERING  
NATIONAL INSTITUTE OF TECHNOLOGY WARANGAL**



**CERTIFICATE**

This is to certify that the dissertation work entitled "**Design, Analysis and Implementation of Bi-Directional DC-DC Converter for HESS in DC Microgrid Applications**", which is being submitted by **Mr. Punna Srinivas** (Roll No: 717014), is a bonafide work submitted to National Institute of Technology, Warangal in partial fulfilment of the requirement for the award of the degree of **Doctor of Philosophy** in Electrical Engineering. To the best of my knowledge, the work incorporated in this thesis has not been submitted elsewhere for the award of any degree.

**Dr. Udaya Bhasker Manthati**

(Supervisor)

Assistant Professor

Department of Electrical Engineering  
National Institute of Technology  
Warangal – 506004

Date:

Place: NIT Warangal

## DECLARATION

This is to certify that the work presented in the thesis entitled "**Design, Analysis and Implementation of Bi-Directional DC-DC Converter for HESS in DC Microgrid Applications**" is a bonafide work done by me under the supervision of **Dr. Udaya Bhasker Mathati**, Assistant Professor, Department of Electrical Engineering, National Institute of Technology, Warangal, India and was not submitted elsewhere for the award of any degree.

I declare that this written submission represents my ideas in my own words and where others ideas or words have been included, I have adequately cited and referenced the original sources. I also declare that I have adhered to all principles of academic honesty and integrity and have not misrepresented or fabricated or falsified any idea/data/fact/source in my submission. I understand that any violation of the above will be a cause for disciplinary action by the Institute and can also evoke penal action from the sources which have thus not been properly cited or from whom proper permission has not been taken when needed.

**Punna Srinivas**  
**(Roll No: 717014)**

Date:

Place: NIT Warangal

## ACKNOWLEDGEMENTS

It gives me immense pleasure to express my deep sense of gratitude and thanks to my supervisor **Dr. Udaya Bhasker Manthati**, Assistant Professor, Department of Electrical Engineering, National Institute of Technology Warangal, for his valuable guidance, support and suggestions. His knowledge, suggestions, and discussions helped me to become a capable researcher. He has shown me the interesting side of this wonderful and potential research area. His encouragement helped me to overcome the difficulties encountered in my research as well in my personal life.

I am very much thankful to **Prof. D. M. Vinod kumar**, Chairman of DSC, Department of Electrical Engineering for his constant technical suggestions, encouragement, support and cooperation.

I wish to express my sincere thanks to **Prof. N.V. Ramana Rao**, Director, NIT Warangal for his official support and encouragement.

I take this privilege to thank all my DSC Committee members, **Prof. N. Viswanathan**, Department of Electrical Engineering, **Dr. D. Sreenivasarao**, Assistant Professor, Department of Electrical Engineering and **Dr. J. Ravi kumar**, Associate Professor, Department of Electronics and communication Engineering for their detailed technical review, constructive suggestions and excellent advice during the progress of this research work.

I am very much thankful to **Prof. M. Sailaja Kumari**, Head, Department of Electrical Engineering for her constant encouragement, support and cooperation.

I also appreciate the encouragement from teaching, non-teaching members and fraternity of Department of Electrical Engineering of NIT Warangal. They have always been encouraging and supportive.

I convey my special thanks to contemporary Research Scholars Arun Kumar C.R, Sumon Dhara, Madhu babu, C. Srinivasarathnam, Anil kumar, Laxman, S. Ramkumar, V.V.K Satyakar, K. Sateesh kumar, Y. Bhaskar S. S. Gupta, K Hema Sundara Rao, A Anil Kumar, B Kiran Babu, A. Pranay Kumar, M. Santhosh, T. Ratna Rahul, Dr. Sachidananda

Prasad, Dr. V. Venkata Ramana, Dr. N V Phanendra Babu, B. Durga Hari Kiran, Siva Prasad (ECE), and also to Power Electronic and Drives M.Tech Students Rajanikanth Puli, Akhil.

I acknowledge my gratitude to co-scholars at NIT Warangal for their moral support and technical suggestions.

I acknowledge my gratitude to all my teachers and colleagues at various places for supporting and encouraging me to complete the work.

Finally, I render my respect to all my family members (my wife Jyothi, mother Smt. Laxmamma, my father-in-law G. Chandrashekhar for giving me moral support and inspiration. They have motivated and helped me to complete my thesis work successfully.

**Punna Srinivas**

## ABSTRACT

This thesis studies various types of bidirectional converters and control schemes for hybrid energy storage systems (HESS). The proposed converters and control scheme are applied to the HESS standalone mode of operation. The main focus is on designing a controller for better DC grid voltage recovery for efficient power balance between PV output and load interruptions using battery and supercapacitor (SC).

During the past decades, in modern electric grid system easy integration with renewable energy sources (RESs), energy storage systems (ESSs) and electric load is an attractive technology of DC microgrid. The wind and photovoltaic (PV) power generations are most popular RESs. Intermittent nature is the main issue regarding these RESs. By varying environmental conditions power generation from RESs changes. As per the best RESs the solar power generation is most economical, clean and green energy. The continuous load power demand, microgrid requires ESSs. To keep the microgrid stable, ESSs responds to any mismatch between PV generation and load demand. The ESSs are diverse variety of characteristics, most commonly used ESS is battery. However, they are suffering from slow rate of charge/discharge due to low power density. In recent years, there is another electrostatic storage component called supercapacitor energy storage system is higher power density device which can respond quickly for fluctuating and transient component of power to maintain the stability of the system. The combining of battery and SC is known as HESS which improves the system performance and cycle life of battery. A controller is designed to make effective use of HESS in DC microgrid applications. The designed controller was improved DC link voltage recovery to PV output and load interruptions, effective power balance between battery and SC.

A novel control scheme is introduced and validated for successful control of battery and SC based HESS power in DC microgrid applications. The battery is used to stabilize mild shifting power surges in the power system, while the SC is used to stabilize quickly changing power surges. In conventional control scheme the total HESS current (charging/discharging) divided into low frequency component of current supplied by using battery and high frequency component of current supplied by using SC with the help of low pass filter (LPF). However, in conventional control strategy battery current tracking error observed. Due to the sluggish dynamics of battery controller and the DC-DC converter, the

error was not resolved. To address the aforementioned issues, a new proposed control strategy is implemented which provides fast regulation of DC microgrid voltage for sudden change in PV output and load demand.

A multi-input bidirectional DC-DC converter (MIPC) has been modified in operation to suit for HESS operation in DC microgrid applications. The MIPC have better energy exchange performance between input sources compared to multiple single-input bidirectional DC-DC converters in active parallel configuration. This makes the former an excellent choice for applications like hybrid electric vehicle (HEV) and microgrids. One attractive attribute of this converter is that all switches are turned on with zero voltage switching (ZVS) which can improve the efficiency. Apart from controlling the charging/discharging of HESS, the unified controller can also share current between battery and SC in such a way that the former is subjected to less current stress which helps in extending its lifetime. The proposed modified operation of bidirectional converter ensured low equivalent series resistance (ESR) supercapacitor to be always with in desired range of state of charge (SOC). Operation of modified converter and performance of designed controller in voltage stability were validated with experimental results.

The model predictive control (MPC) approach has been proposed for battery-SC based HESS for DC microgrid applications. Develop an appropriate control strategy to assign low frequency power fluctuations to the battery and high frequency power fluctuations to the SC. The traditional PI based control strategy involves a difficult tuning process and its performance is affected when the operating point fluctuates. Therefore, the MPC based control strategy is proposed because of its simplicity, clarity and ease of implementation and the inclusion of simplicity and barriers. First, a prototype of a dual input bidirectional DC-DC converter was developed and a two-loop control strategy was developed for DC grid voltage regulation and estimating internal current control for HESS energy management and external voltage control. Second, the SC voltage regulation loop was developed to enable the charging and discharging of the SC for reliable operation of the HESS system. Finally, simulation studies are performed using MATLAB Simulink and a prototype external setup has been developed to verify the effectiveness of the proposed control strategy. The proposed MPC based power management scheme monitors and controls the HESS effectively with lower DC grid voltage variation and better discharging rate without low pass filters.

The scaled-down experimental setup is developed to validate the effectiveness of the proposed control strategy through the dSPACE 1104 real time controller. The simulation results are compared to conventional control methods. The results shows the proposed control techniques are effective. The performance results are compared for the peak overshoot and settling time to restore DC grid voltage.

# Table of Contents

<b>ACKNOWLEDGEMENTS .....</b>	<b>v</b>
<b>ABSTRACT .....</b>	<b>vii</b>
<b>Table of Contents .....</b>	<b>ix</b>
<b>List of Figures .....</b>	<b>xiv</b>
<b>List of Tables.....</b>	<b>xviii</b>
<b>Abreviations .....</b>	<b>xviii</b>
<b>List of Symbols .....</b>	<b>xix</b>
<b>Chapter-1 Introduction.....</b>	<b>2</b>
1.1    Background and Motivation .....	2
1.1.1    Batteries and SC .....	4
1.1.2    Hybrid Energy Storage System .....	5
1.2    Aim of the work .....	5
1.3    Scientific work Contributions.....	6
1.4    Thesis Organization.....	7
<b>Chapter-2 Literature Review .....</b>	<b>10</b>
2.1    Types of Energy Storage Technologies.....	10
2.1.1    Lead-Acid Battery .....	11
2.1.2    Nickel Metal Hydride Battery .....	12
2.1.3    Nickel Cadmium Battery .....	12
2.1.4    Nickel Zinc Battery .....	13
2.1.5    Lithium-Ion Battery .....	13
2.1.6    Supercapacitors.....	14
2.1.7    Fuel Cell .....	15
2.1.8    Comparison of Energy Storage devices .....	15
2.2    HESS Configurations in DC microgrid.....	17
2.2.1    Passive HESS Configuration .....	18
2.2.2    Semi-active HESS Configuration.....	18
2.2.3    Full-active HESS Configuration.....	18
2.3    HESS Power Decomposition Methods.....	19
2.3.1    LPF/HPF Based Power Sharing Method .....	20
2.3.2    Rate limiter Based Power Sharing Method .....	20
2.3.3    MPC Based Power Sharing Method .....	20
2.3.4    Fuzzy Logic Control Power Sharing Method .....	21
2.4    Control Methods for HESS .....	21
2.5    Model Predictive Control .....	22
2.6    Summary .....	23

<b>Chapter-3 Optimum Design and Analysis of a Dynamic Energy Management Scheme for HESS in Renewable Power Generation Applications .....</b>	<b>25</b>
3.1    Introduction .....	25
3.2    Modelling DC microgrid Components .....	25
3.2.1    PV Panel Modelling .....	25
3.2.2    P & O MPPT Algorithm .....	26
3.2.3    Battery Modelling .....	27
3.2.4    Modelling of SC .....	28
3.3    HESS Supported RES Configuration .....	30
3.4    Operation of microgrid with HESS .....	30
3.4.1    HESS Charging Mode .....	31
3.4.2    HESS Discharging Mode .....	32
3.5    Proposed Control Strategy of HESS .....	33
3.6    Design of Proposed Controller for HESS .....	35
3.6.1    Design of SC Current Controller .....	35
3.6.2    Design of HESS Voltage Controller .....	37
3.6.3    Battery Current Controller Design .....	38
3.7    Simulation Results and Discussion .....	40
3.7.1    Case-I: Step increase in PV generation .....	40
3.7.2    Case-II: Step decrease in PV generation .....	41
3.7.3    Case-III: Step increase in load demand .....	42
3.7.4    Case-IV: Step decrease in load demand .....	43
3.8    Comparative Performance Evaluation .....	44
3.9    Experimental Results .....	46
3.9.1    Case-I: HESS Charging Mode .....	47
3.9.2    Case-II: HESS Discharging Mode .....	48
3.10    Summary .....	49
<b>Chapter-4 Modelling of a Double-Input Bidirectional DC-DC Converter for HESS and Unified Controller Design for DC Microgrid Applications .....</b>	<b>51</b>
4.1    Introduction .....	51
4.2    Two Input Bidirectional DC-DC Converter Operation .....	53
4.2.1    HESS Discharging Mode .....	54
4.2.2    HESS Charging Mode .....	55
4.2.3    HESS Energy Exchange Mode .....	57
4.2.4    Mode Transitions .....	58
4.3    Small Signal Linear Averaged Model of 2-input Bidirectional Converter and Controller Design .....	59
4.3.1    Small Signal Linear Averaged Model of SC-DC Microgrid Stage ...	60
4.3.2    Small Signal Linear Averaged Model of Battery-DC Microgrid Stage .....	61
4.3.3    Supercapacitor State-of-Charge Controller .....	65
4.4    Simulation Study and Discussion .....	66

4.4.1	Case-I: Step Change in PV generation .....	66
4.4.2	Case-II: Step Change in load demand .....	67
4.5	Experimental Results.....	68
4.5.1	HESS Charging Mode .....	69
4.5.2	HESS Discharging Mode .....	71
4.5.3	HESS Energy Exchange Mode .....	72
4.6	Summary .....	73

**Chapter-5 Modelling, Analysis and Design of Novel Control Scheme for Two-input Bidirectional DC-DC Converter for HESS in DC Microgrid Applications ..... 75**

5.1	Introduction .....	75
5.2	HESS Supported RES Configuration .....	75
5.2.1	Power flow from HESS to DC grid .....	76
5.2.2	Power flow from DC grid to HESS .....	78
5.2.3	Power flow from Battery to SC (Energy Exchange Mode) .....	79
5.2.4	Mathematical Design Calculations of Filter Parameters .....	80
5.3	Proposed Control System Scheme of HESS .....	81
5.4	Controller Design for HESS .....	83
5.4.1	Design of SC Current Control Loop.....	84
5.4.2	Design of Battery Current Control Loop.....	86
5.4.3	Overall Outer Voltage Control Loop.....	87
5.5	Simulation Study and Discussion .....	87
5.5.1	Case-I: Step increase in PV generation .....	88
5.5.2	Case-II: Step decrease in PV generation .....	89
5.5.3	Case-III: Step increase in load demand .....	89
5.5.4	Case-IV: Step decrease in load demand .....	91
5.6	Experimental Results .....	91
5.6.1	Case-I: Step Change in PV generation .....	93
5.6.2	Case-II: Step Change in load demand .....	94
5.6.3	Case-III: Energy Exchange Mode .....	96
5.7	Comparative Performance Evaluation .....	96
5.8	Summary .....	98

**Chapter-6 A Comparative Analysis of PI and Predictive Control Strategy for HESS Based Bi-Directional DC-DC Converter for DC Microgrid Application..... 100**

6.1	Introduction .....	100
6.2	MPC Control Strategy .....	101
6.2.1	Outer Voltage Control loop .....	101
6.2.2	Inner Current Control .....	102
6.3	Simulation Results .....	103
6.3.1	Case-I: Step Change in PV generation .....	104
6.3.2	Case-II: Step Change in load demand .....	105
6.4	Experimental Results .....	106
6.4.1	Case-I: Step Change in PV generation .....	107

6.4.2	Case-II: Step Change in load demand .....	108
6.5	Comparative Performance Evaluation .....	109
6.6	Summary .....	111
<b>Chapter-7</b>	<b>Conclusion .....</b>	<b>113</b>
7.1	General Overview.....	113
7.2	Summary of Important Findings.....	113
7.3	Future Scope .....	115
<b>References.....</b>		<b>116</b>
<b>List of Publications .....</b>		<b>129</b>
<b>Curriculum-Vitae .....</b>		<b>130</b>

## List of Figures

<b>Figure Title</b>	<b>Page. No</b>
Figure 1.1: DC microgrid architecture.....	3
Figure 1.2: Battery and SC response for step change in PV generation and load demand.	5
Figure 2.1: Types of energy storage devices .....	11
Figure 2.2: Ragone chart .....	16
Figure 2.3: HESS configurations based on DC-DC converter (a) & (b) passive configuration, (c) & (d) Semi active configuration, (e) & (f) fully active configuration ..	17
Figure 2.4: (a) Block diagram representation of LPF based power sharing method (b) Rate-limiter based power sharing method (c) MPC based power sharing method (d) FLC based power sharing method .....	19
Figure 3.1:(a) Equivalent circuit representation of PV array(b) I-V & P-V Characteristics	25
Figure 3.2: (a) P & O MPPT flowchart (b) P-V characteristics .....	26
Figure 3.3: Electrical equivalent circuit of lead-acid battery .....	27
Figure 3.4: Equivalent circuit representation of SC .....	28
Figure 3.5: PV based microgrid aided by HESS .....	29
Figure 3.6: DC microgrid setup powered by PV source and supplemented by HESS.....	30
Figure 3.7: Equivalent circuit of bidirectional DC-DC converter for charging/discharging mode ..	31
Figure 3.8: Steady state waveforms for HESS charging/discharging mode.....	32
Figure 3.9: Control block diagram of conventional control scheme .....	33
Figure 3.10: Control block diagram of proposed control scheme .....	34
Figure 3.11: SC controller block diagram .....	36
Figure 3.12: Bode plot of inner current controller of SC control logic with controller .....	37
Figure 3.13: Bode plot of outer voltage controller of SC control logic .....	37
Figure 3.14: Battery current controller block diagram .....	39
Figure 3.15: Bode plot of battery current controller .....	39
Figure 3.16: Simulation results for step increase in PV generation in conventional control scheme.....	40
Figure 3.17: Simulation results for step increase in PV generation in proposed control scheme.....	41

Figure 3.18: Simulation results for step decrease in PV generation in conventional control scheme .....	41
Figure 3.19: Simulation results for step decrease in PV generation in proposed control scheme .....	42
Figure 3.20: Simulation results for step increase in load demand in conventional control scheme .....	42
Figure 3.21: Simulation results for step increase in load demand for proposed control scheme .....	43
Figure 3.22: Simulation results for step decrease in load demand for conventional control scheme .....	44
Figure 3.23: Simulation results for step decrease in load demand for proposed control scheme .....	44
Figure 3.24: Graphical comparative performance of proposed and conventional control scheme. (a) settling time (b) Peak overshoot.....	45
Figure 3.25: Prototype model of the proposed topology .....	46
Figure 3.26: (a) Experimental results for HESS charging mode: DC microgrid voltage ( $V_{DC}$ ), battery current ( $i_B$ ), SC current ( $i_S$ ). (b) supercapacitor SOC waveform .....	47
Figure 3.27: (a) Experimental results for HESS discharging mode: DC microgrid voltage ( $V_{DC}$ ), battery current ( $i_B$ ), SC current ( $i_S$ ) (b) supercapacitor SOC.....	48
Figure 4.1: Different configurations of HESS, comprising of battery and SC, interfaced to DC microgrid. (a) Two separate bidirectional converter modules used. (b) Single double-input bidirectional converter .....	51
Figure 4.2: DC microgrid setup powered by PV source and supplemented by HESS .....	52
Figure 4.3: Two-input bidirectional converter topology for HESS.....	53
Figure 4.4: Steady-state waveforms for HESS discharging mode of operation.....	54
Figure 4.5: Staedy-state waveforms for HESS charging mode of operation.....	56
Figure 4.6: HESS energy exchange mode of operation, (a) Active circuit through which current flow. (b) Staedy-state waveforms .....	57
Figure 4.7: Transitions to different modes represented using a flow chart .....	58
Figure 4.8: Overall control system description for current bifurcation between SC and battery units .....	59
Figure 4.9: SC and battery control logic (a) Control system description for SC control (b) Control system description for battery control .....	59

Figure 4.10: Bode plot of inner current controller of SC control logic with and without controller.....	61
Figure 4.11: Bode plot of outer voltage controller of SC control logic with and without controller .....	61
Figure 4.12: SOC charge controller for SC (a) Logic to select between charging/ discharging (b) Control logic diagram .....	62
Figure 4.13: Bode plot of current controller of battery control logic .....	65
Figure 4.14: Simulation results for step change in PV generation .....	67
Figure 4.15: Simulation results step change in load demand.....	68
Figure 4.16: Low power hardware prototype developed .....	69
Figure 4.17: Experimental results for HESS charging mode. (a) DC microgrid voltage ( $V_{DC}$ ), battery current ( $i_B$ ), SC current ( $i_S$ ). (b) Battery and supercapacitor SOC waveforms .....	70
Figure 4.18: Experimental results for HESS discharging mode. (a) DC microgrid voltage ( $V_{DC}$ ), battery current ( $i_B$ ), SC current ( $i_S$ ). (b) Battery and supercapacitor SOC .....	71
Figure 4.19: (a) Experimental results for HESS energy exchange mode. DC microgrid voltage ( $V_{DC}$ ), Battery current ( $i_B$ ), and SC current ( $i_S$ ). Transition from discharge mode to energy exchange is shown. (b) Battery and supercapacitor SOC .....	72
Figure 5.1: DC microgrid architecture operation of HESS with PV system .....	76
Figure 5.2: Equivalent circuit of two-input bi-directional converter (a) $S_2, S_3, S_5$ operates (b) $S_2, S_4, S_5$ operates (c) $S_1, S_4, S_6$ operates (d) Steady-state waveforms in discharging mode .....	77
Figure 5.3: Equivalent circuit of two-input bi-directional converter (a) $S_1, S_4, S_6$ operates (b) $S_2, S_4, S_5$ operates (c) $S_2, S_3, S_5$ operates (d) Steady-state waveforms in charging mode .....	78
Figure 5.4: HESS energy exchange mode of operation (a) equivalent circuit (b) Steady-state waveform .....	79
Figure 5.5: Overall control system description for current bifurcation b/w SC and battery unit (a) conventional control scheme (b) proposed control scheme .....	82
Figure 5.6: Block diagram representation of SC control logic .....	84
Figure 5.7: Block diagram of Battery control logic .....	84
Figure 5.8: Bode plot of inner current logic for with and without compensation .....	85

Figure 5.9: Open loop Bode plot of battery current logic for with and without compensation .....	86
Figure 5.10: Open loop Bode plot of outer voltage logic for with and without compensation .....	87
Figure 5.11: Simulation results for step change in PV generation .....	88
Figure 5.12: Simulation results for step change in load demand .....	90
Figure 5.13: Hardware prototype developed for HESS .....	92
Figure 5.14: Experimental results for step change in PV generation (a) step increase in PV generation (b) step decrease in PV generation (c) step increase and decrease in PV generation.....	93
Figure 5.15: Experimental results for step change in load demand (a) step increase in load demand (b) step decrease in load demand (c) step increase and decrease in load demand..	95
Figure 5.16: Experimental results for HESS energy exchange mode. DC microgrid voltage (V <sub>DC</sub> ), Battery current (i <sub>B</sub> ), and SC current (i <sub>S</sub> ). Transition from discharge mode to energy exchange is shown .....	96
Figure 5.17: Graphical comparative performance of proposed and conventional control scheme. (a) Settling time (b) Peak overshoot .....	97
Figure 6.1: Block diagram representation of MPC for HESS .....	101
Figure 6.2: Simulation results for step change in PV generation .....	104
Figure 6.3: Simulation results for step change in load demand .....	105
Figure 6.4: Hardware prototype developed for HESS .....	106
Figure 6.5: Experimental results for step change in PV generation (a) step increase in PV generation (b) step decrease in PV generation (c) step increase and decrease in PV generation .....	108
Figure 6.6: Experimental results for step change in load demand (a) step increase in load demand (b) step decrease in load demand (c) step increase and decrease in load demand	109
Figure 6.7: Comparative analysis of MPC over PI control methods (a) Step change in PV generation (b) Step change in load demand (c) battery current (d) SC current .....	110
Figure 6.8: Graphical comparative performance of MPC over conventional PI control schemes (a) Settling time (b) Peak overshoot .....	110

## List of Tables

<b>Table Title</b>	<b>Page. No</b>
Table 2.1: Charecterstics of various ESSs.....	16
Table 2.2: Comparison of HESS configurations .....	18
Table 3.1: Nominal parameters for simulation study .....	41
Table 3.2: System parameters for experimental study .....	45
Table 4.1: Nominal parameters for simulation study .....	66
Table 4.2: Parameters of the experimental system.....	69
Table 5.1: Switching states in different time intervals .....	77
Table 5.2: Switching states in different time intervals .....	78
Table 5.3: Relation between different voltages in each mode.....	80
Table 5.4: Small signal linear averaged transfer functions .....	85
Table 5.5: Nominal parameters for simulation study .....	91
Table 5.6: DC microgrid implementation parameters .....	92
Table 6.1: Nominal parameters for simulation study .....	103
Table 6.2: DC microgrid implementation parameters .....	106
Table 7.1: Comparative performance of various control methods .....	115

## Abbreviations

ANN	Artificial Neural Network
CCM	Continuous Conduction Mode
EV	Electric vehicle
ESS	Energy storage systems
HESS	Hybrid energy storage system
HPF	High pass filter
DOD	Depth of Discharge
EMS	Energy management scheme
FC	Fuel cell
HEV	Hybrid electric vehicle
LPF	Low-pass filter
MISO	Multi Input Single Output
MPP	Maximum power point.
PI	Proportional-integral
NiCd	Nickel cadmium
SC	Supercapacitor
NiMH	Nickel metal hydride
PV	Photovoltaic
NiZn	Nickel zinc
SOC	State of charge
RESs	Renewable energy sources
PWM	Pulse width modulation
UPS	Uninterruptable power sources

## List of Symbols

$d_B$	Battery duty cycle
$d_{SC}$	SC duty cycle
$w_c$	Cut-off frequency of LPF
$f_{sw}$	Switching frequency
$i_B$	Battery current
$i_{B,ref}$	Battery reference current
$i_{SC}$	SC current
$i_{SC,ref}$	SC reference current
$V_{DC}$	DC grid voltage
$V_{DC,ref}$	DC grid reference voltage
$i_{tot}$	Total current demand
$V_B$	Battery voltage
$V_{SC}$	SC voltage
$L_B$	Battery inductance
$L_{SC}$	SC inductance
$L_{eq}$	Equivalent inductance
$\Delta i_L$	Peak-to-peak inductor current
$V_{PV}$	MPP voltage
$i_{PV}$	MPP current
$P_{max}$	Maximum power
$I_{HIGH}$	High frequency component of current
$I_{LOW}$	Low frequency component of current
$P_{std}$	Steady state power component
$P_{tran}$	Transient power component
$P_{dc}$	DC grid power
$P_{ren}$	RES power
$P_B$	Battery power
$P_{SC}$	SC power
$K_{p,v}$	Proportional constant of outer voltage loop
$K_{i,v}$	Integral constant of outer voltage loop
$v_{err}$	Voltage error
$P_{B\_un}$	Uncompensated power from the battery system
$i_{B,err}$	Battery error current

$H_B$	Feedback gain of battery control loop
$H_{SC}$	Feedback gain of SC control loop
$H_v$	Feedback gain of outer voltage control loop
$K_{p,SC}$	Proportional constant of SC current controller
$K_{p,B}$	Proportional constant of battery current control loop
$K_{i,SC}$	Integral constant of SC current control loop
$K_{i,B}$	Integral constant of battery control loop
$G_{pi,sc}$	PI controller transfer function of inner SC current loop
$G_{i_{SC}d_{SC}}$	Control to SC current transfer function
$G_{ol\_SC}$	Open loop transfer function of SC control loop
$G_{cl\_SC}$	Closed loop transfer function of SC control loop
$G_{v_{DC}i_{SC}}$	SC current to output voltage transfer function
$G_{i_Bd_B}$	Control to battery current transfer function
$G_{pi,BAT}$	PI controller transfer function of battery current loop
$G_{pi,v}$	PI controller transfer function of outer voltage control loop
$SOC_i$	Initial SOC of SC
$Q_{SC}$	Rated SC charge
$I_{dc}(k)$	Total load current
$V_{dc}(k)$	Present sampling DC grid voltage
$V_{SC}(k)$	Present sampling SC voltage
$i_{SC}(k)$	Present sampling SC current
$V_B(k)$	Present sampling battery voltage
$i_B(k)$	Present sampling battery current
$i_B(k+1)$	Prediction of battery current
$i_{SC}(k+1)$	Prediction of SC current
$i_C$	Charging current
$\frac{dv_{dc}}{dt}$	Rate of change of DC grid voltage
$T_S$	Sampling period
$\frac{di_b}{dt}$	Rate of change of battery current
$\frac{di_{sc}}{dt}$	Rate of change of SC current
$d_b(i)$	Iteratively calculated battery duty cycle
$d_{sc}(i)$	Iteratively calculated SC duty cycle
$J$	Objective function of MPC

# **Chapter-1**

## **Introduction**

# Chapter-1

## Introduction

### 1.1 Background and Motivation

The use of renewable energy sources (RESs) in global microgrids has been growing rapidly since 2000[1-2]. The maturity in RESs significantly reduced installation and maintenance costs. In recent days, developing countries in Latin America, South Asia and South Africa have been moving towards RESs. The investments towards RESs with in India and China also expanding rapidly. Due to reduced cost of RESs and land availability countries like USA and Australia has attracted towards the RESs investments. In the year 2016, RES accounted for 24% of the world's total generation and in 2017 it accounted for 25% [3].

The RESs are very economical, environmentally friendly and sustainable. Therefore, all governments are investing plans and investments to improve RES utilization as much as possible [4-7]. The RESs like solar energy [8-10], wind energy [11-14] and wave energy [15-17] are extensively studied and implemented. According to the best RES, solar and wind are the most promising [2]. However, without combining with energy storage devices, these RESs cannot be used as long-term electrical solutions. The solar and wind energy variations are influenced by the time of day, weather patterns and installation site. For standalone and grid interactive systems, ESSs are often used for smooth power output from RESs. ESSs serve as energy backup, which stores energy during excess power consumption and releasing it when the AC/DC grid experiences a power deficit. The ESSs act as uninterruptable power supplies (UPS), providing a steady voltage and frequency during power outages. ESSs are also very important key component for microgrid systems.

Figure 1.1 depicts a standard DC microgrid architecture. The power produced by the PV panel is generally DC. Whereas power output from wind generation is AC. Due to different RESs nature, the power electronics like AC-DC converters and DC-DC converters are connected in between DC grid. The RES's power output is controlled and regulated by the power converters.

The power mismatch between demand and supply in the system, ESSs are required. Combining multiple ESS has been increasingly common in recent years, as it provides more benefits then using a single ESS. HESS incorporate the characteristics of various energy storage elements to increase the system stability.

The two operating modes of DC microgrid either in standalone mode or grid-connected mode. In standalone mode, the local loads are operated using RES generation and HESS. The power flow between the DC and AC microgrids provides more stability and control over the power output from RESs and HESS in grid-connected mode. The power balance in the system, on the other hand, is determined by the system stability. In [19] provides a comprehensive overview of control methods and energy efficient techniques for AC and DC microgrids. The main requirement during PV generation and load demand variance is to control the grid voltage as rapidly as possible. Thus, the efficient power sharing methods are required to balance the grid using RESs and HESS. The work presented in this thesis, different types of bidirectional converters and control schemes for HESS in the DC microgrid applications. The suitable control methods are designed for DC grid voltage management, control of battery charge/discharge ratios and power splitting between battery and SC.



**Figure 1.1** DC microgrid architecture.

### 1.1.1 Batteries and SC

One of the most widely used energy storage system is the battery. Its stores electrical energy in the form of chemical structure. In general, battery has high energy density device, it means to support power to the system for longer time. To process electrochemical reactions inside the cell, a certain amount of time is needed. Thus, it is not support for sudden and fast changing of PV generation and load demand. Due to its high internal resistance, their internal losses are high. During charging/discharging of battery its internal structural integrity changes. The cycle life of battery determined by its charge/discharge rate. Even though batteries have drawbacks like low power density and life cycle, they are most dominant in renewable power generation and electric vehicle applications.

The oldest battery technology is the lead acid battery. Gaston Plante was the first to study how to extract current from a pair of lead plates immersed in sulphuric acid in 1859 [20]. To meet several requirements, the different design and models of lead-acid batteries have been proposed. However, the basic fundamental electro chemical lead-acid battery remains same over 150 years [20]. It is a popular rechargeable battery used in microgrids and EVs.

The electrochemical double-layer capacitor is termed as supercapacitors (SCs) or ultracapacitors by Nippon electric company. In 1978, they produced commercial SCs and used for computer memory backup in consumable electronics [21]. Several products have been modified during the course of the manufacturing process. The SCs with capacitances ranging from 1000 to 5000F and energy densities ranging from 3.5 to 4.9 Wh/kg is commercially available in the 21<sup>st</sup> century [21]. The SCs are low voltage range with high capacitance value compared to electrolytic capacitance. It reduces the gap between the battery and the electrolytic capacitor system. The major advantages of SC are high power density and longer life cycle. During charging/discharging process, there no change of internal structural integrity in SC. The only drawback of SC is that it has a higher rate of self-discharge. The self-discharge rate is around 20% of stored energy in a day even in no load condition.

The battery and SC have complementary properties. Both the battery and the SC have their benefits and drawbacks. The system accuracy is improved when these two energy storage devices are combined. The battery life cycle is greatly enhanced with adding SC

storage device. This will also minimize the replacement cost of battery system. As a results, the battery and SC combination is an appealing option for wind power, PV generation and EV applications.

### 1.1.2 Hybrid Energy Storage System

The main aim of HESS is to achieve optimum ESS efficiency by integrating multiple forms of energy storage devices [18]. The high energy and power density are the main characteristics of ideal ESSs. This behaviour cannot fulfil by using single energy storage device.

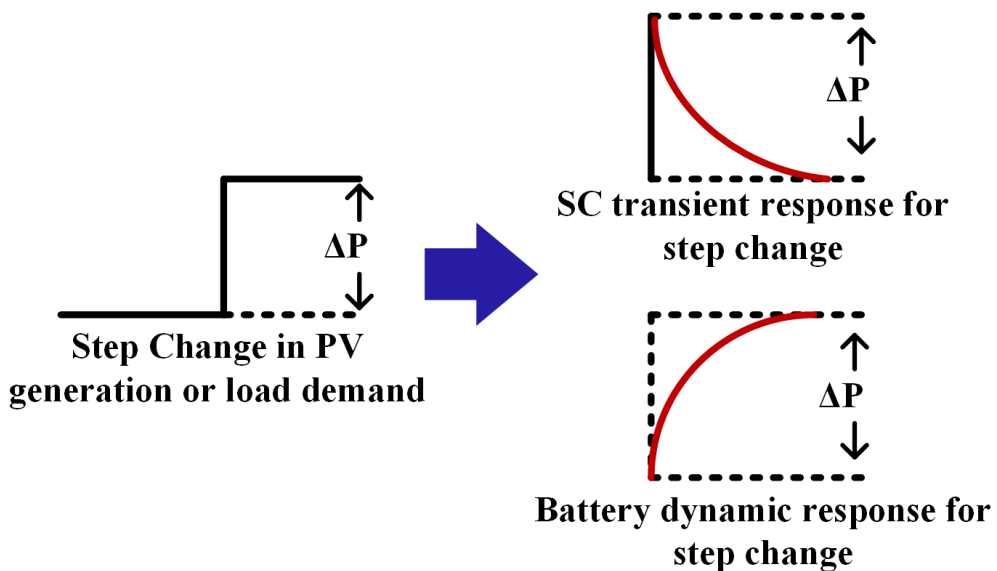


**Figure 1.2** Battery and SC response for step change in PV generation and load demand

The ESSs with complimentary characteristics combined to form HESS. Depending upon power and energy density requirements, ESSs are combined. For step increase in load, battery and SC responses are shown in Figure 1.2. The SC can discharge a large amount of power in a short amount of time, but it cannot sustain the power for an extended period of time. The battery, on the other hand, responds slowly to a step change in load. It can, however, sustain the same level of energy for an extended period of time. Quick and long lasting power can be obtained with the combined action of battery and SC provides the ideal ESS response. In our work, we merged a lead-acid battery and a SC to create HESS. The lead-acid battery has high energy density, low life cycle, low cost per watt-hour and low self-discharge rate. In contrast, SC has high power density, low energy density, high cost per watt-hour and high self-discharge rate.

For adequate utilize of different ESSs in HESS we require effective control methods. The control methods should exhibits a significant role for enhancing entire HESS. The main requirements for HESS control methods are (i) improve DC grid voltage regulation to the step change in PV and load demand (ii) maintain power balance between battery and SC (iii) maintain battery and SC state of charge (SOC) with in the safe operating limits.

## 1.2 Aim of the work

For a better use of HESS, efficient control schemes are necessary. The main objective of this work presents the different types of bidirectional converters and control schemes for standalone operation of HESS. The main focus of the study is on converter and controller design as well as stability analysis, simulation and experimental evaluation of the proposed control methods. For other details of the thesis, performance evaluation of proposed control scheme over the conventional control scheme with step change in PV generation and load demand for peak overshoot and settling time to restore grid voltage.

## 1.3 Scientific Contributions

During the research work, the following scientific contributions were made:

1. A novel control strategy for HESS is discussed in detail. In the proposed system, battery is utilized to stabilize the moderate change of power surges, whereas SC is utilized to stabilize rapidly changing power surges. A two loop proportional-integral (PI) controller is designed for closed loop operation of HESS. In proposed control scheme, the uncompensated power from the battery system is utilize to improve SC system. The simulation and experimental results are developed for proposed control scheme for step change in PV generation and load demand, provides fast DC grid voltage regulation.
2. A MIPC is designed to suit HESS operation in DC microgrid applications. One attractive attribute of this converter is that all the switches are turned on with zero voltage switching (ZVS) which can improve its efficiency. This MIPC not only provide decoupled control of battery and SC power but also provides energy exchange between storage devices within. The designed controller was better DC grid voltage restoration to PV generation and load demand, effective power balance between the battery and SC.

3. The proposed advanced controller designed for MIPC for HESS. In the proposed scheme, uncompensated power from the battery system is utilized to improve the SC system. This approach reduce stresses, increase life span of battery and improve the overall system performance to the step change in PV generation and load demand and provides faster DC grid voltage.
4. The traditional PI controller for a HESS has drawbacks such as difficult tuning of the controller parameters and the additional filters to allocate high and low frequency power fluctuations. In this work proposed a model predictive control (MPC) method to control two-input bidirectional DC-DC converters for HESS in a DC microgrid applications. MPC uses the current state of system and considers the effect of present control and action of future outputs. MPC controllers solves the optimization problem at each sampling interval. MPC controller provides the effective power sharing between battery and SCs in such a way that regulates the grid voltage as quick as possible.

## 1.4 Thesis Organization

The Research for the thesis is divided into seven different chapters and presented as follows:

The **first Chapter** presents the background and motivation behind the study, the purpose of the work, the research contributions of the work and outline of the thesis presented in this chapter.

**Chapter 2** present a comprehensive literature review for the research work are in detail. The comparison of various ESSs are provided. The possible variety of HESS configurations for DC microgrid applications are discussed. The various forms of power decomposition methods for battery SC based HESS systems are discussed.

In **Chapter 3**, the proposed control technique is explored in detail. The proposed control scheme controller design, device parameters selection, stability analysis, experimental results and performance of the proposed control scheme over conventional control scheme.

In **Chapter 4**, the multiple input bidirectional converter proposed and detailed modified operation as two-input bidirectional DC-DC converter for HESS operation is

elaborated. Small signal linear averaged model of the two-input converter is developed to design controller parameters. The simulation and experimental results are presented.

In **Chapter 5**, the advanced MIPC for HESS controller is discussed. The controller design for HESS by using small signal analysis discussed. The performance comparisons of the proposed and conventional control methods are also presented.

In **Chapter 6**, the analysis of the MPC control scheme for HESS is discussed. The MPC control method is introduced along with its architecture, implementation algorithm, simulation and experimental analysis and through comparison with the conventional PI control methods are presented.

Finally, **Chapter 7** highlights the brief conclusions and the significant contribution of research work and provides scope for further research in this area.

# **Chapter-2**

## **Literature Review**

# Chapter-2

## Literature Review

### 2.1 Energy Storage Technologies

Electrical energy can be stored in many different forms such as electrochemical energy, kinetic energy, potential energy, etc. This stored energy is then converted back to electrical form but while conversion, some losses may be present. Because of the self-sufficiency provided by the smart grid technologies, microgrids are becoming very popular [22]. ESSs can be considered as their essence for providing continuous, reliable, and sustainable electricity. Microgrids are the groups with many interconnected sources and sinks of power, which can operate on their own as well as in synchronism with the central or main grid. This autonomous operation of microgrids are called electrical islanding [23].

A detailed analysis of the power of the ESSs is provided in [24]. It considers storage power as a function of time  $S_T(t)$  and is positive while discharging and negative while charging.  $P_R(t)$  is the power production profile by installed generation system which is either supplied to ESS or to the grid or lost by dissipation in network. The supply profile  $S_U(t)$  is the time-structure of the power that the producer delivers to the grid.

The ESSs ensures that the power produced plus the storage power yields the desired power supplied

$$S_T(t) = \alpha \cdot S_U(t) - P_R(t) \quad (2.1)$$

The scalar ‘ $\alpha$ ’ account for the losses which makes the total energy supplied less than the total energy produced. The criteria for the selection of the energy storage technologies depend on application, energy and power ratings, size, lifetime, response time, capacity and cost [25-27]. A brief analysis of the types of energy storage systems and their comparison is shown in Figure 2.1.

### 2.1.1 Lead-Acid Batteries

The lead-acid battery is one of the most well-known and widely used rechargeable electrochemical storage devices, having been invented about 150 years ago [28, 29]. Due to its low cost and reliability, they are used in renewable power generation and hybrid electric vehicle (HEV) applications. In general, the cathode plates are made of lead dioxide ( $PbO_2$ ) and the anode plates of porous lead (Pb) and both plates are immersed in an electrolyte, sulphuric acid ( $H_2SO_4$ ). During discharging process, lead over the anode reacts with  $H_2SO_4$  making lead sulphate and electrons [30].

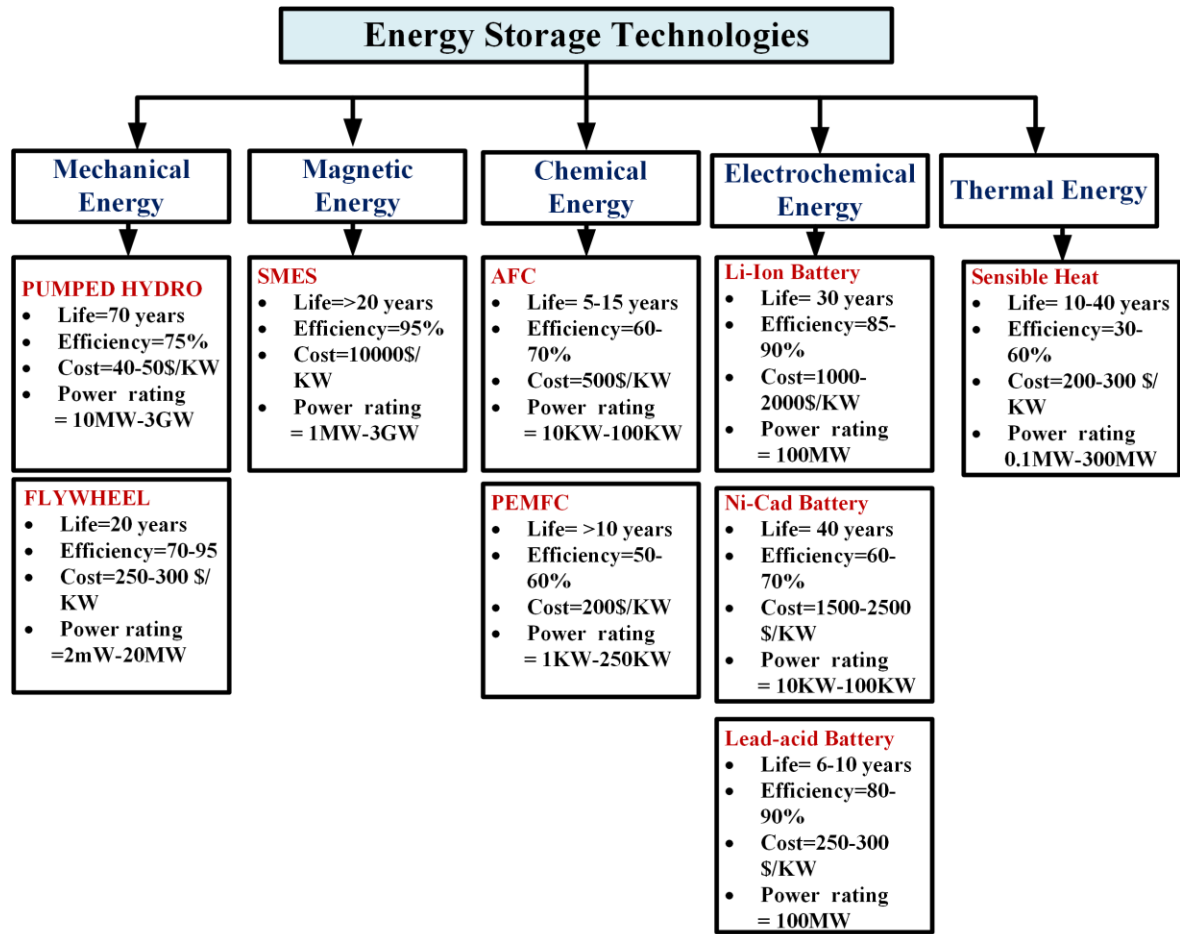


**Figure 2.1** Types of Energy Storage Devices

The cycle life of lead-acid battery is 1200-1800 cycles, with an efficiency range of 85% to 90% [31]. They have energy and power densities of 30-50 Wh/kg and 75-300 W/kg respectively [28]. The rated cell voltage of a lead-acid battery is about 2V [32]. At a temperature of 25° C, its self-discharge rate is less than 2% of its rated capacity. Thus, it is

most suitable for longer term power storage applications [32]. The temperature range of operation from  $-30^{\circ}\text{C}$  to  $+40^{\circ}\text{C}$  range [33]. When lead-acid battery is discharged less than 20% of its rated capacity, its lifetime is seriously affected. When charged and discharged at a high rate of current, its lifetime is reduced. Due to heavy weight lead collectors, lead acid battery has low power and energy densities [35, 36]. The detailed research in these fields has culminated in collectors that are non-corrosive and have a high energy and power density [37]. Its life time improved with proper control methods and energy management strategy.

### **2.1.2 Nickel Metal Hydride Batteries (NiMH)**

The NiMH battery technology invented around 100 years ago. The applications of NiMH are like electronic devices, EV, electrical tools and UPS. In NiMH, positive and negative electrodes are made with nickel hydroxide and metal alloy respectively. The NiMH batteries cycle life depends on depth of discharge (DOD). For 100% DOD, its life cycle is  $>1000$  and 10% DOD it has life over 10,000,000 cycles [38]. It has efficiency from 65% to 70% range [32]. Their energy and power density are 70-110 Wh/kg and 150-300 W/kg [38, 39]. The NiMH batteries operating temperature range from  $-30^{\circ}\text{C}$  to  $+70^{\circ}\text{C}$ . However, the desired performance obtained at temperature between 0 to  $+40^{\circ}\text{C}$  [38]. The NiMH batteries rated voltage is around 1.2V [32].

The NiMH batteries are required less maintenance and environmental friendly. They are wide range of operating temperature and less memory effect. The operation of NiMH batteries generates heat and complex charging technology is necessary for safe operation. For larger scale cost of operation will increase [40].

### **2.1.3 Nickel Cadmium Batteries (NiCad)**

About 1950 A.D., NiCad batteries were invented [31]. The negative electrodes are made of nickel species and positive electrodes are made of cadmium species active materials in NiCad batteries. In NiCad batteries, aqueous alkali solution used as electrolyte. The NiCad and NiMH batteries are popular in applications like EVs as they have high energy density can be discharged for very low SOC range and long life cycle [40]. The NiCad batteries cycle life depends on DOD. Its cycle life in the range of 2,000-2,500 cycles [41]. The efficiency range between 60-70%. Its energy and power density are 70-110 Wh/kg and 150-300 W/kg respectively [28]. The NiCad batteries operating temperature range from  $-40^{\circ}\text{C}$  to  $+60^{\circ}\text{C}$ . The NiCad batteries rated voltage of 1.2V and cut off voltage of 1V [42].

NiCad batteries have a high specific energy, but they have a high memory effect, low performance and high price [31, 32, and 40]. The self-discharge rate of NiCad batteries are high compared to lead acid battery technology [31, 32, and 40].

#### **2.1.4 Nickel Zinc Batteries (NiZn)**

In NiZn batteries, Positive electrode made with nickel and negative electrodes made with zinc hydroxide. The electrolyte in NiZn batteries is a potassium peroxide aqueous solution [32].

NiZn batteries have a life cycle of 100 to 300 cycles [40]. NiZn batteries have a 75% efficiency rating. It has a power density of 150-300 W/kg and an energy density of 60-65 Wh/kg [40]. The operating temperature of NiZn batteries are  $-10^{\circ}\text{C}$  to  $+50^{\circ}\text{C}$ . The nominal voltage of NiZn battery is 1.65V [32].

The main advantages of NiZn batteries are handle peak power demand and no effect from heavy charge and deep discharge cycles [38]. The NiZn batteries has high energy density compared to lead-acid battery. When compared to other battery technologies, NiZn batteries have the highest operational cost and life cycle [34].

#### **2.1.5 Lithium-Ion Batteries (Li-ion)**

Around 40 years ago, the Li-ion battery was first introduced [41]. Sony produced the commercial Li-ion battery in 1991, based on graphite and lithium oxide [40]. It is very popular in electronic devices like mobile phones, tablets, laptops and EV applications. The positively charged lithium ions move from the anode to the cathode via the electrolyte. The reverse reaction takes place from the cathode to anode. These movements generate electrons into the systems which pass from the external circuitry. There are many Li-ion batteries depending upon the electrolyte and plate material used such as lithium cobalt oxide ( $\text{LiCoO}_2$ ), lithium manganese oxide ( $\text{LiMn}_2\text{O}_4$ ), Lithium iron phosphate ( $\text{LiFePO}_4$ ), Lithium nickel manganese cobalt oxide ( $\text{LiNiMnCoO}_2$ ) and Lithium titanite ( $\text{Li}_4\text{Ti}_5\text{O}_{12}$ ) batteries.

The energy and power density of these batteries are more than that of lead acid batteries and high cell voltage of about 3.6V. They are very economical with fast charging rates, high efficiency of around 95%. Its light weight makes it very portable and so used in mobiles and laptops. Good protection schemes should be used for these batteries as they

catch fire easily [42]. A good battery management system is needed to avoid it to go through over charge/discharge and over-heating.

The Li-ion battery have range from 1000-10,000 life cycles depending upon the DOD [32, 41]. The power and energy density are 50-2000 W/kg and 80-150 Wh/kg respectively [40, 42]. It has very low self-discharge rate around <5% per month of its rated capacity. The operating temperature range from -20° C to +60° C [44]. The most important features for Li-ion batteries are no memory effect, longer lifetime, high power and energy densities [43]. The Li-ion batteries are more susceptible to the temperature changes and battery deep charge and discharge. These batteries are used in EV and renewable power applications. However, Li-ion batteries are more expensive than other energy storage systems. The detailed study being done in these fields in order to improve low-cost Li-ion materials and battery control systems [44].

### 2.1.6 Supercapacitors

SCs stores the energy in the form of charge difference appearing on its positive and negative plates separated by some distance. Supercapacitors also called as double layer capacitors is similar to conventional capacitors except that it has high capacitance value due to its bigger plate area and less distance between plates as:

$$C = \varepsilon \frac{A}{d} \quad (2.2)$$

The supercapacitor is used mostly where fast charging/discharging processes are to be done and it provides high current pulse [45]. As seen from eq. (2) it is clear that the design of Electric Double Layer Capacitor (EDLC) are such that their surface area of the electrode is more with thin high-permittivity dielectric between them so as to have higher value of capacitance. The material of the electrode and electrolyte affects the performance of supercapacitors. Use of porous carbon as the current collector, activated carbon electrodes, metal-oxide electrodes and electronically conducting polymer electrodes [46].

High energy density and high capacitances make activated carbon electrodes as the most commonly used electrode material. The carbon could be in different forms such as graphane, carbon nano tubes, etc [46]. Their capacities are about a thousand times compared to those of conventional capacitors making large amount of energy to be stored in them.

The time constant of a supercapacitor is calculated by the multiplication of ESR of the supercapacitor and its capacitance like a typical RC series circuit [47]. ESR is its equivalent series resistance. Supercapacitors are highly effective in reducing power gaps lasting from a few seconds to a few minutes, and they can be recharged quickly. Because of the rapid charging/discharging processes, supercapacitors are used as peak load boosters for Plug in hybrid electric vehicles (PHEV), in Uninterrupted Power Supplies, automobiles in regenerative braking, etc.

The energy and power density of SCs are ranges from 2.5-15 Wh/kg and 500-5000 W/kg [48]. The efficiency of SC is more than 90%. The major demerits of SC is high self-discharge rate, which averages more than 20% per a day. The cost of SCs is relatively high compared to other storage devices.

### **2.1.7 Fuel Cell**

The Fuel cell (FC) is an electrochemical device which converts the chemical energy into electrical energy by making and breaking of molecular bonds [34]. When the hydrogen is fed at the anode and oxygen is fed at the cathode, then a potential difference occurs between the two electrodes. The hydrogen here is the fuel and oxygen is the oxidant causing a chemical reaction between them.

Mostly fuel cell has power rating up to 50MW and good energy density from 800 to 10000Wh/kg but its efficiency is less with high cost. Fuel cell can be used for medium as well large-scale applications from kilowatt to megawatt ratings.

The following are the advantages of FC over other energy storage devices: It has the following characteristics (i) higher efficiency (ii) less noise (iii) low carbon emission (iv) longer lifespan (v) high reliability [34]. However, the efficiency of FC depends on the extraction of power from it. It is relatively more expensive than other energy storage devices and compared to lead-acid battery and SC, the reaction time is slower.

### **2.1.8 Comparison of Energy storage devices**

Figure 2.2 [49] illustrates the features of multiple energy storage systems in a single graph. It includes details on the charge discharge times of various energy storage systems. The complete information about the chart can be presented in [50]. By this graph to build HESS combination using different energy storage devices. The comparative characteristics

of different energy storage devices are tabulated in Table 2.1. For each energy storage technology have unique merits and demerits. Among all energy storage devices SC has high power density and cycle life  $>500,000$ . In comparison to other energy storage devices, the Li-ion battery has a high efficiency and FC has a higher energy density. The wide range of operating temperature for NiMH batteries compared to other devices.

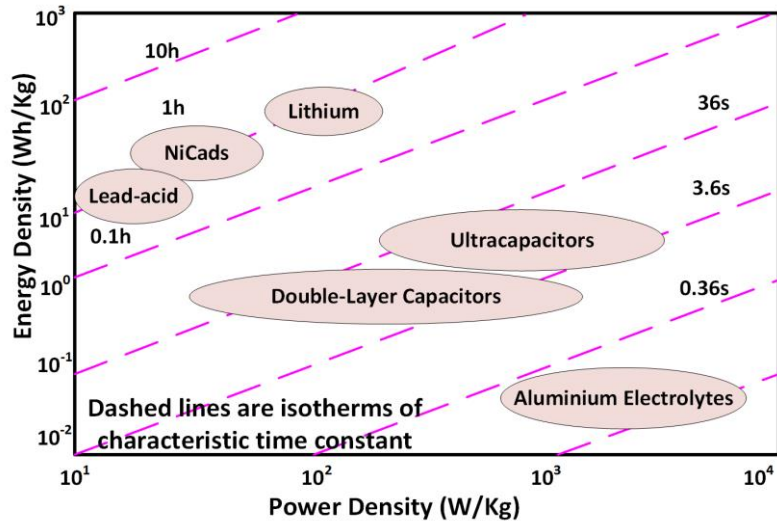


Figure 2.2 Ragone chart

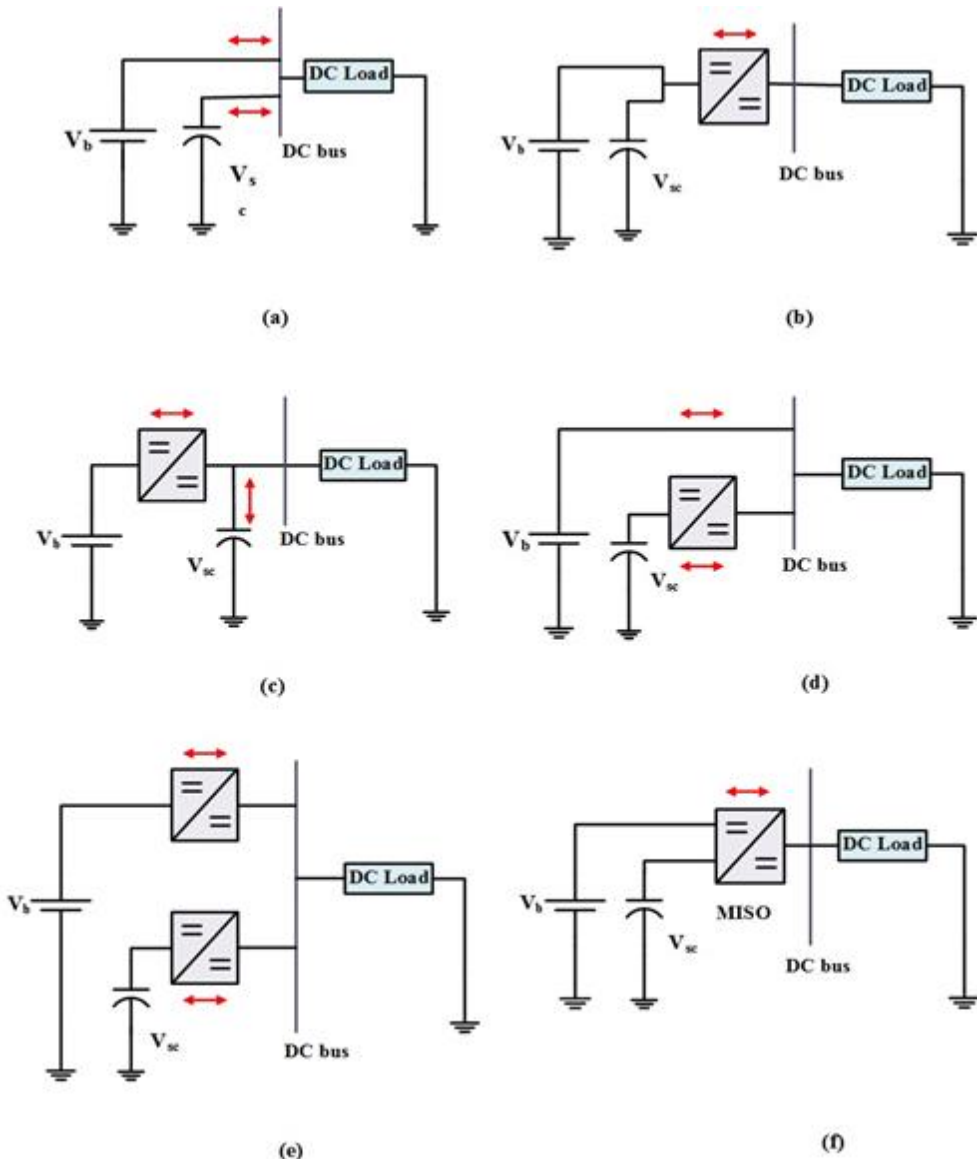
The ESSs that are selected are decided by the system requirements. In general, single energy storage unit may not be able to meet high power and energy density requirements. For example, for high energy density lead-acid battery is preferable and can store energy for longer time. The SC is preferable for high power density, although it cannot maintain the same power output for longer period of time. The cycle life of lead-acid battery is low. In compliment to the lead-acid battery, SC has high cycle life. In general, combined characteristics of ESS have to make ideal behaviour of storage system. The lifetime of lead-acid battery can be improved when combined with the SC.

Table 2.1 characteristics of various ESSs

	Cycle life (cycles)	Power density (W/kg)	Energy density (Wh/kg)	Efficiency (%)	Operating temp (°C)
<b>Lead-acid</b>	1200-1800	75-300	30-50	85-90	-30 to +40
<b>NiMH</b>	>1000	150-300	70-110	65-70	-30 to +70
<b>Ni-Cd</b>	2000-2500	150-300	70-110	60-70	-40 to +60
<b>Ni-Zn</b>	100-300	150-300	60-65	75	-10 to +50
<b>Li-Ion</b>	1000-10000	50-2000	80-150	>95	-20 to +60
<b>Fuel cell</b>	1000	500	800-10000	25-35	
<b>SC</b>	>500000	500-5000	2.5-15	>90	

## 2.2 HESS Configurations in DC microgrid

To exploit the advantages of both battery and SC, different topologies of HESS are shown in Figure 2.3. It has some advantages such as (i) reduces the required number of converters (ii) easy integration of ESSs in DC microgrid. The integration of HESS and DC microgrid is a cost-effective and stable solution. Figure 2.3 [51] illustrates the different HESS configurations that can be found in a DC microgrid. The selection of HESS configuration determined by the system power requirements. They are three basic types of HESS configurations, which are passive HESS configuration, semi-active HESS configuration and full-active HESS configuration [52].



**Figure 2.3** HESS configurations based on DC-DC converter. (a) & (b): passive configuration, (c) & (d): Semi active configuration, and (e) & (f): Fully active configuration.

### 2.2.1 Passive HESS Configuration

This classification is based on how the HESS is interconnected with the DC bus. In the Figure 2.3 (a) and (b) shows the passive HESS configuration. Battery and SC are directly connected in parallel. Figure 2.3 (a) is the simplest of all configurations and cost effective. However, it lacks in control over the ESS operation and requires high rated battery and SC for high power applications. Figure 2.3 (b) able to avoid requirement of high rated ESS by incorporating DC-DC converter, however still there is no control over the battery and SC voltage. Furthermore, passive configuration demands equal voltage of battery and SC for proper operation.

### 2.2.2 Semi-active HESS Configuration

The semi active configuration is shown in Figure 2.3 (c) & (d). Here, one of the ESS is connected with the DC bus through DC- DC converter and the other ESS is directly connected. These configurations have partial control over the ESS voltage though it's not the efficient. The connection of the battery to the DC grid without a DC-DC converter as shown in Figure 2.3 (d), will increase the stress on the battery during high current fluctuations.

### 2.2.3 Full-active HESS Configuration

The bi-directional converters effectively controls the power output from the HESS in full-active configurations. In these configurations, the effective use of HESS is possible. Figure 2.3 (e) (f) shows the full-active configurations.

In configuration (e) utilize two independent bidirectional converters for the HESS. The advantage is better modularity and independent control is applicable. However, the space required and cost will be higher compared to other configurations. To overcome these drawbacks, multi input single output (MISO) converters are used as shown in Figure 2.3 (f). The advantage is less space and cost effectiveness compared to configuration (e).

**Table 2.2** Comparisons of HESS configurations

<b>Configuration</b>	<b>(a)</b>	<b>(b)</b>	<b>(c)</b>	<b>(d)</b>	<b>(e)</b>	<b>(f)</b>
Number of converters	0	1	1	1	2	1
Controlled DC link voltage	No	Yes	Yes	Yes	Yes	Yes
Controlled battery current	No	No	Yes	No	Yes	Yes
Controlled SC current	No	No	No	Yes	Yes	Yes
DC link voltage swing	less	less	High	less	High	High

The merits and demerits of different schemes of HESS are summarized in Table 2.2. The comparisons are made based on number of converters used, voltage control and HESS current control. Based on the above comparison, configuration (f) provides freedoms to control the power from an individual energy storage systems.

The main advantages of configuration (f) are: (i) decreases the system size (ii) minimization of converter cost (iii) improved utilization ratio of HESS.

## 2.3 HESS Power Decomposition Methods

The power decomposition methods for HESS determines the overall HESS performance. The main aim of power decomposition method is to share the steady state power to battery and transient power requirement to SC. The optimal design of power decomposition methods are important for better utilization of HESS. The design of power decomposition method will also affect the size of the system. The few power decomposition methods are summarised in following sections.

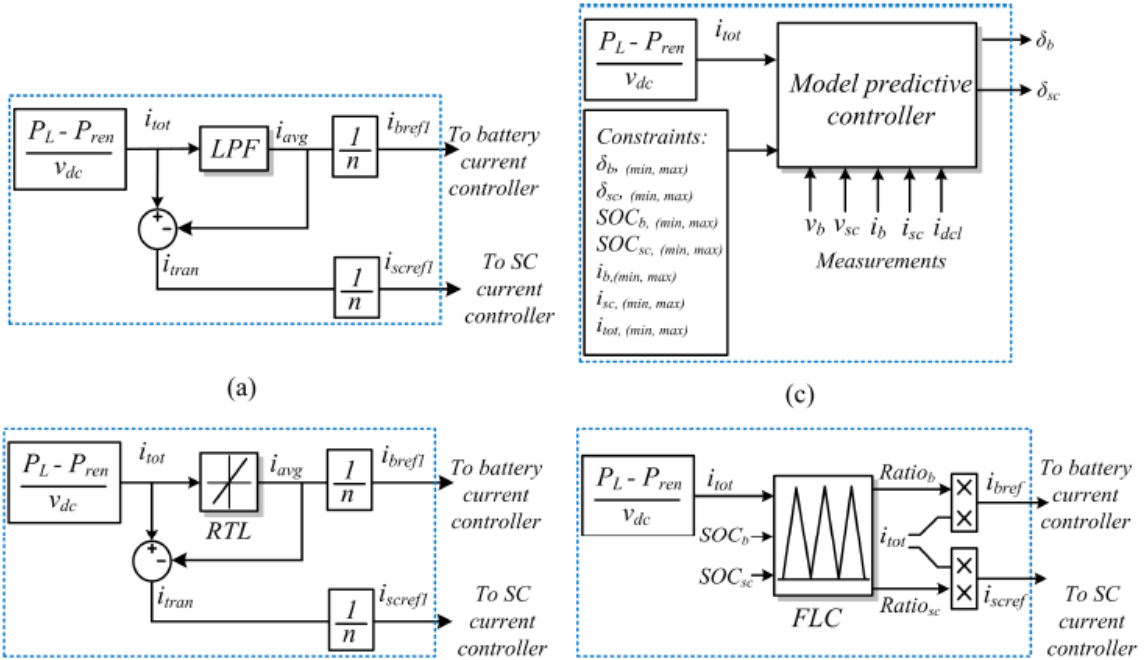


**Figure 2.4:** (a) Block diagram of LPF based power sharing method (b) Rate-limiter based power sharing method (c) MPC based power sharing method (d) FLC based power sharing method.

### **2.3.1 LPF/HPF Based Power Sharing Method**

Power sharing methods based on low pass filter (LPF) or high pass filter (HPF) are among the most common and simplest to implement HESS. The total current demand was transferred through the LPF/HPF in this method to produce battery and SC reference currents. By using renewable power generation and load power demand to calculate total current demand. To design cut-off frequency of LPF/HPF is based on dynamic characteristics of ESSs. In general, the LPF based method cut-off frequency depends on dynamic behaviour of ESSs with slow response time. The LPF based architecture is presented in Figure 2.4 (a) [53] [54]. After LPF, the current references are fed to the appropriate current controllers.

### **2.3.2 Rate limiter Based Power Sharing Method**

The rate limiter based power sharing method block diagram is represented in Figure 2.4 (b). The total HESS current demand is passed through the rate limiter block in this method. The ramp rate of total current demand is regulated with a rate-limiter block. The battery current controller receives the slower ramp rate, while the SC controller receives the quicker ramp rate. In [55], a double stage rate limiter control technique for HESS has been presented. The current references in the proposed schemes are determined based on battery SOC and load power demand. The generated current references are then fed to the PI controllers, which handle both the battery and the SC currents. The proposed scheme reduces the charge/discharge rate of the battery. As a result, the battery life cycle is improved.

### **2.3.3 MPC Based Power Sharing Method**

The MPC based power sharing method for HESS control is presented in Figure 2.4(c) [56]. In MPC control scheme, the optimal switching states are determined by defined control horizon. The switching states are calculated by using cost function and constraints. The system constraints and cost function will determine the effective power sharing between ESSs. In MPC control, various weighting values can be assigned to the system parameters to be controlled. However, MPC control method requires larger computational resources compared to conventional power sharing methods.

### 2.3.4 Fuzzy Logic Control (FLC) Power Sharing Methods

The FLC based power sharing method architecture is presented in Figure 2.4 (d) [57, 58]. The FLC is intelligent control method to control the complicated parameters. In FLC method, fuzzy rules are developed based on characteristics of ESSs. The slow varying current demand allocated to battery and transient current demand allocated to SC. In generally, the FLC generates ratios for battery and SC energy storage devices. The fuzzy rules determines the sharing between battery and SC based on load demand and SOCs of the storage devices.

## 2.4 Control Methods for HESS

Several control strategies are being utilized for HESS such as Artificial Intelligence (AI) methods like FLC, Artificial Neural Networks (ANNs) and Genetic Algorithm (GA) [59]. Based on above control approaches, the SC supports high frequency power fluctuations and battery supports average or low frequency power fluctuations [60].

Several multiple input topologies have been proposed which can interface multiple sources with contrasting characteristics to a common load. In [61], multiple ESSs are interfaced to a three-winding high frequency transformer wherein each source is connected through a full-bridge circuit. For battery-supercapacitor HESS connected number of switches required is eight which may affect the overall efficiency as far as dc microgrid application is concerned. An Isolated multiport dc-dc converter was presented in [62] [63] which can manage power from multiple energy sources to a common load. But power flow between the sources, if they were replaced by ESSs, was not explored. Even though isolated converters support wide range of voltage levels as well as safety in the form of isolation, energy management of multiple sources is difficult compared to that of non-isolated converters.

A number of multiple input non-isolated dc-dc bidirectional converters for interfacing multiple sources can be found in literature which offers far more flexibility in implementation and power management than isolated ones [64]-[76]. In [64] a procedure for developing all possible double-input single-output dc-dc converters was described and was experimentally verified for a system with battery as one input. But bidirectional power flow between the two input ports was not considered which is necessary for HESS in microgrid applications. A multi-input dc-dc converter for various energy sources of diverse

characteristics was proposed in [65] but with no power sharing option between the input sources.

Benfei Wanga et al. [66] has presented single inductor based multi-port converter for HESS. The computation and controller effort are much more since the paper uses model predictive control. More over SOC based analysis is required for the validity of control strategy.

Rasoul Faraji et al. [67] proposes a multiport hybrid energy system with PV and battery. The independent use of battery alone will increase the stress on the battery. Also the proposed converter is not suitable for SC applications. Yusuke Sato et al. [68] also proposing multi-port converter for PV and battery. The proposed circuit able to integrate battery with PV, however during various disturbances, the stress on the battery will be high. Zhehan Yi et al. [69] developed Unified control of Energy management system for PV-Battery based grid for both grid connected and islanded operation has been presented. In the proposed control method, battery balances the AC micro grid and DC micro grid power in all different operating conditions. This increases the battery stress, system cost and life cycle of battery. A high efficiency dual input interleaved converter was proposed in [74] which is especially suitable for energy storage sources. However, Dual input interleaved converter circuit requires eight switches makes the control strategy to be complicated. Few multi-input converters for grid-tied and/or solar applications are reported in [75]-[77]. Similarly, multi-input converters are also widely used in hybrid electric vehicle (HEV) applications as in [78]-[84]. However, in all above multiple input converter topologies does not maintain  $SOC_{SC}$  in the predefined limits and protecting SC from over charge and discharge is difficult.

## 2.5 Model Predictive Control

The MPC is popular control method for process control applications. The MPC method is also widely used for power electronics converter control. The MPC is a promising new technique that predicts the future states of a system using a discrete model of the system and present state of the system, to get optimal control action to be performed at every sampling instant. MPC can deal with possible interface, noise, etc. in the system and improve the robustness of the system [85]. The MPC based control strategy for different converters are proposed in [86-92]. In [86-88], proposed MPC method involves operations on a large number of matrices which leads to high computational time and complexity. To overcome

this [89-91] have proposed a relatively low complex MPC control strategy with dynamic reference generation [92] with a two-loop control strategy but the SC voltage variation not considered.

SC voltage is assumed to be constant in all these works although it fluctuates rapidly with the charge/discharge current and if the SC voltage goes below a particular value the converter operation will be failed and there is a prospect of getting overcharged when it is operating in regenerative mode. Hence SC voltage should be maintained in particular limits for reliable operation [93, 94].

## 2.6 Summary

The ESSs are the important part of microgrids. The ESSs are balance the flow between power generation and load demand. For effective system operation the choice of converter schemes of ESSs and their converters plays a vital role. In this chapter, a detailed literature review of ESSs have been presented. The state of art of power sharing methods have been analysed.

# **Chapter-3**

## **Optimum Design and Analysis of a Dynamic Energy Management Scheme for HESS in Renewable Power Generation Applications**

## Chapter-3

# Optimum Design and Analysis of a Dynamic Energy Management Scheme for HESS in Renewable Power Generation Applications

### 3.1 Introduction

In this chapter, the proposed control scheme implemented for the integration of HESS in DC microgrid applications. The proposed control scheme design a new SC system by using uncompensated power from battery system to improve the overall performance of HESS. The modelling, analysis, stability and control of a two-input bidirectional DC-DC converter for HESS in DC microgrid is presented in this chapter. The proposed control scheme is realized in MATLAB/Simulink and results are presented for different case studies. Experimental results are presented for two-input bidirectional converter at the step change in PV generation and load demand.

### 3.2 Modelling of system components of DC microgrid

#### 3.2.1 Modelling of PV Panel

The PV panel converts light energy in to electrical energy. PV cell is the basic unit of PV panel. The PV cells are connected in series and parallel to form a PV panel. The PV panels are further connected in series and parallel to form a PV array. The PV array is designed based to meet the necessary voltage and current ratings. The electrical equivalent of PV array is shown in Figure 3.1(a).

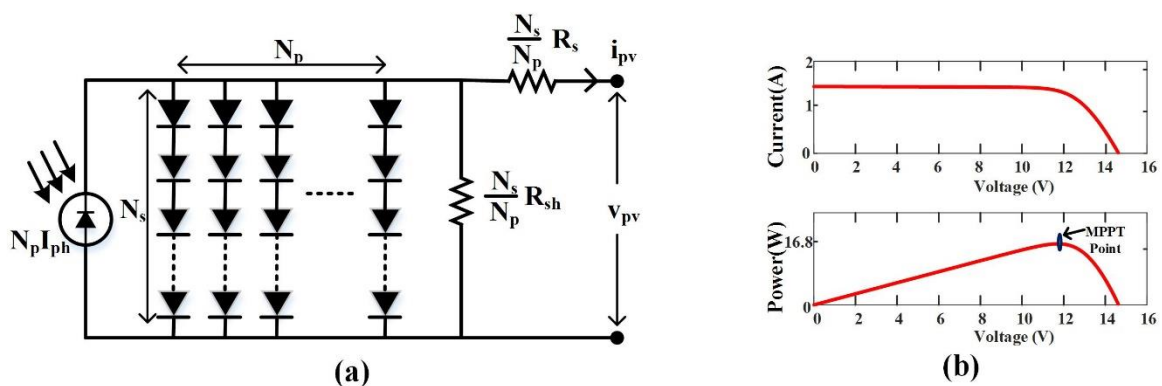


Figure.3.1 (a) Equivalent circuit representation of PV array (b) I-V & P-V Characteristics of PV

The characteristics equation is presented here is based on a PV array with a single diode model. The current and voltage properties of PV cells are nonlinear in general i.e. shown in Figure 3.1 (b). The characteristics equation of PV array is given below.

$$i_{pv} = N_p I_{ph} - N_p I_{rs} \left( e^{\frac{q(\frac{V_{pv}}{N_s} + \frac{i_{pv}}{N_{pv}})}{AKT}} - 1 \right) - \frac{\frac{N_p V_{pv}}{N_s} + i_{pv} R_s}{R_{sh}} \quad (3.1)$$

Where  $N_p$ : Total number of Parallel connected PV cells,  $N_s$ : Total number of series connected PV cells.  $I_{ph}$  is the total photo-current generated from PV array.  $I_{rs}$  represents reverse saturation current of PV cell.  $R_s$  and  $R_{sh}$  represent the series and parallel resistances.  $A$  is the diode ideal factor,  $T$  is PV cell's working temperature and the  $K$  is the Boltzmann's constant ( $1.38 \cdot 10^{-23} \text{ J/k}$ ).  $V_{pv}$  and  $I_{pv}$  represent PV array voltage and current. The current equation of PV panel is non-linear and dependent on weather conditions like insolation and temperature. To find the maximum power point on non-linear PV curve maximum power point tracking algorithm is engaged.

### 3.2.2 P & O MPPT Algorithm:

The main objective of MPPT algorithm is to extract maximum power from the PV Panel. It is the conventional MPPT algorithm. In this method extracted power is observed by varying the duty based on comparing the power output. The change in power ( $\Delta P_{PV}$ ) and voltage ( $\Delta V_{PV}$ ) between two samples are recorded and compared to generate the duty for the next sample. As, it can also be observed from the flowchart of P&O algorithm shown in Figure 3.2 (a), when both  $\Delta P_{PV}$  and  $\Delta V_{PV}$  are positive or  $\Delta P_{PV}$  and  $\Delta V_{PV}$  are negative duty factor increases while, alternation of positive and negative sign in  $\Delta P_{PV}$  and  $\Delta V_{PV}$  leads to reduces of duty factor.

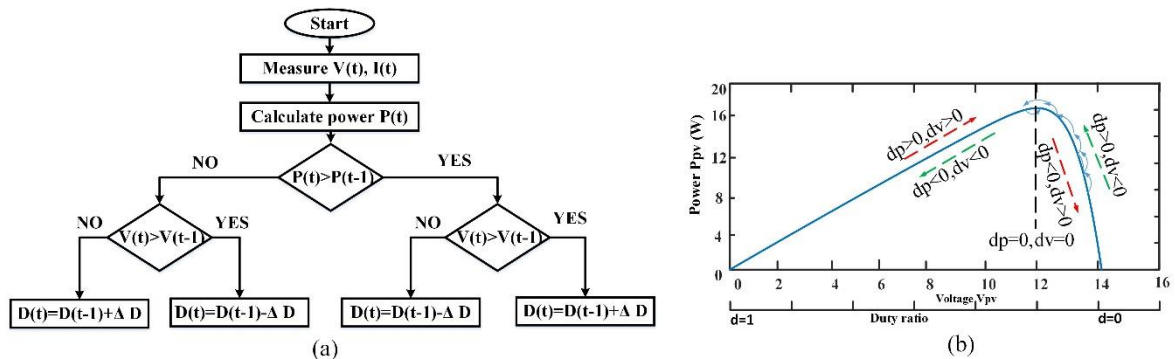


Figure 3.2 (a) P & O MPPT flowchart (b) P-V characteristics

### 3.2.3 Modelling of Battery

There are basically three types of batteries represented [95, 96]. They are electrical circuit based battery model [97, 98], electro chemical based battery model [99], experimental circuit based battery model [95, 96]. The basic electrical circuit battery model is shown in Figure 3.3. In electrical circuit based battery model look like series combination of voltage source and resistance. In this electrical circuit model, nonlinear mathematical equation (3.2) represents the terminal voltage of battery. The internal resistance ( $R$ ) of battery is constant, independent of charging/discharging current magnitude in this model. The terminal voltage of battery depends on electric charge of the battery. The characteristic equation is same for both charging/discharging mode operation of battery.

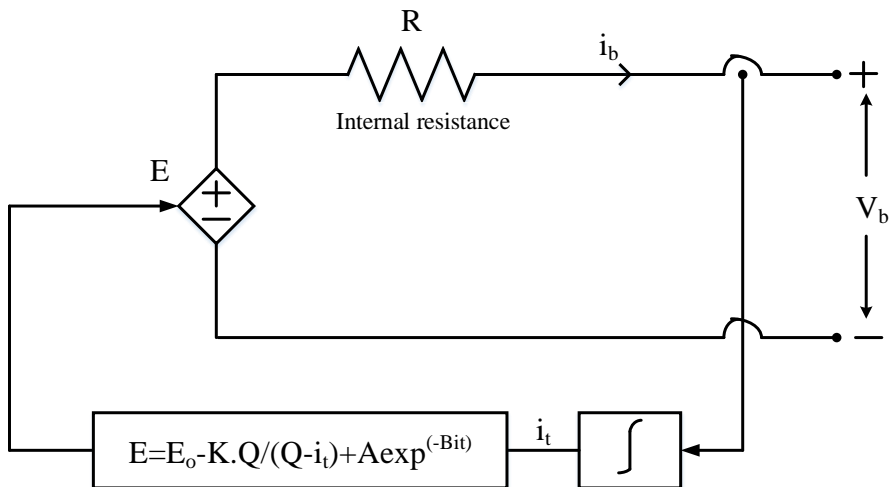


Figure 3.3. Electrical equivalent circuit of lead-acid battery

$$E = E_o - K \frac{Q}{(Q - i_t)} + A e^{-B i_t} \quad (3.2)$$

$$i_t = \int_0^t i_b dt \quad (3.3)$$

$$V_b = E - R i_b \quad (3.4)$$

Where  $E$ : no-load voltage,  $E_o$ : nominal voltage,  $K$ : polarization voltage,  $Q$ : charge capacity of battery,  $i_b$ : battery current  $V_b$ : battery terminal voltage,  $A$ : exponential zone amplitude and  $B$ : exponential time zone constant. The left over parameters in eq (3.2) can be same specifications given in [98].

### 3.2.4 Modelling of SC

SC stores the energy in the form of charge difference appearing on its positive and negative plates separated by some distance. Supercapacitors also called as double layer capacitors is similar to conventional capacitors except that it has high capacitance value due to its bigger plate area and less distance between plates as:

$$C = \varepsilon \frac{A}{d} \quad (3.5)$$

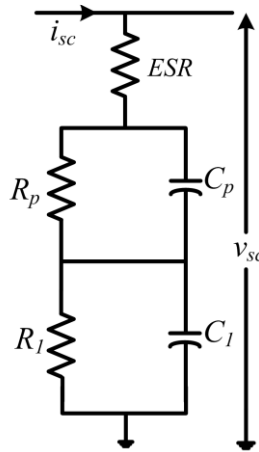


**Figure 3.4** Equivalent circuit representation of SC

The SC is used mostly where fast charging/discharging processes are to be done and it provides high current pulse [100]. As seen from eq. (3.5) it is clear that the design of Electric Double Layer Capacitors (EDLCs) are such that their surface area of the electrode is more with thin high-permittivity dielectric between them so as to have higher value of capacitance. The material of the electrode and electrolyte affects the performance of supercapacitors. Use of porous carbon as the current collector, activated carbon electrodes, metal-oxide electrodes and electronically conducting polymer electrodes [101].

High energy density and high capacitances make activated carbon electrodes as the most commonly used electrode material. The carbon could be in different forms such as graphene, carbon nano tubes, etc [101]. Their capacities are about a thousand times compared to those of conventional capacitors making large amount of energy to be stored in them.

There are three electrical equivalent circuit models of SC. They are series combination of resistance and capacitance (series RC) model [102], parallel combination of

resistance and capacitance (parallel RC) model [102,103] and series parallel combination of resistance and capacitance (series-parallel RC) model [104,105]. Among the different equivalent circuits, simplest one is series RC model. The dynamic behaviour of SC determined by using resistance and capacitance. In general, series resistance in equivalent circuit of SC determines the equivalent series resistance (ESR). It reflects the losses during charging/discharging process of SC. If the charging current abruptly drops to zero in a series RC model, the SC voltage gradually decreases and takes some time to achieve steady state [103]. This behaviour of SC is not discussed in series RC model.

This problem is somewhat discussed in parallel RC model of SC. The parallel RC model is made up of two or more series RC circuit models that are connected in parallel. The various time constants for various RC models. As a result, during charging/discharging operation each RC branch in a parallel RC model behaves differently. As compared to the series RC model, the dynamic behaviour of the parallel RC model of SC is more accurate.

In our study we used series-parallel model of SC as shown in Figure 3.4 ESR in figure 3.4 represents series resistance which represents the ohmic losses during charge and discharge operation of SC. In Figure 3.4,  $R_p$  and  $C_p$  represents parallel resistance and capacitance respectively.  $R_1$  represents the self-discharge rate of SC and  $C_1$  represents the actual storage capacitance of SC.  $V_{sc}$  and  $i_{sc}$  represents the terminal voltage and output current from SC respectively. The model parameters calculations are discussed in detail in [105].

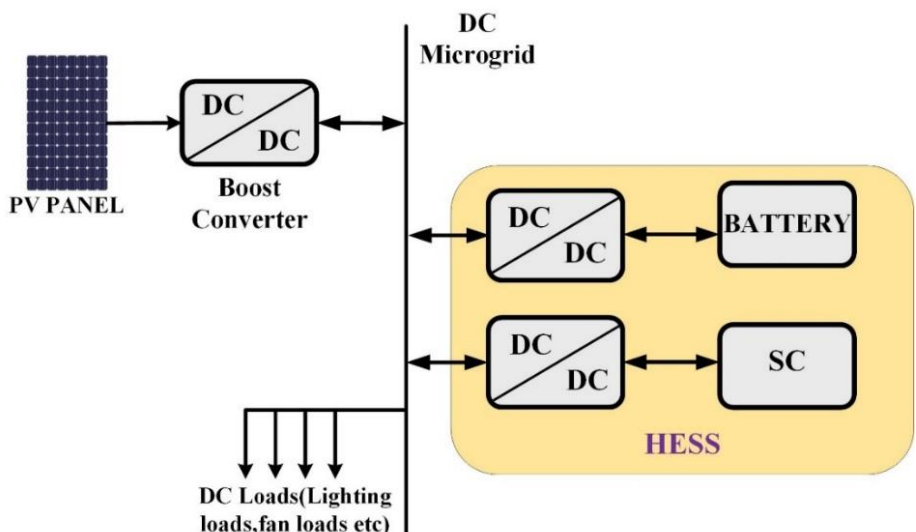


Figure 3.5: PV based microgrid aided by HESS

### 3.3 HESS Supported RES Configuration

The most commonly used configuration of HESS, which has the leverage of attaining independent control on both battery and SC is as shown in Figure 3.5. In this active parallel configuration of HESS, it is possible to exchange energy between the component ESSs, for example, the battery ESS can charge supercapacitor ESS or vice versa. For the DC microgrid, PV is the main source of power and connected with battery and supercapacitor. The boost converter is used for maximum power point (MPP) extraction and interfacing of PV to DC microgrid. By utilizing the HESS system including battery-SC bank, mismatch among source power and load power is settled. A two-input 4 switch H-bridge bidirectional converter is used to connect HESS with DC microgrid. With the usage of the 2-input bidirectional converter, HESS charging/discharging is controlled. At the point of mismatch between source power and load power, HESS take care of the surplus or deficient power at the set reference of grid voltage.

### 3.4. Operation of microgrid with HESS

The operation of microgrid with HESS is cleared up in this subsection and two-input bidirectional converter is used to HESS (charging/discharging) control. The system involves 4 bidirectional switches which are organized in the topology of H-bridge showed up in Figure 3.6. Battery voltage is selected to be less than that of DC grid voltage but greater than SC voltage in this converter topology. High frequency inductors  $L_B$  and  $L_S$  are connected to the battery and SC legs respectively. Different modes of operation are explained in the following sections.

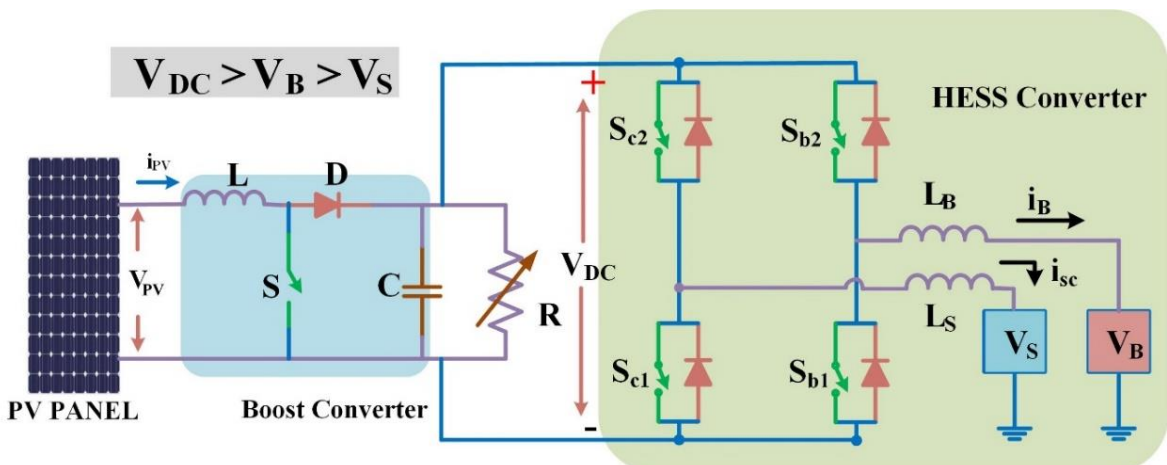
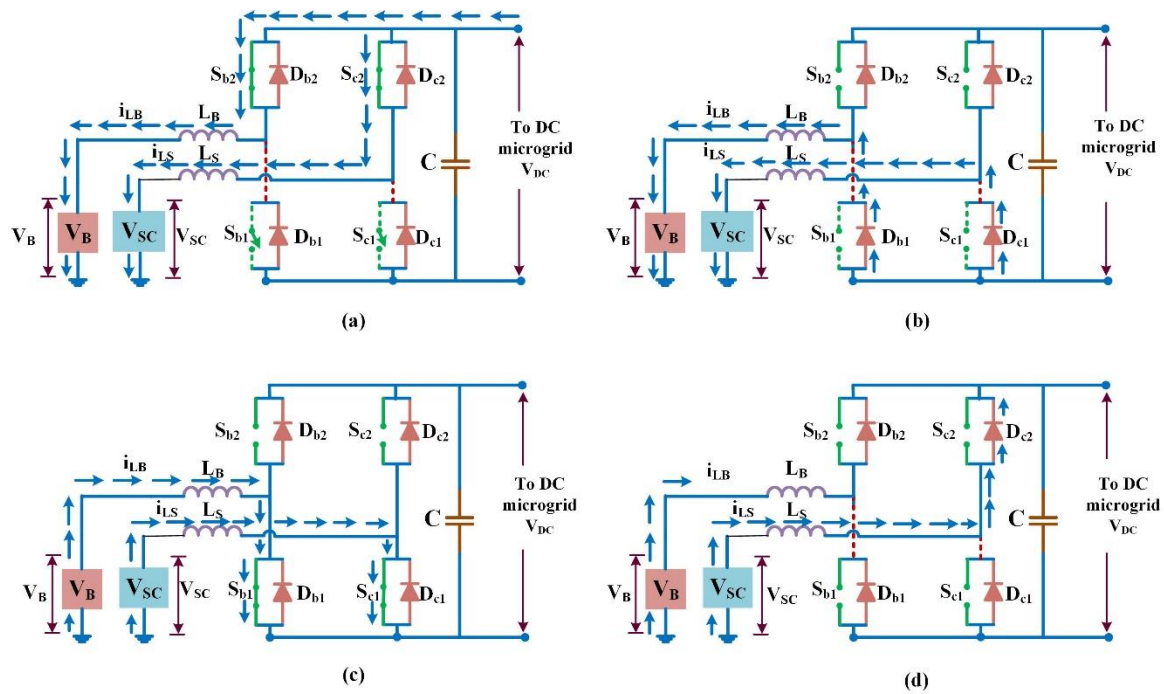


Figure 3.6: DC microgrid setup powered by PV source and supplemented by HESS

### 3.4.1. HESS Charging Mode

Whenever generated PV power exceeds the load requirement or load demand decreases, so excess power existing in the DC microgrid which results DC grid voltage increases. This excess amount of power will charge both battery and supercapacitor to stabilize DC microgrid. Hence in this mode power flows from DC microgrid to HESS. The converter operation in this mode can be divided in to two time intervals as shown in Figure 3.7. During the time interval  $T_1$ , switches  $S_{b2}$  and  $S_{c2}$  as switches are operated with duty cycle, charging both the inductors  $L_B$  and  $L_S$  by corresponding sources  $V_B$  and  $V_{SC}$ . Current increases with a slope of  $(V_{DC}-V_B)/L_B$  and  $(V_{DC}-V_{SC})/L_S$  respectively as demonstrated in Figure 3.8. At the end of this interval (During  $T_2$ ), both the switches are turned off providing freewheeling path for  $i_{LB}$  and  $i_{LS}$  through  $D_{b1}$  and  $D_{c1}$  respectively.



**Figure 3.7** Equivalent circuit of bidirectional DC-DC Converter for charging/discharging mode.

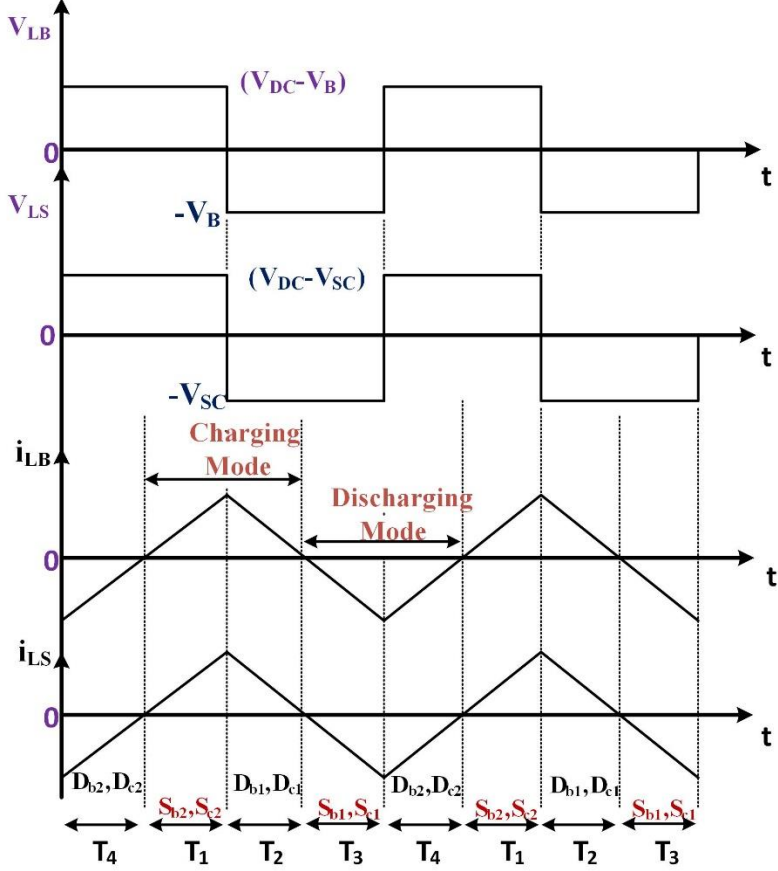


**Figure 3.8** Steady state waveforms for HESS charging/discharging mode

$$V_B = d_B \cdot V_{DC} \quad (3.6)$$

$$V_{SC} = d_{SC} \cdot V_{DC} \quad (3.7)$$

Where,  $d_B$  and  $d_{SC}$  are the duty cycles. Transfer of energy from DC grid to HESS. The DC grid has extreme potential than the HESS. In order to HESS charge, then the converter is operated as buck mode.

### 3.4.2. Discharging mode of HESS

DC microgrid voltage decreases if load exceeds PV generation capability or when PV generated power falls due to reduced solar irradiation. During this time interval power has to be supplied by HESS. By operating on devices  $S_{b1}$  and  $S_{c1}$ , power flows from HESS to DC microgrid in this mode, by properly controlling bidirectional converter. During the time interval  $T_3$ , switches  $S_{b1}$  and  $S_{c1}$  are gated-on, inductors ( $L_B$  and  $L_S$ ) stores energy in opposite direction, reverse currents ( $i_{LB}$  and  $i_{LS}$ ) increases with a slope of  $V_B/L_B$  and  $V_{SC}/L_S$  respectively as demonstrated in Figure 3.8. After end of this time period  $T_3$  (During time period  $T_4$ ) as sum of battery and inductor voltages exceeds DC microgrid voltage, so power

flows from HESS to DC microgrid current directions of each time interval as demonstrated in Figure 3.7.

$$V_{DC} = \frac{V_B}{1-d_B} \quad (3.8)$$

$$V_{DC} = \frac{V_{SC}}{1-d_{SC}} \quad (3.9)$$

Since  $S_{b1}$ ,  $S_{b2}$ ,  $S_{c1}$ , and  $S_{c2}$  are the switches which are switched in the complimentary way. For each switching leg, only 1 gate circuit is required.

### 3.5 Proposed Control Strategy of HESS

The control block diagram of conventional and proposed control schemes are depicted in Figure 3.9 and Figure 3.10 respectively. To the proportional integral (PI) controller, the reference ( $V_{DC,ref}$ ) and actual ( $V_{DC}$ ) voltages of grid are contrasted with each other in both schemes and the dissimilarity in voltages is proceed. From the HESS the controller is generating total reference current ( $i_{tot}$ ) required and which is minimizing the difference in voltages. In the conventional scheme total current is decomposed into frequency components as low and high range, to the battery and SC which is given as reference currents respectively and it is depicted in Figure 3.9. The reference current of SC consists of a component with high frequency and the battery current with error component in the proposed control scheme which is explained below,

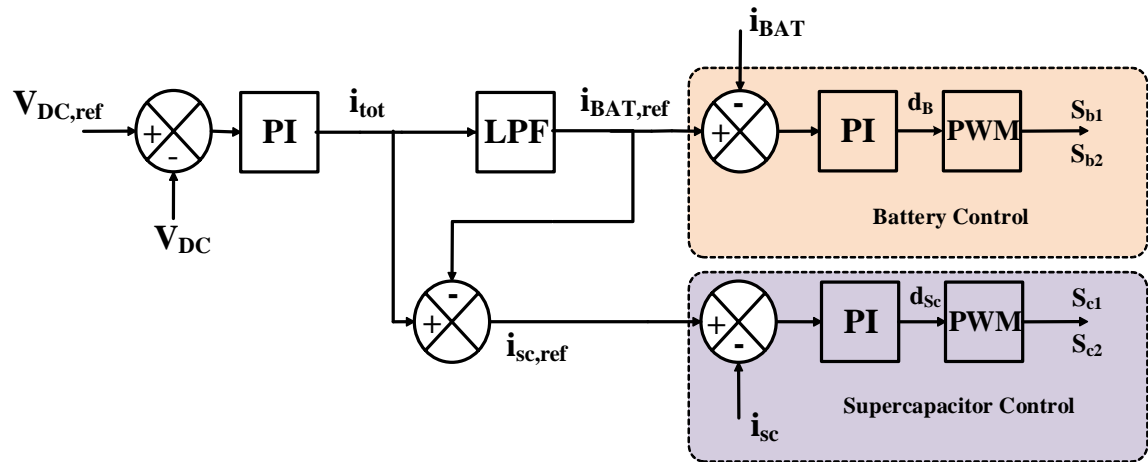


**Figure 3.9:** Control block diagram of conventional control schemes

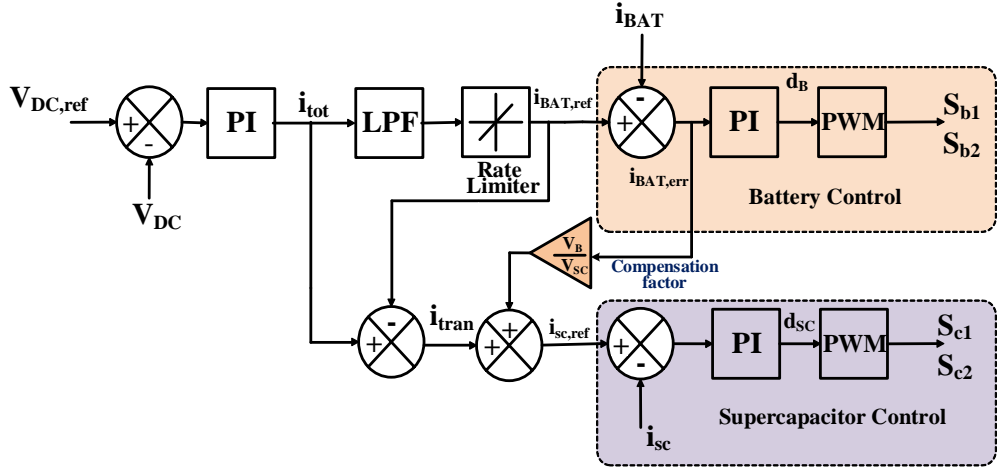


**Figure 3.10:** Control block diagram of proposed control schemes

The component ( $i_{lf}$ ) with low frequency is derived from  $i_{tot}$  as derived as follows,

$$i_{lf} = f_{lf}(i_{tot}) \quad (3.10)$$

Where, low pass filter function is represented as  $f_{lf}(.)$ . A rate limiter ( $f_{rl}$ ) is introduced for battery current charge/discharge rate limit which is depicted in Figure 3.10. The current signal reference of rate limiter output is formulated by,

$$i_{BAT,ref} = f_{rl}(i_{lf}) \quad (3.11)$$

The difference in currents ( $i_{BAT,err}$ ) is given to the PI controller after the battery current with reference and actual are contrasted with each other. The controller generates the control signal ( $d_B$ ) to minimize the dissimilarity in the currents. The pulse width modulated (PWM) pulses are generated to the switches ( $S_{b1}, S_{b2}$ ) in the converter of battery to the PWM generator, this duty ratio which is shown in Figure 3.10. In DC-DC converter due to the electrical inertia and slow dynamics of battery system the converter may not follow instantly with battery reference current ( $i_{BAT,ref}$ ). Therefore, the uncompensated power is observed in battery system is given by

$$i_{tran} = i_{tot} - i_{BAT,ref} \quad (3.12)$$

$$P_{B\_Uncomp} = (i_{BAT,ref} - i_{BAT}) \cdot V_B \quad (3.13)$$

Where  $i_{tran}$ : transient component of current,  $P_{B\_Uncomp}$ : battery uncompensated power. In the proposed control strategy  $P_{B\_Uncomp}$  used to enhance the performance of SC. Therefore, the supercapacitor reference current ( $i_{SC,ref}$ ) is formulated as follows,

$$i_{SC,ref} = i_{tran} + (i_{BAT,ref} - i_{BAT}) \frac{V_B}{V_{SC}} \quad (3.14)$$

The error is passed to the controller after the actual and references of supercapacitor currents are contrasted with each other. The error is minimized when the PI controller generates the control signal  $d_{SC}$ . To generate the pulses of PWM corresponding to SC switches such as  $S_{c1}, S_{c2}$  this control signal is given to the PWM generator which is shown in Figure 3.10.

$$i_{SC,ref} = i_{tran} + i_{BAT,err} \cdot \frac{V_B}{V_{SC}} \quad (3.15)$$

Where  $i_{BAT,err}$ : battery error current is the difference between actual and references of battery is given by

$$i_{BAT,err} = i_{BAT,ref} - i_{BAT}$$

### 3.6. Design of Proposed Controller for HESS

The design of proposed controller for HESS is clarified [106]. In the unified controller a single controller is utilized to trigger the two control switches. For both charge (buck) and discharge (boost) modes [107], boost mode of operation is considered to design the controller. The sub-harmonic oscillations are kept then, the current control loop bandwidth of supercapacitor controller is restricted to 0.1667 times switching frequency ( $f_{sw}$ ) [108]. Here, the switching frequency is equivalent to 10 kHz. The battery current controller Bandwidth (BW) is chosen with the end goal that high frequency transients are redirected to supercapacitor, i.e. at  $f_{sw}/10$ . In stable region to work the system, the bandwidth of the converter must be worked significantly lesser than the right half plane zero frequency ( $f_{rhpz}$ ) [109] of the supercapacitor.

$$f_{RHPZ} = \frac{(1-d_{SC})^2 R}{2\pi L_S} \quad (3.16)$$

Where R: load resistance,  $L_S$ : SC inductance and  $d_{SC}$ : duty cycle of SC leg. The outer voltage control loop is slower than the inner current control loop; than the voltage control loop bandwidth is picked lesser than that of the SC current control loop.

#### 3.6.1. Design of Supercapacitor Current Controller

Figure 3.11 shows the block diagram of the current controller of the supercapacitor. The voltage control loop produces the supercapacitor reference current ( $i_{sc,ref}$ ) in the controller. In

the current control loop, reference current is contrasted with the actual current [110]. After perturbation and linearization of state equations, duty cycle to SC current transfer function is given below,

$$G_{id\_SC} = \frac{\hat{i}_{SC}}{\hat{d}_{SC}} = \frac{V_{DC}CS + 2\frac{V_{DC}}{R}}{L_SCS^2 + \frac{L_S}{R}S + (1-d_{SC})^2} \quad (3.17)$$

Here, the duty cycle of small perturbations as  $\hat{d}_{SC}$ , SC inductor current as  $\hat{i}_{SC}$ . The PI control transfer function of SC current loop is formulated as follows,

$$G_{pi,SC} = K_{p,SC} + \frac{K_{i,SC}}{S} \quad (3.18)$$

Here, proportional and integral gains of the PI controller is represented as  $K_{p,SC}$  and  $K_{i,SC}$ .

Controller parameters ( $K_{p,SC}$  and  $K_{i,SC}$ ) for inner current loop is designed based on above model with bandwidth of 1.67 kHz and phase margin of 59.2°. Bode plot for compensated and uncompensated transfer functions is shown in Figure. 3.12. The controller parameters are designed and fine-tunes using SISO tool in MATLAB software. The proportional and integral constants obtained are 0.0088 and 80.689 respectively.

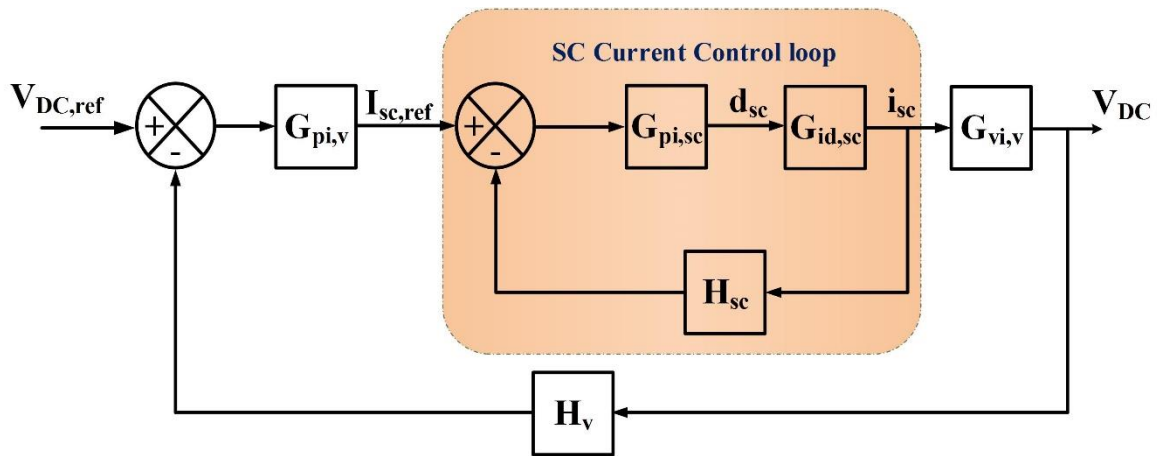
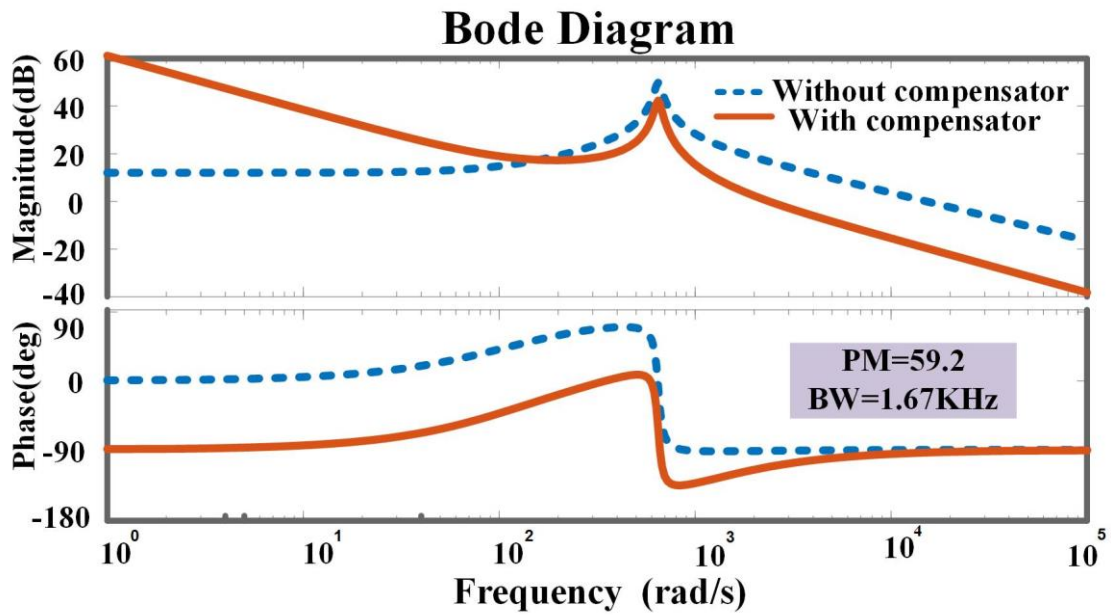


Figure 3.11: SC controller Block diagram



**Figure 3.12:** Bode plot of inner current controller of SC control logic with controller.

The open loop transfer function of SC current controller can be calculated based on the following equation,

$$G_{ol,SC} = G_{pi,SC} \cdot G_{id,SC} \cdot H_{SC} \quad (3.19)$$

Here, gain of the current sensor is specified as  $H_{SC}$ .

### 3.6.2 Design of HESS Voltage Controller

The voltage control loop, SC current to voltage small signal transfer function are obtained in equation (3.20).

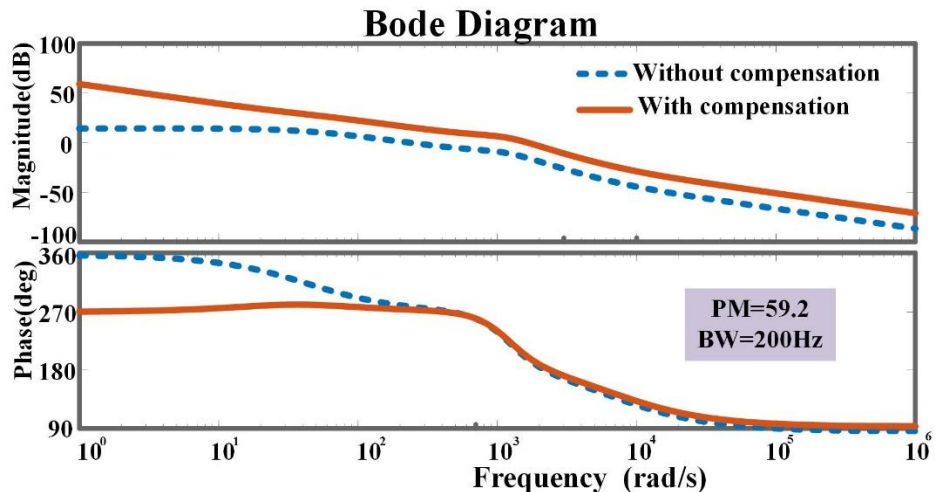


**Figure 3.13:** Bode plot of outer voltage controller of supercapacitor control logic with controller.

$$G_{vi,v} = \frac{\hat{V}_{DC}}{\hat{i}_{SC}} = \frac{R(1-d_{SC}) \cdot (1 - \frac{L_{SC}}{R(1-d_{SC})^2} S)}{2 + RCS} \quad (3.20)$$

Here, the output voltage small perturbation is specified as  $\hat{V}_{DC}$ . The PI control transfer function of voltage control loop is given as follows,

$$G_{pi,v} = K_{p,v} + \frac{K_{i,v}}{s} \quad (3.21)$$

Here, the PI controller gains as  $K_{p,v}$  and  $K_{i,v}$ . Open loop transfer function of voltage controller is equated as follows,

$$G_{ol,v} = G_{pi,v} \cdot G_{cl,sc} \cdot G_{vi,v} \cdot H_v \quad (3.22)$$

$$\text{Here, } G_{cl,sc} = \frac{G_{pi,sc} \cdot G_{id,sc}}{1 + G_{pi,sc} \cdot G_{id,sc} \cdot H_{sc}} \quad (3.23)$$

Here, gain of the voltage sensor is represented as  $H_v$ .

Proportional constants of outer voltage loop is also designed based on averaged state space model. Bandwidth has to be less than right half plane zero. The designed voltage controller has a bandwidth of 200Hz and phase margin 59.2°. Bode plot for compensated and uncompensated transfer functions shown in Figure 3.13. Proportional and integral constants are 5.96 and 175 respectively.

### 3.6.3 Battery Current Controller Design

Figure 3.14 depicts the block diagram of the battery current controller. The duty cycle to battery current transfer function for battery stage is given by,

$$G_{id,BAT} = \frac{\hat{i}_{BAT}}{\hat{d}_B} = \frac{V_{DC}CS + 2\frac{V_{DC}}{R}}{L_BCS^2 + \frac{L_B}{R}S + (1-d_B)^2} \quad (3.24)$$

Here, small perturbations in duty cycle as  $\hat{d}_B$ , battery inductor current is represented as  $\hat{i}_{BAT}$ .

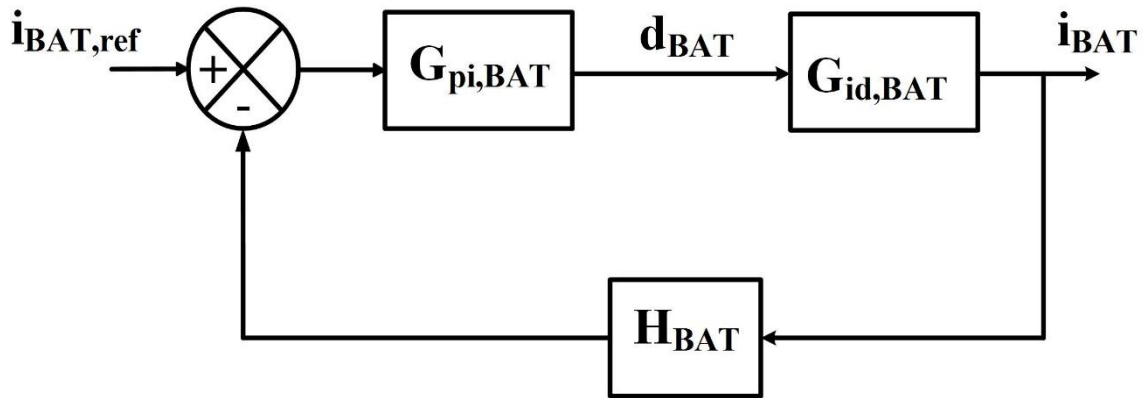


Figure.3.14: battery current controller block diagram

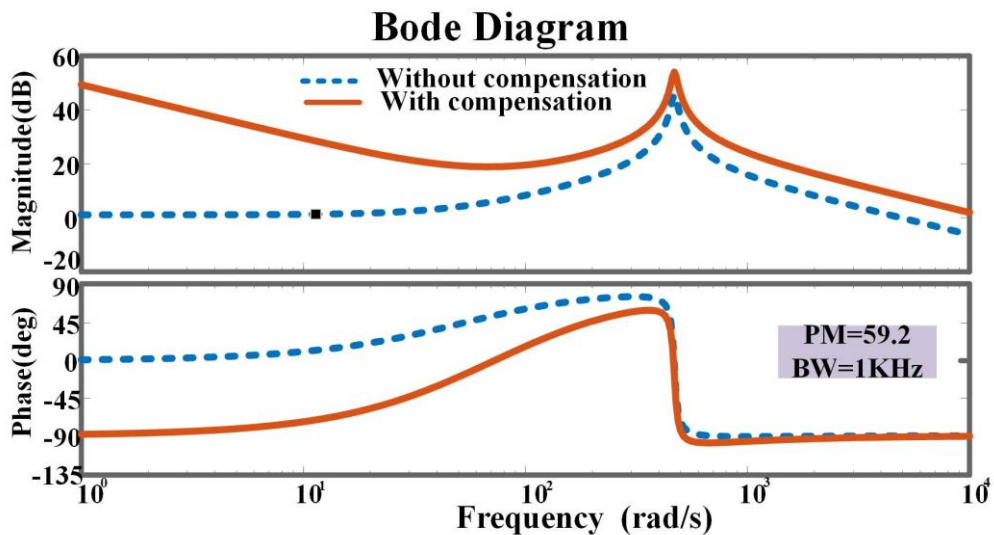


Figure.3.15: Bode plot of battery current controller

The PI control transfer function of battery current control loop as follows,

$$G_{pi,BAT} = K_{p,BAT} + \frac{K_{i,BAT}}{s} \quad (3.25)$$

Here, proportional and integral gains of the PI compensator as  $K_{p,BAT}$  and  $K_{i,BAT}$ .

The open loop transfer function of current control loop is formulated as follows,

$$G_{ol,BAT} = G_{pi,BAT} \cdot G_{id,BAT} \cdot H_{BAT} \quad (3.26)$$

Here, gain of the current sensor is represented as  $H_{BAT}$ .

PI controller to regulate battery current is designed based on above transfer function. Bandwidth of the controller is made less than that of supercapacitor controller stage. The

designed controller has a bandwidth of 1 kHz with phase margin of 59.2°. Bode plot of compensated and uncompensated plant is shown in Figure 3.15. The proportional and integral constants obtained are 0.1404 and 78 respectively.

### 3.7. Simulation Results and Discussion

In this segment, the results of the conventional and proposed control schemes are displayed for four test cases. The nominal parameters for simulation study are presented in Table 3.1. The entire model is implemented using MATLAB. The model consists of two bidirectional converters - one for battery and other for SC. The PV array is a unidirectional, which is connected to the boost converter. The four operating cases are presented in the following sections for step change in PV generation and load demand.

#### 3.7.1 Case-I: Step increase in PV generation

The simulation results for step increase in PV generation, conventional and proposed control schemes are shown in Figure 3.16 and Figure 3.17 respectively. In both the control schemes, due to atmospheric variations power produced by the PV panel increases from 96W to 192W at  $t=0.3$ sec. Due to this PV current increases from 4A to 8A at  $t=0.3$ sec. In this case load power requirement is constant at 96W. As PV power is more than the load power requirement, DC grid voltage increases more than 48V. Immediately SC absorbs excess power of 96W in short duration until battery can regulate the grid voltage to 48V. Thus, the battery and SC charge according to energy management scheme to maintain the grid voltage constant at 48V.

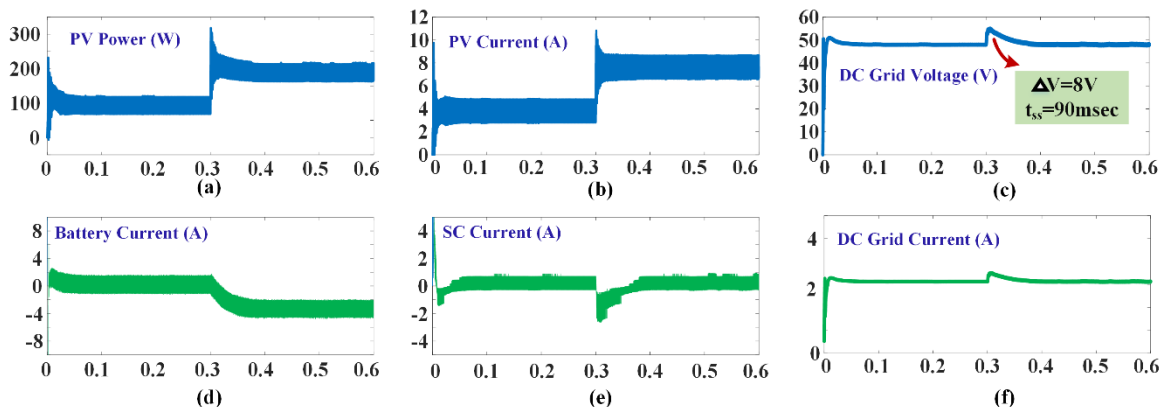


**Figure 3.16.** Simulation results for step increase in PV generation in Conventional control scheme

The simulation shows a settling time of 90ms for conventional control scheme and 35ms for proposed control scheme. The proposed control scheme has better dynamic performance and fast DC grid voltage regulation due to the utilization of uncompensated power from the battery system to improve the SC system.

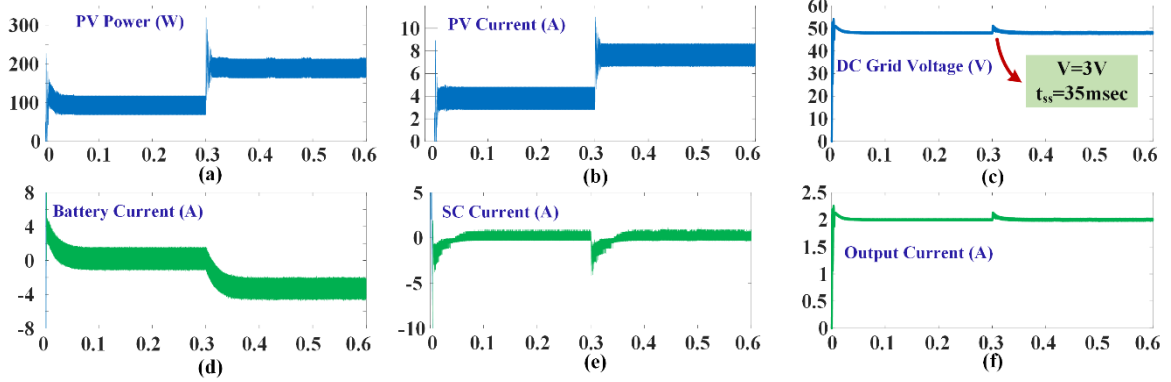


**Figure 3.17.** Simulation results for step increase in PV generation in Proposed control scheme

### 3.7.2 Case-II: Step decrease in PV generation

The simulation results for step decrease in PV generation for conventional and proposed schemes are presented in Figure 3.18 and Figure 3.19 respectively. In both the control schemes, due to atmospheric variations power produced by the PV panel changes from 192W to 96W at  $t= 0.3\text{sec}$ . The step decrease in PV generation causes step decrease in PV current from 8A to 4A. The sudden decrease in PV generation causes decrease in DC grid voltage.

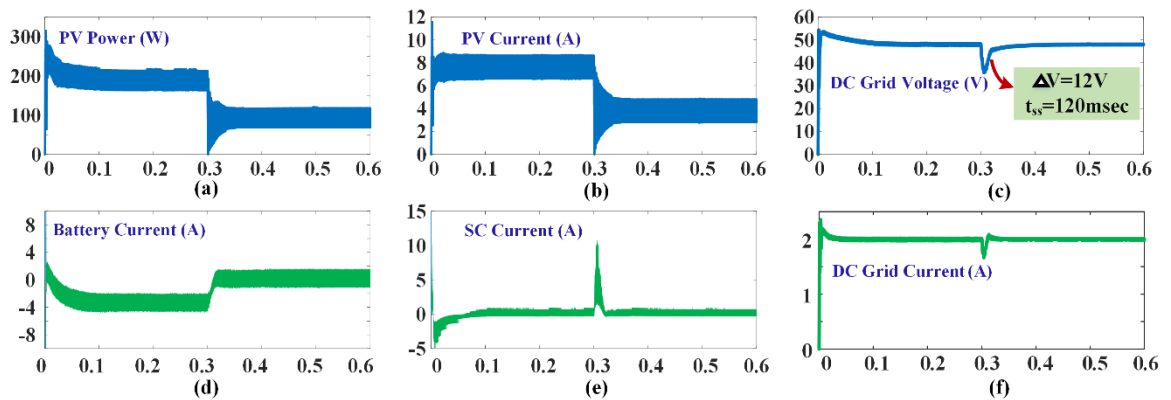


**Figure 3.18.** Simulation results for step decrease in PV generation in Conventional control scheme

The settling time for conventional and proposed schemes are 120msec and 30msec respectively. Proposed control scheme is approximately 4 times faster compared to

conventional control scheme. From the results, it can be observed that performance of proposed scheme is better compared to conventional control scheme.

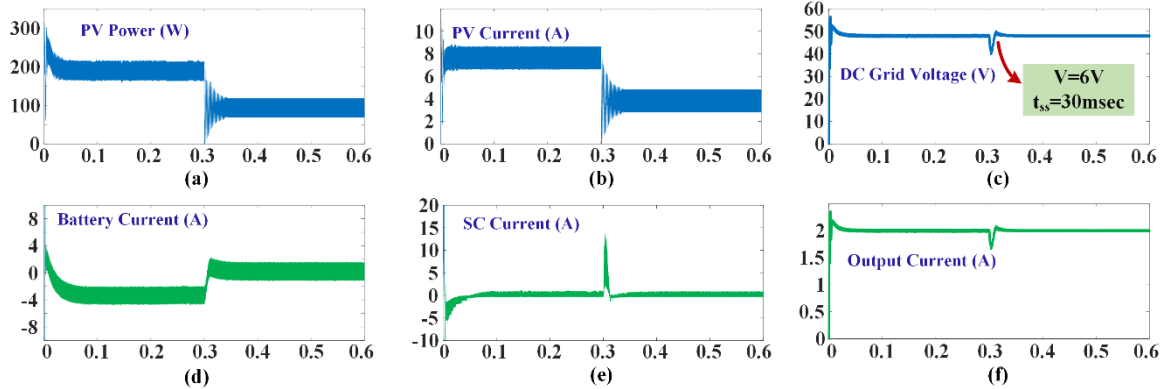


**Figure 3.19.** Simulation results for step decrease in PV generation in Proposed control scheme

### 3.7.3 Case-III: Step increase in load demand

Simulation results for step increase in load demand for conventional and proposed control schemes are presented in Figure 3.20 and Figure 3.21 respectively. At an instant  $t=0.3\text{sec}$  load demand increases from  $96\text{W}$  to  $192\text{W}$ . This increases the load current from  $2\text{A}$  to  $4\text{A}$ . During this case PV current is constant at  $4\text{A}$ . Before  $t=0.3\text{sec}$ , the steady state values of  $V_{DC}=48\text{V}$ ,  $i_{PV}=4\text{A}$ ,  $i_o=2\text{A}$ . At  $t=0.3\text{sec}$ , the load demand increases to  $192\text{W}$ , which is beyond the power range of PV generation. This creates a power imbalance between source power and load power. Immediately HESS responds, SC supply transient component of power demand and battery supplies steady state component of power demand. The DC grid voltage is regulated in  $150\text{msec}$  in conventional control scheme and  $25\text{msec}$  in proposed control scheme as shown in Figure 3.20 and Figure 3.21.

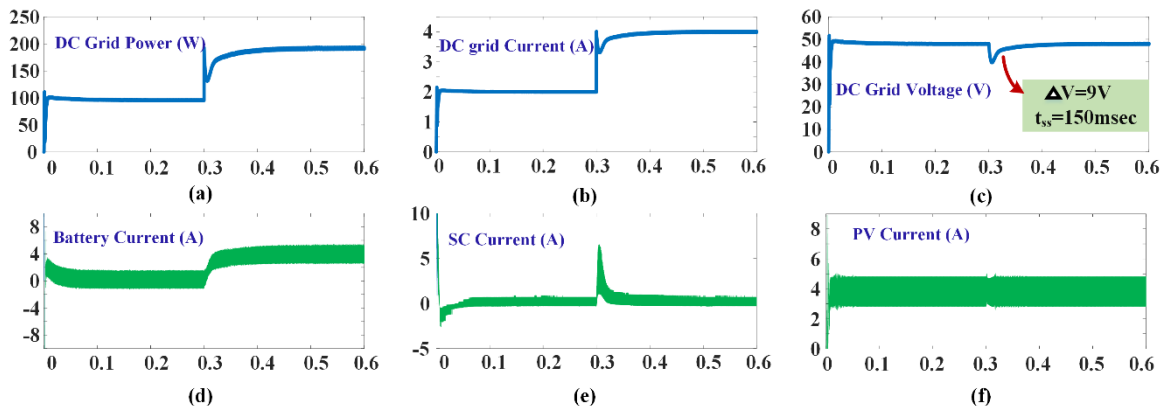


**Figure 3.20.** Simulation results for step increase in load demand in Conventional control scheme

**Table 3.1** Nominal parameters for simulation study

S. No	PARAMETERS	Value
1	MPPT Voltage ( $V_{\text{mppt}}$ )	24 V
2	MPPT Current ( $I_{\text{mppt}}$ )	4 A
3	MPPT Power ( $P_{\text{mppt}}$ )	96 W
3	SC Voltage ( $V_{\text{SC}}$ )	32 V
4	SC inductance ( $L_S$ )	0.355mH
5	Battery Voltage ( $V_B$ )	24 V
6	Battery inductance ( $L_B$ )	0.3mH
7	Boost inductance ( $L$ )	4.1mH
8	Resistance ( $R$ )	24 $\Omega$
9	DC grid voltage ( $V_{\text{DC}}$ )	48 V
10	Capacitance ( $C$ )	300 $\mu\text{F}$

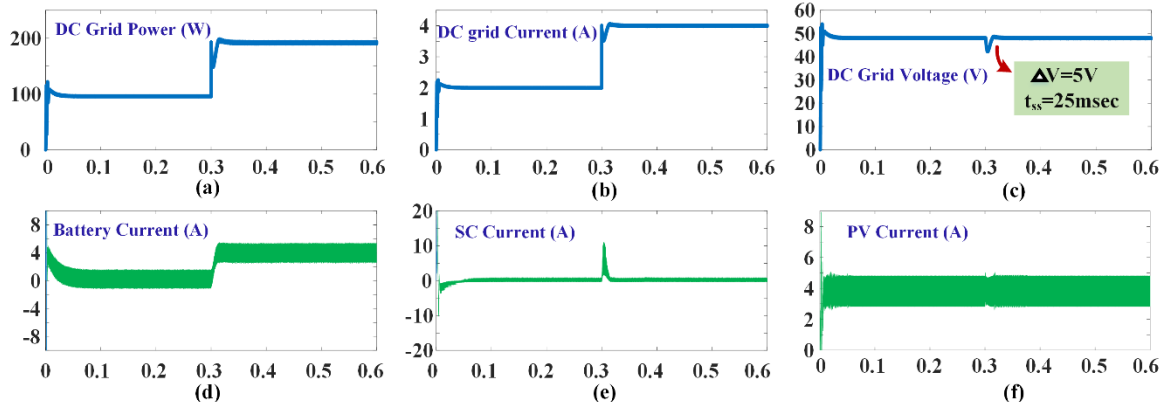


**Figure 3.21.** Simulation results for step increase load demand in proposed control scheme

### 3.7.4 Case-IV: Step decrease in load demand

The simulation results for step decrease in load demand for conventional and proposed control schemes are presented in Figure 3.22 and Figure 3.23 respectively. At  $t=0.3\text{sec}$ , load power demand decreases from 192W to 96W. This causes load current changes from 4A to 2A. The sudden change in load current affects the DC grid voltage. HESS responds immediately to these fluctuations to handle the excess power in the DC microgrid. The transient component of power handled is by the SC and average or steady state component of power is handled by the battery in both the control schemes. The times taken to restore the voltage, in conventional and proposed control scheme are 120msec and

40msec. From the results, it can be seen that the proposed control scheme is faster with less peak overshoot DC grid voltage compared to conventional control scheme.

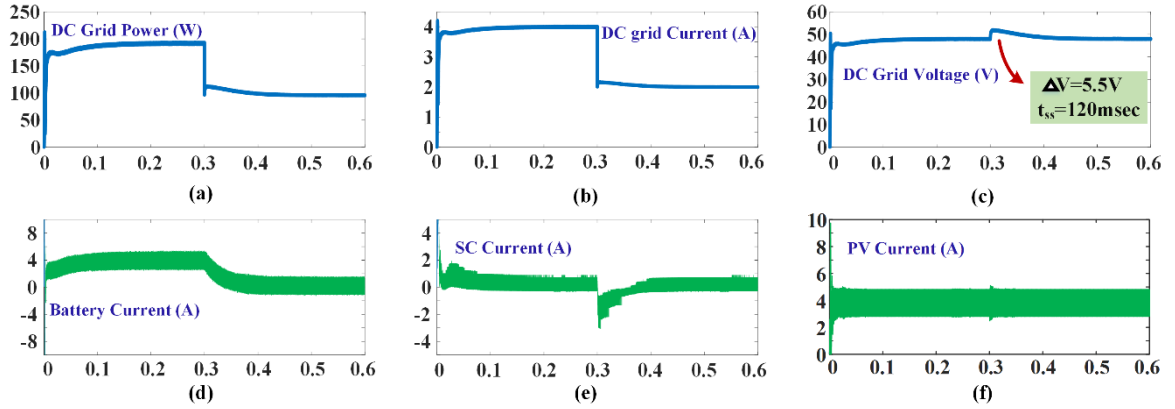


**Figure 3.22.** Simulation results for step decrease in load demand in Conventional control scheme

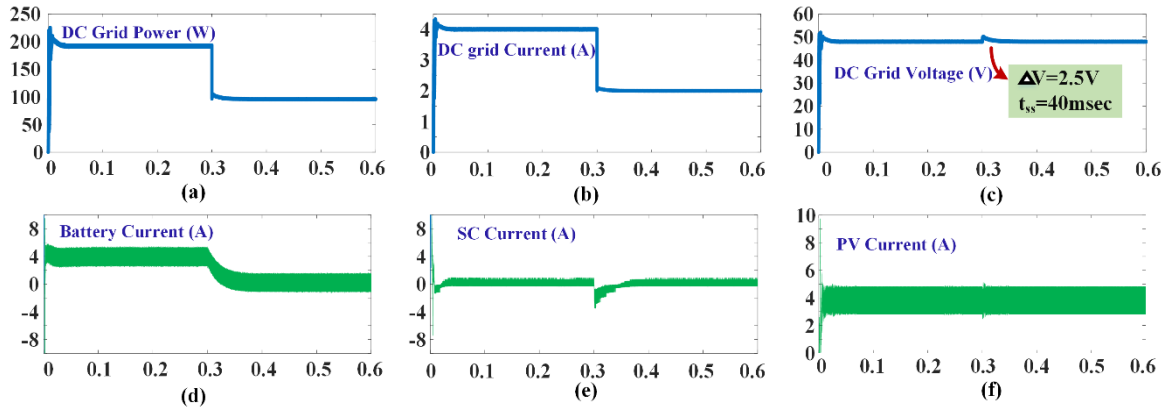


**Figure 3.23.** Simulation results for step decrease in load demand in Proposed control scheme

### 3.8 Comparative performance evaluation

The performance of the proposed control scheme is evaluated in comparison to the conventional control scheme with step change in PV generation as well as load demand for the peak overshoot and settling time to restore grid voltage. During step variation of PV generation and load demand, the maximum peak overshoot can be calculated as follows.

$$\%MP = \frac{|V_{DC,ref} - V_{max}|}{V_{DC,ref}} \times 100$$

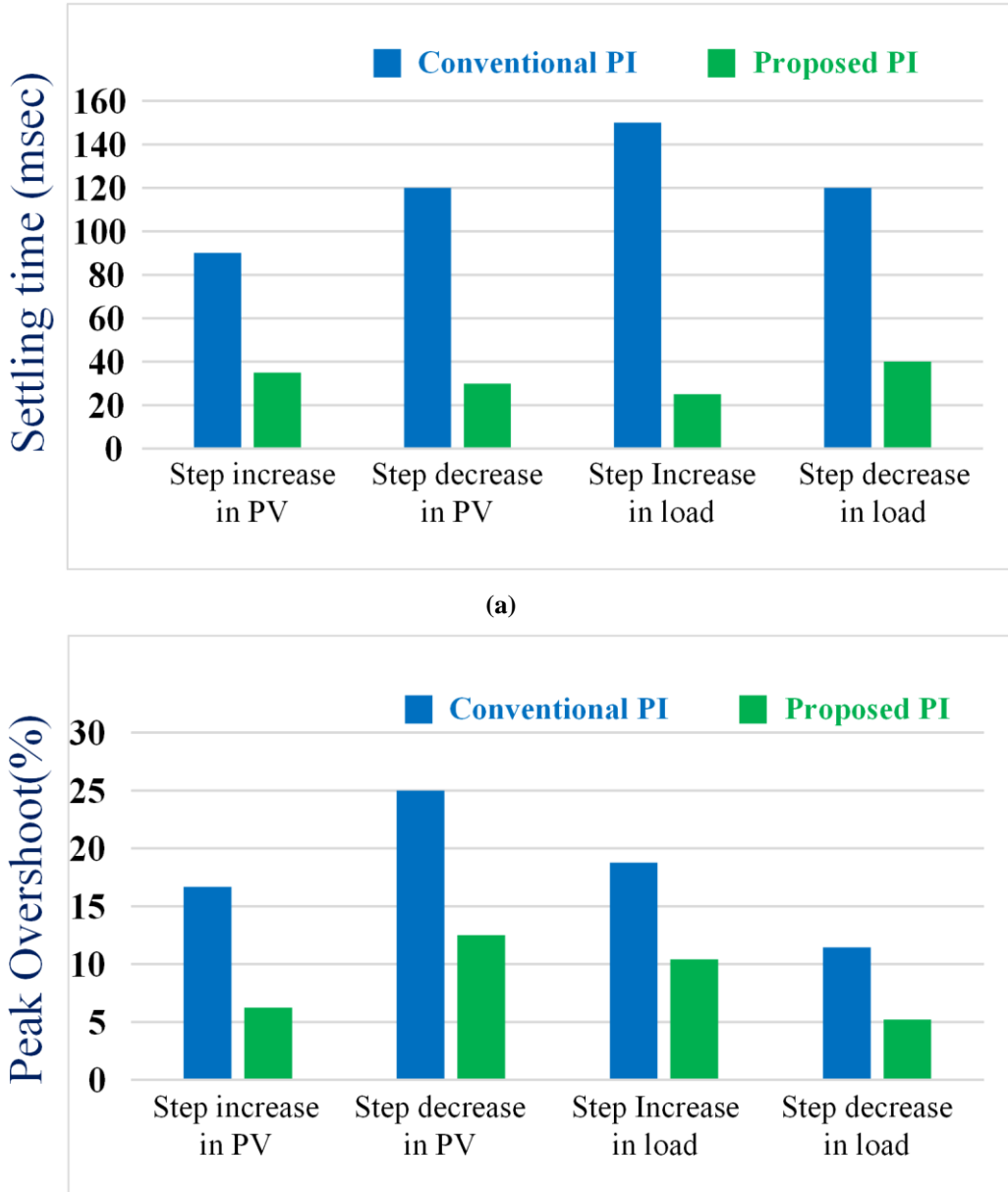


**Figure 3.24.** Graphical comparative performance of proposed and conventional control scheme. (a) Settling time (b) Peak overshoot

The comparative performance of conventional and proposed scheme is shown in Figure 3.24. It can be seen from the graphical representation that the proposed scheme is approximately three times faster compared to conventional scheme. In the proposed control scheme, the maximum peak overshoot is also reduced in all four cases. Proposed control scheme is designed such that SC supports the HESS up to the time the battery reaches steady state condition. The proposed scheme offers faster DC grid regulation with robust operation.

### 3.9 Experimental Results:

A low power hardware prototype is developed for proposed controller for two-input bidirectional converter shown in Figure 3.25. The controller used for this experiment is dSPACE DS1104. In this experiment a regulated power supply (RPS) is used as PV generator. RPS currents are controlled by using boost converter. HESS is wired up using Exide chloride 12V, 7Ah lead acid battery and Maxwell BMOD0058 16V, 58F supercapacitor. The two input bidirectional converter is built using Four MOSFET switches IRF540N. Operation of microgrid with HESS in charging/discharging mode explained in Section 3.4. DC grid specifications are given in Table 3.2. DC microgrid is setup at a nominal voltage of 20 V.

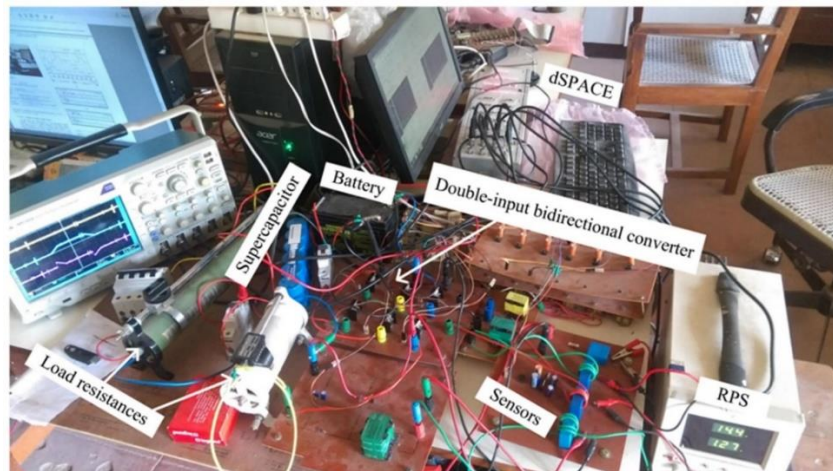


**Figure 3.25:** Prototype model of the proposed topology

**Table 3.2** System parameters for experimental study

S. No	Parameter	Value
1	MPPT Voltage ( $V_{pv}$ )	12V
2	MPPT Current( $i_{pv}$ )	1.4A
3	SC Voltage ( $V_s$ )	10 V
4	SC inductance ( $L_s$ )	1.43mH
5	Battery Voltage( $V_B$ )	12 V
6	Battery inductance ( $L_B$ )	4.8mH
7	Boost inductance ( $L_s$ )	4.1mH
8	Resistance ( $R$ )	$25 \Omega$
9	DC grid voltage( $V_{DC}$ )	20 V
10	Capacitance ( $C$ )	$150\mu F$

### 3.9.1 Case-I: HESS Charging mode:

Here controller designed for scenario of surge in DC grid voltage by increasing PV generation (or) decrease in load is analyzed. The waveforms are shown in Figure 3.26.

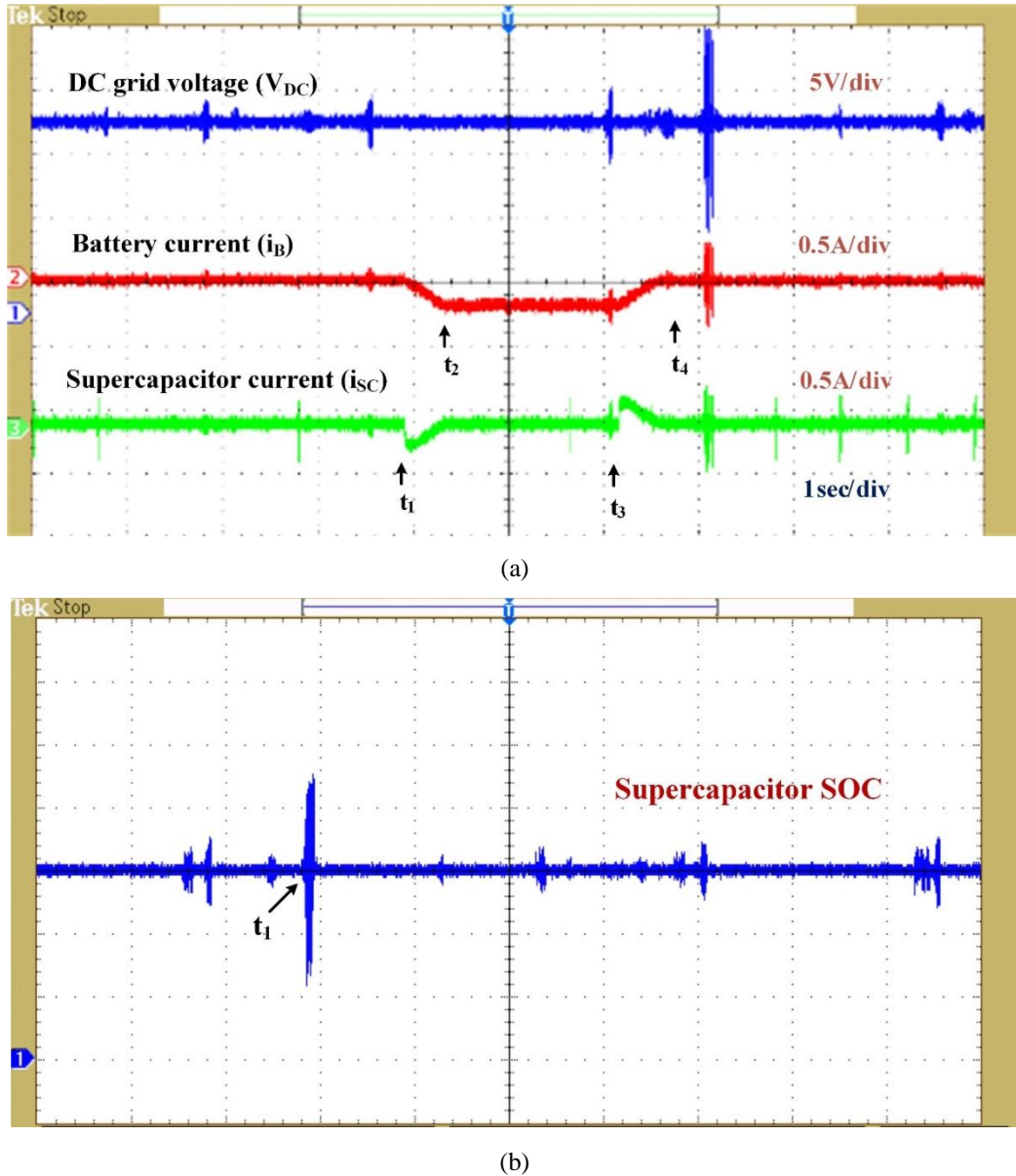


**Figure 3.26(a):** Experimental results for HESS charging mode: DC microgrid voltage ( $V_{DC}$ ), Battery current ( $i_B$ ), supercapacitor current ( $i_S$ ). (b) Supercapacitor SOC waveform

A sudden upward movement in microgrid voltage is realized by increasing PV generation. Initially  $I_{PV}=1.3A$  and at time  $t=t_1$ ,  $I_{PV}$  is increased to 1.42A and as a result increased in PV generation. The excess energy in DC grid cause a surge in grid voltage. Immediately HESS responds, Transient component of current charging supercapacitor and battery charging current is allowed to increase slowly till steady state value at instant  $t=t_2$ . The PV generation brought back to original condition of  $I_{PV}=1.3A$  at instant  $t=t_3$ . Battery and

supercapacitor then return to its floating state as it was before  $t=t_1$ . At instant  $t_1$  and  $t_3$  DC microgrid voltage is retained at 20V almost instantly as indicated by small spikes in the Figure.3.26. Supercapacitor SOC shown in Figure. 3.26(b). At the instant  $t_1$ ,  $SOC_{SC}$  is shown to be increasing indicating charging of supercapacitor. After transient current has died out, supercapacitor remains idle as indicated by constant SOC. Battery SOC is not considered, its energy not depleted fast compared to supercapacitor.

### 3.9.2 Case-II: HESS Discharging mode:

Discharging mode is active either due to decrease in PV generation or due to increase in load. Waveforms are shown in Figure.3.27.

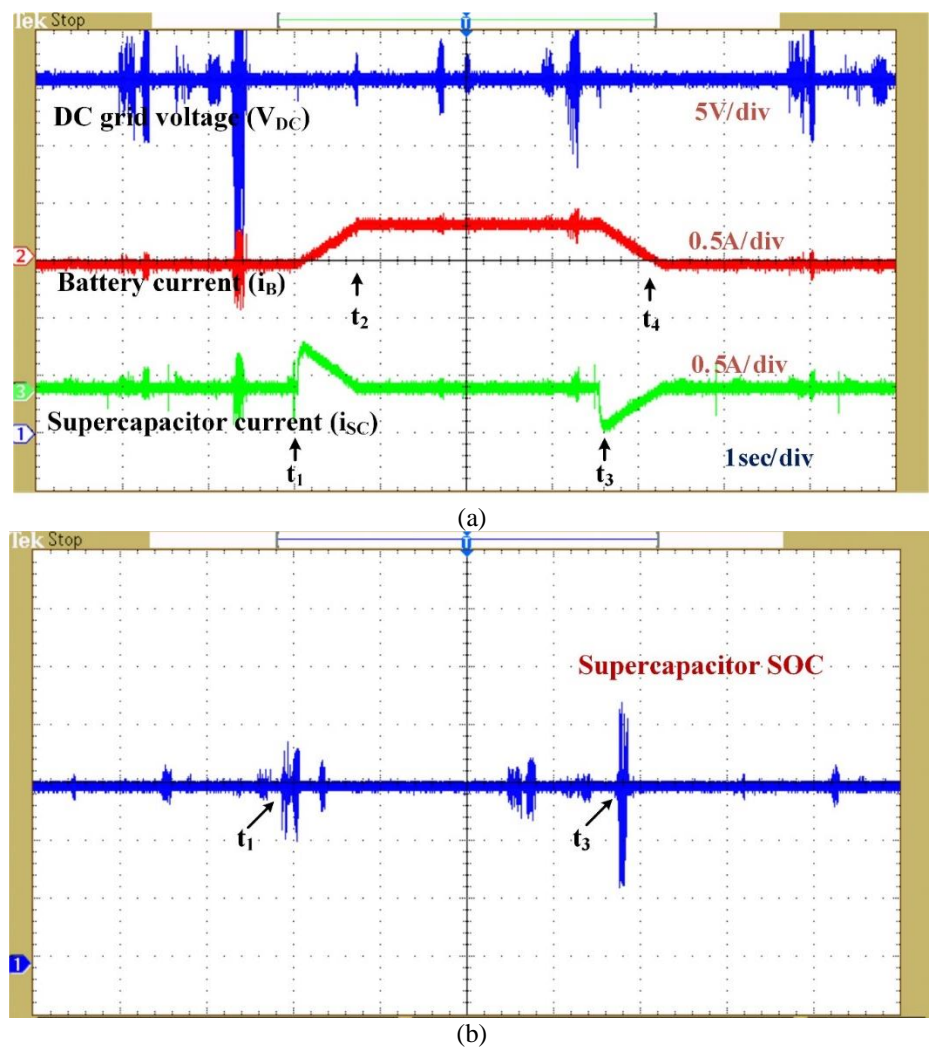


**Figure 3.27:** Experimental results for HESS discharging mode: DC microgrid voltage ( $V_{DC}$ ), Battery current ( $i_B$ ), supercapacitor current ( $i_S$ ) and state of charge of supercapacitor. (b) Supercapacitor SOC waveform

Here, dip in microgrid voltage is realized by an increase in load. At instant  $t_1$ ,  $R$  is decreased from  $25 \Omega$  to  $18 \Omega$ . This causes DC microgrid voltage to dip since there exists a

power mismatch between source and load. The deficient power is then fed by HESS by discharging battery and supercapacitor. Transient current is met by supercapacitor and steady state current is supplied by battery as is evident from current waveforms. Combined action of battery and supercapacitor maintain DC microgrid voltage constant at nominal value of 20 V. At instant  $t_3$ , Resistance is reverted back to normal setting of  $25 \Omega$  and  $V_{DC}$  is brought to 20 V again. Supercapacitor SOC waveform is also shown in Figure. 3.27(b) to validate the above explained operation. When load demand increased at instant  $t_1$ ,  $SOC_{SC}$  is found to be decreased as long as supercapacitor supplies current indicating discharge operation of supercapacitor. After that supercapacitor is idle as indicated by constant SOC waveform. Similarly at instant  $t_3$ , SOC increased to indicate charging of supercapacitor after which it stays idle.

### 3.10 Summary

In this chapter, a controller is designed for two input bi-directional converter with battery and supercapacitor as storage system. The detailed HESS modelling, design of bi-directional converter, controller design, stability analysis and simulation and experimental results are presented. The comparative performance evaluation of conventional with proposed control scheme have been illustrated.

The conventional control scheme is based on the idea that the battery supports steady-state power fluctuations while the SC supports transient power fluctuations. However, there was a current tracking error in the battery system. The error observed in the battery system is due to battery dynamics, battery controller dynamics and DC-DC converter that are not discussed in conventional control scheme. To address the issues raised above, a new control scheme is proposed that offers faster DC grid voltage management than the conventional control scheme. By utilizing the battery error current proposed control scheme overcome the slow dynamics of battery system. The main advantages of proposed control scheme are summarised as follows: (i) The proposed control scheme makes use of uncompensated power from the battery grid to increase overall system capacity. (ii) Less stress on battery during step change in PV generation and load demand. (iii) Proposed control scheme is faster DC grid voltage regulation with robust operation. The proposed method includes less CPU time. Hence it makes HESS with high power and energy density, which extended the life of battery.

# **Chapter-4**

## **Modelling of a Double-Input Bidirectional DC-DC Converter for HESS and Unified Controller Design for DC Microgrid Applications**

## Chapter-4

# Modelling of a Double-Input Bidirectional DC-DC Converter for HESS and Unified Controller Design for DC Microgrid Applications

### 4.1 Introduction

Due to easy integration with renewable energy sources as well as proliferation of dc-compatible loads, dc microgrids are gaining popularity [111] [112]. To exploit the advantages of both battery and supercapacitor, different topologies of HESS are shown in [51]. The most commonly used configuration of HESS, which has the leverage of attaining independent control on both battery and supercapacitor, is as shown in Figure 4.1(a). In this active parallel configuration of HESS, it is possible to exchange energy between the component ESSs, for example, the battery ESS can charge supercapacitor ESS or vice versa. However, the energy exchange process is through DC microgrid and this may push the grid operating limits beyond desired range.

Multiple input bidirectional (MIBD) converters, as in Figure 4.1 (b), have better energy exchange performance between input sources compared to multiple single-input bidirectional dc-dc (MSIBD) converters in active parallel configuration. This makes the former an excellent choice for applications like hybrid electric vehicle (HEV) and microgrids. The main advantage of MIBD converter over the MSIBD converter are (i) Better energy exchange between input sources (ii) reduces the system size (iii) reduces the cost of the converter [61]

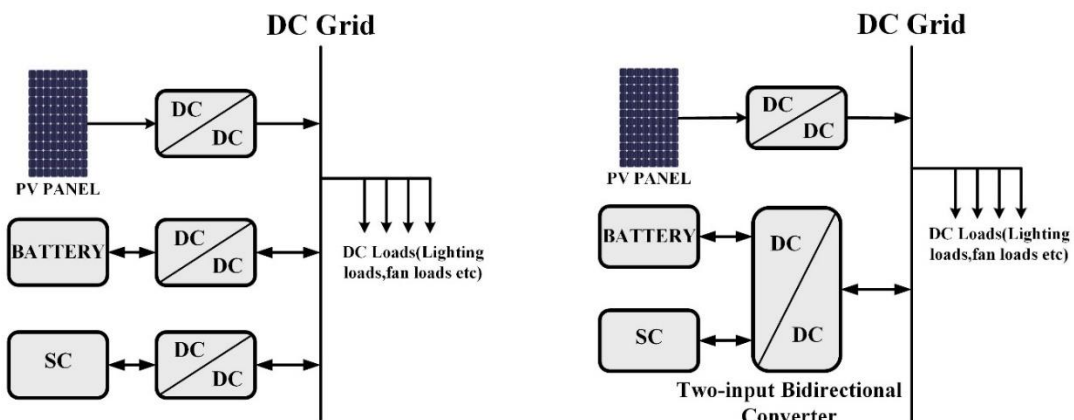


**Figure 4.1.** Different configurations of HESS, comprising of battery and SC, interfaced to dc microgrid. (a) Two separate bidirectional converter modules used. (b) Single double-input bidirectional converter

Several multiple input topologies have been proposed which can interface multiple sources with contrasting characteristics to a common load. Even though a large number of works about multi-input bidirectional converters are available in literature, less or little importance has been given to their controller development methods. A multi-input bidirectional dc-dc converter, proposed in [113], is used to interface the HESS to microgrid.

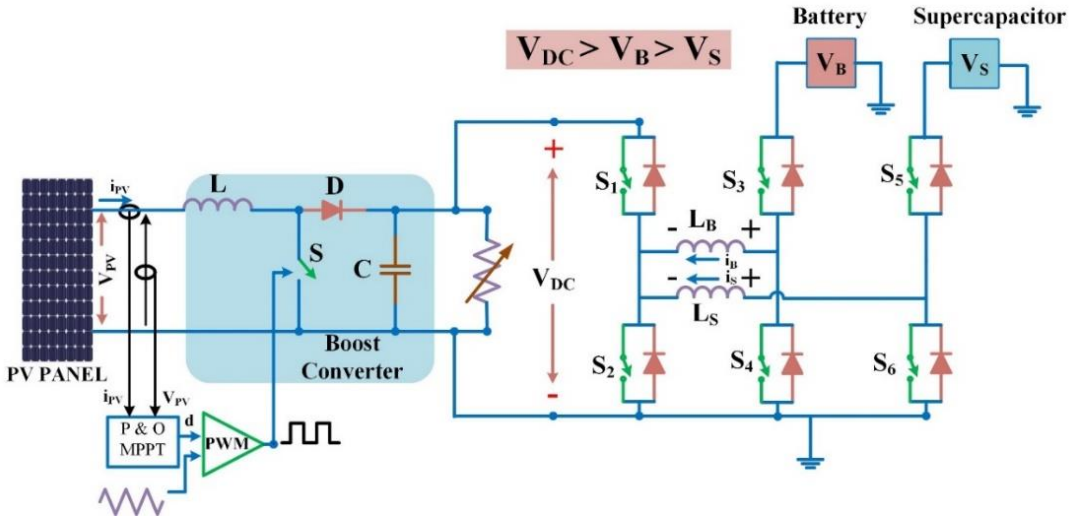


Figure 4.2. DC microgrid setup powered by PV source and supplemented by HESS

The converter in [113] has been modified in operation to suit for HESS operation in DC microgrid applications. One attractive attribute of this converter is that all the switches are turned on with zero voltage switching (ZVS) which can improve its efficiency. Apart from controlling the charging/discharging of HESS, the unified controller can also share current between battery and supercapacitor in such a way that the former is subjected to less current stress which helps in extending its lifetime. Total HESS current (charging/discharging) bifurcates such that high frequency component of the current is being supplied by power density element supercapacitor and average or low frequency current is being fed by energy density unit battery. The main contributions of the paper are as follows.

1. A multi input converter based DC microgrid voltage stabilization is proposed in this Chapter.
2. Detailed controller design and analysis is presented for HESS based MIBD. The presented small signal model based controller for multi input converter can ensure stability in all operating regions.

3. Implementation of energy management system for MIBD with HESS is presented for different PV and load conditions. The EMS can easily track the SC SOC and enable different mode to ensure safe operation.
4. The main advantage of designed double-input Bidirectional converter is its energy exchange mode where we can charge the SC independently from battery. Aside from that, the bi-directional double-input converter has some benefits such as efficient power allocation between the various ESSs, faster DC link voltage control to the PV power fluctuations and load disturbances.
5. The proposed modified operation of converter made it possible to use same controller for both HESS charging/discharging operation thus making it a unified controller.

The DC microgrid setup by PV source supported by battery-supercapacitor HESS is shown in Figure 4.2.

## 4.2 Two Input Bidirectional DC-DC Converter operation

The two input bidirectional converter is shown in Figure 4.3. Various modes of operation are elaborated in detail in [113]. Modified operation of the converter is explained here. It consists of three switch-legs. Battery ( $V_B$ ) and supercapacitor ( $V_S$ ) modules are connected to legs 2 and 3 respectively. DC microgrid ( $V_{DC}$ ) is connected to leg 1. Battery voltage is selected to be less than that of DC grid voltage but greater than supercapacitor voltage in this converter topology. High frequency inductors  $L_B$  and  $L_S$  are connected between legs 1, 2 and 1, 3 respectively. Different modes of operation are explained in following sections.

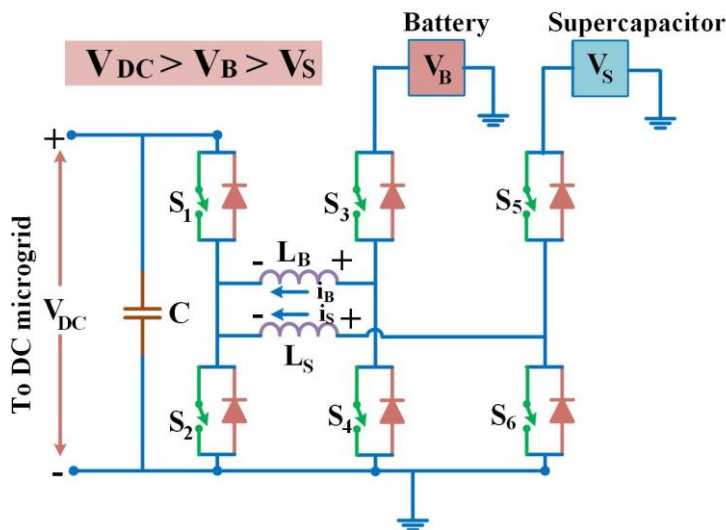
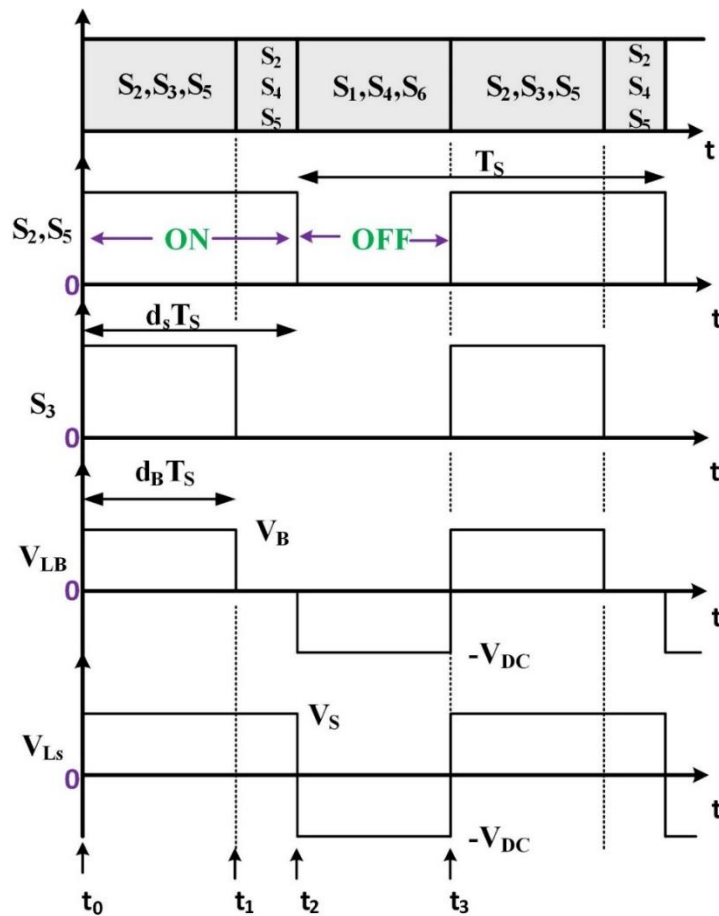


Figure 4.3. Two-input bidirectional converter topology for HESS [113].

#### 4.2.1 HESS discharging mode

Whenever there exists a mismatch between PV output and load power, DC microgrid voltage varies from steady state value. DC microgrid voltage decreases if load exceeds PV generation capability or when PV generated power falls due to reduced solar irradiation. During this time deficient power has to be supplied by HESS. So power flows from HESS to DC microgrid in this mode, by properly controlling the bidirectional converter.



**Figure 4.4.** Steady-state waveforms for HESS discharging mode of operation

The converter operation in this mode can be divided into three time intervals as in Figure 4.4. Switch pairs  $S_1/S_2$ ,  $S_3/S_4$  and  $S_5/S_6$  always work in complimentary fashion. Switch pair  $S_2/S_5$  and  $S_1/S_6$  always switch together in this mode and their gating pulses are complimentary to each other. At time instant  $t_0$ , switches  $S_2$ ,  $S_3$  and  $S_5$  are turned on which will increase inductor currents  $i_B$  and  $i_S$  linearly with slopes  $V_B/L_B$  and  $V_S/L_S$  respectively. At  $t_1$ , switch  $S_3$  is turned off to provide a free-wheeling path for current  $i_B$  through body diode of  $S_4$ . After dead time interval for switch pair  $S_3/S_4$ , switch  $S_4$  is turned on. Since body

diode of  $S_4$  is already conducting when gating signal was given,  $S_4$  turns on with ZVS. At  $t_2$ , switches  $S_2$  and  $S_5$  are turned off causing inductor current  $i_{L2}$  to flow through body diodes of switches  $S_1$  and  $S_6$  with a negative slope of  $V_{DC}/L_S$ . Inductor current  $i_B$  also flows body diode of  $S_1$  with a negative slope of  $V_{DC}/L_B$ . Switches  $S_1$  and  $S_6$  are gated on after dead time interval of switch pairs  $S_2/S_1$  and  $S_5/S_6$ . Similar to the turn on of  $S_4$ , switches  $S_1$  and  $S_6$  are also turned on with ZVS since body diodes of respective switches are already in conduction. At  $t_3$ , switches  $S_1$ ,  $S_4$  and  $S_6$  are turned off. Consequently, body diodes of switches  $S_2$ ,  $S_3$  and  $S_5$  will conduct in order to maintain the flow of inductor currents. Currents,  $i_B$  and  $i_S$ , flow with positive slopes of  $V_B/L_B$ , and  $V_S/L_S$  respectively. After dead time interval, gating pulses are given to switches  $S_2$ ,  $S_3$  and  $S_5$  which turn on with ZVS. If  $d_B$  is duty cycle of gating pulse given to switch  $S_3$  and  $d_S$  is duty cycle of gating pulse given to switches  $S_2$  and  $S_5$ , applying volt-second balance to inductors  $L_S$  and  $L_B$  gives

$$V_{DC} = \frac{d_S}{1-d_S} \cdot V_S \quad (4.1)$$

$$V_{DC} = \frac{d_B}{1-d_S} \cdot V_B \quad (4.2)$$

Since  $V_B$  is greater than  $V_S$ ,  $d_B$  will always be lesser than  $d_S$ . Therefore, by controlling  $d_B$  and  $d_S$ , power flow from battery and supercapacitor to dc grid can be controlled independently.

#### 4.2.2 HESS charging mode

Whenever PV generated power exceeds that required by load or when load decreases, there is excess power existing in the DC microgrid which results in increase of DC microgrid voltage. This excess power will charge battery and supercapacitor. Hence, in this mode power flows from DC microgrid to HESS. The converter operation in this mode can be divided into three time intervals as in Figure. 4.5. Switch pair  $S_1$  and  $S_6$  are switched simultaneously. Switch pair  $S_2$  and  $S_5$  are also gated simultaneously but with complimentary pulses to that of  $S_1$  and  $S_6$ . Similarly switches  $S_4$  and  $S_3$  are also gated in complimentary fashion. At  $t_0$ , switches  $S_1$ ,  $S_4$  and  $S_6$  are gated on to increase the inductor currents,  $i_B$  and  $i_S$ , in negative direction linearly with slopes  $V_{DC}/L_B$  and  $V_{DC}/L_S$  respectively.

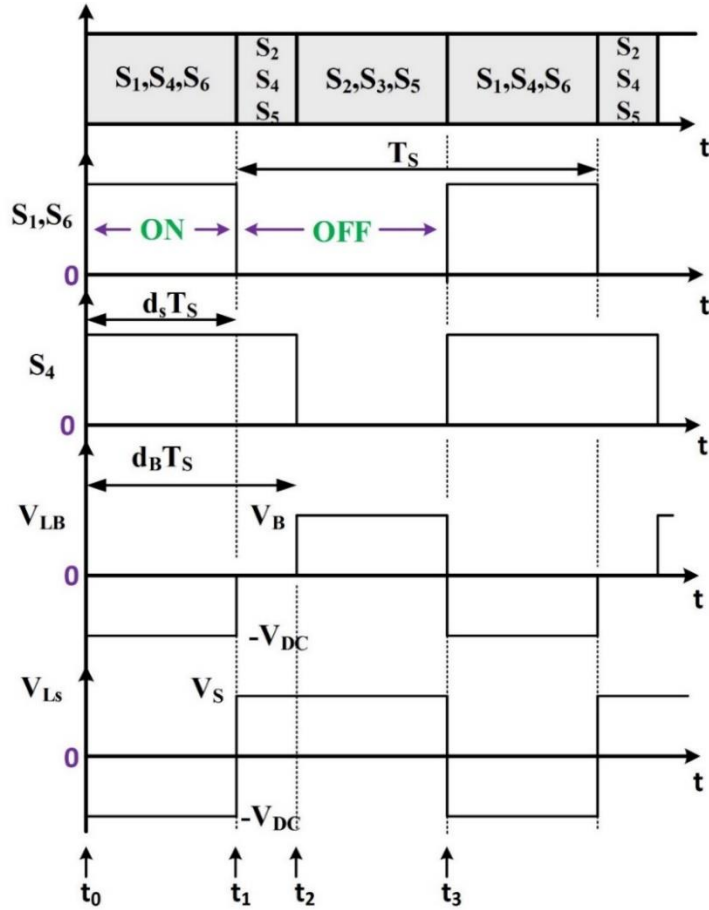


**Figure 4.5.** Steady-state waveforms for HESS charging mode of operation

Inductors,  $L_B$  and  $L_S$ , store energy in this time interval until instant  $t_1$ . At  $t_1$ , switch pair  $S_1/S_6$  are turned off. In order to maintain inductor current  $i_S$ , body diodes of switches  $S_2$  and  $S_5$  turn on. Energy stored in inductor  $L_S$  is now used up to charge supercapacitor. Inductor current  $i_B$  free-wheels through body diode of switch  $S_2$ . After dead time interval for switch pair  $S_1/S_6$  and  $S_2/S_5$ , gating pulses are given to  $S_2$  and  $S_5$  which turns them on with ZVS since body diodes of respective switches are already in conduction. At time instant  $t_2$ , switch  $S_4$  is turned off. Inductor current  $i_S$  increase linearly with slope  $V_S/L_S$  through body diode of switch  $S_3$ . After dead time interval of switch pair  $S_4/S_3$ , gating pulse to  $S_3$  is applied to turn it on with ZVS. Energy stored in inductor  $L_B$  is now used to charge battery. At instant  $t_3$ , switches  $S_2$ ,  $S_3$  and  $S_5$  are tuned off, consequently body diodes of switches  $S_1$ ,  $S_4$  and  $S_6$  turns on to maintain flow of inductor currents. Gating pulses are given to  $S_1$ ,  $S_4$  and  $S_6$  after dead time interval to turn them on with ZVS. If  $d_S$  is duty cycle of gating pulse to  $S_1/S_6$  switch pair and  $d_B$  is duty cycle of gating pulse to switch  $S_4$ , applying volt-second balance to inductors  $L_S$  and  $L_B$  gives

$$V_s = \frac{d_s}{1-d_s} \cdot V_{DC} \quad (4.3)$$

$$V_B = \frac{d_s}{1-d_B} \cdot V_{DC} \quad (4.4)$$

Since  $V_B$  is greater than  $V_s$  which in turn is smaller than  $V_{DC}$ ,  $d_B$  is always greater than  $d_s$ . By controlling  $d_B$  and  $d_s$ , power flow from DC microgrid to HESS can be controlled.

#### 4.2.3 HESS Energy exchange mode

Supercapacitor in HESS is a power density unit. It cannot supply energy for long duration continuously like battery due to its high self-discharging effect. For proper functioning of HESS in DC microgrid applications it is necessary that component ESSs of HESS should have enough energy stored in it. To maintain supercapacitor charge within desired limits, it has to be charged whenever needed from the energy density unit battery for proper functioning of HESS. This mode constitutes power flow from battery to supercapacitor. Circuit topology in this mode is given in Figure 4.6(a).

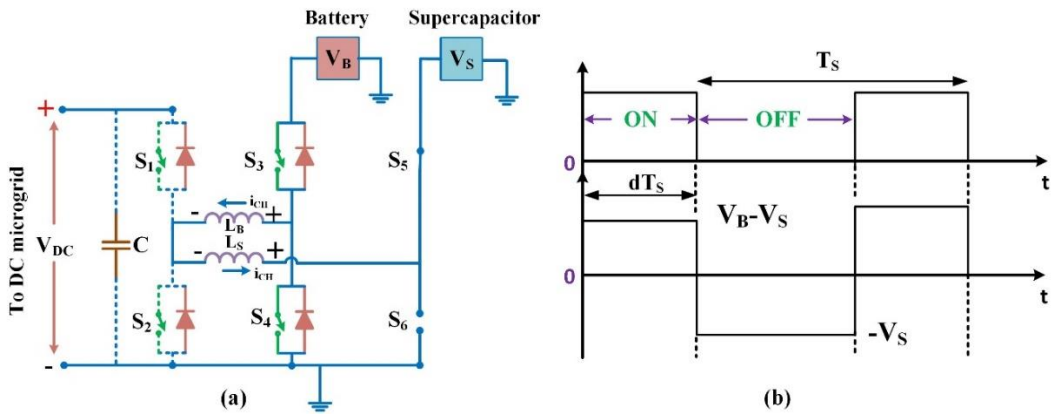


**Figure 4.6.** HESS Energy Exchange mode of operation. (a) Active circuit through which current flows. (b) Steady-state waveforms

In this mode, first switch leg is inactive (switches  $S_1$  and  $S_2$  are off) thus effectively isolating the DC microgrid from HESS during supercapacitor charging process. Switch pairs  $S_5/S_6$  and  $S_3/S_4$  work in complimentary manner. Switch  $S_5$  is always on in this mode which cause switch  $S_6$  to be always off. Switch  $S_3$  is operated upon with duty cycle  $d$ . Waveforms are as shown in Figure 4.6(b). Power flow from battery to supercapacitor involves buck operation of switch  $S_3$ . Inductors,  $L_B$  and  $L_s$ , are in series and this considerably reduce the current ripple. By controlling  $d$ , power flow from battery to supercapacitor can be controlled. Applying volt-second balance to equivalent series inductor  $L$  ( $L = L_B + L_s$ ) gives

$$V_s = d \cdot V_B \quad (4.5)$$

Similarly, power flow from supercapacitor to battery is possible by complimentary operation of switch  $S_3$ . This indicates boost operation of switch  $S_4$ . Operation is similar to that explained above.

#### 4.2.4 Mode Transitions

The mode of operation is determined from present condition of DC microgrid and continuous monitoring of supercapacitor SOC. Battery SOC is not considered in this work since it is assumed that battery energy is not depleted fast compared to supercapacitor. Flow chart for simple mode transition logic is shown in Figure 4.7. When DC microgrid voltage exceeds the set reference, HESS is put into charging mode, provided supercapacitor SOC is within prescribed limits. When DC microgrid voltage is less than set reference value, HESS is put into discharging mode, provided supercapacitor SOC is in safe limits. If supercapacitor SOC violates the prescribed limits, HESS is put into energy exchange mode, thus isolating the DC microgrid electrically from HESS. Supercapacitor SOC working range and its mathematical expression using coulomb's counting method are

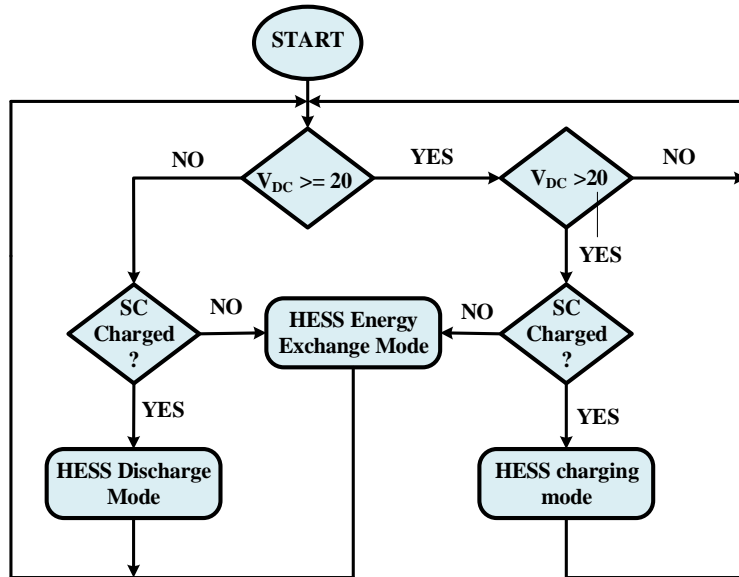


**Figure 4.7.** Transitions to different modes represented using a flow chart.

$$SOC_{MIN} \leq SOC \leq SOC_{MAX} \quad (4.6)$$

$$\% SOC = \left[ SOC_i + \left( \frac{1}{Q_{SC}} \int i_{CH} dt \right) \right] \times 100 \quad (4.7)$$

where  $SOC_i$  is initial SOC of supercapacitor,  $Q_{SC}$  is rated supercapacitor charge and  $i_{CH}$  is supercapacitor charging current.

### 4.3 Small Signal Linear Averaged Model of 2-Input Bidirectional Converter and Controller Design

Small signal averaged model is the basis for development of unified controller for charging/discharging of HESS. An effective model will contribute a controller which will not only provide good closed loop performance but also provide stable operation amidst converter dynamics and external disturbances.

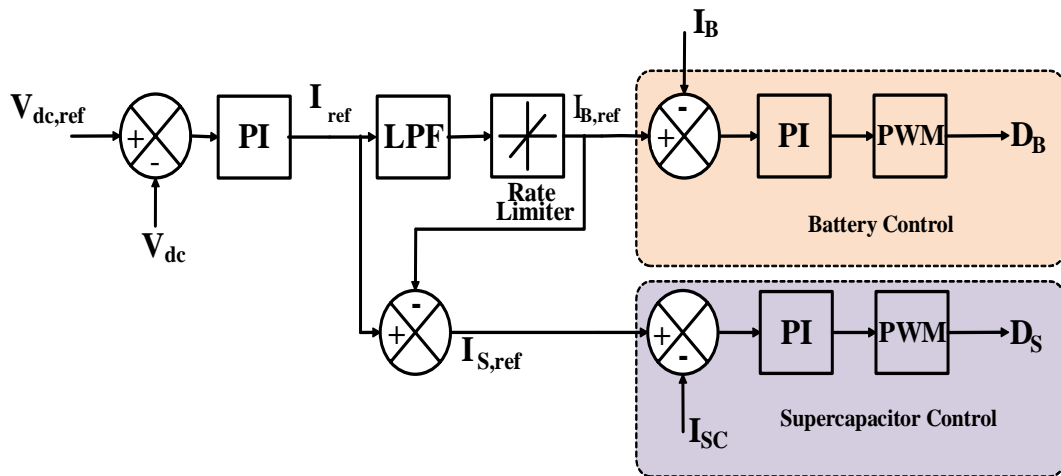


**Figure 4.8.** Overall control system description for current bifurcation between SC and battery units.

As per circuit operation as explained in previous sections, independent control of power flow is possible from battery and supercapacitor to DC microgrid. Hence, decoupled small signal model can be developed for battery stage as well as for supercapacitor stage which is similar to developing dynamic model of two single-input bidirectional converter. This decoupled averaged small signal model of battery and supercapacitor power flow stage aids in designing simpler controllers which otherwise would be complicated due to presence of multi-input multi-output control systems [73]. Small signal model of battery to DC microgrid as well as supercapacitor to DC microgrid are developed as follows.

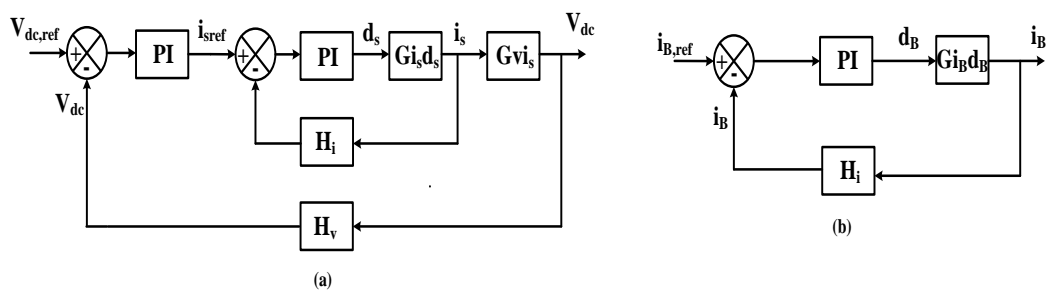


**Figure 4.9.** Supercapacitor and battery control logic. (a) Control system description for supercapacitor control. (b) Control system description for battery control

A unified controller for battery/supercapacitor charging/discharging will suffice since both the circuit operations share same small signal transfer function due to complimentary action of switches. For developing linear models, HESS discharging mode of operation is considered. Control system description for bifurcation of battery and supercapacitor power is shown in Figure 4.8. The outer voltage loop is designed based on supercapacitor stage because of its inherent fast dynamic response.

Thus control system description of supercapacitor stage consists of an inner current loop and an outer voltage loop as depicted in Figure 4.9(a). Similarly, battery current reference is regulated by a current controller as in Figure 4.9(b). Inner current loop of supercapacitor is designed for a higher bandwidth than that of battery for fast response. Inner current loop operate at a faster rate compared to that of outer voltage loop. Hence voltage loop bandwidth is maintained lesser than inner current loop. Switching frequency considered is 10 kHz.

#### 4.3.1 Small Signal Linear Averaged Model of SC-DC Microgrid Stage

From Figure 4.4 and as per operation explained in Section 4.2, during time interval ( $t_0 \sim t_2$ ) the state equations are as follows.

$$\begin{aligned} L_s \frac{di_{L_s}}{dt} &= v_{sc} \\ C \frac{dv_{DC}}{dt} &= -\frac{v_{DC}}{R} \end{aligned} \quad (4.8)$$

During time interval ( $t_2 \sim t_3$ ), the state equations are as follows.

$$\begin{aligned} L_s \frac{di_{L_s}}{dt} &= -v_{DC} \\ C \frac{dv_{DC}}{dt} &= i_{L_s} - \frac{v_{DC}}{R} \end{aligned} \quad (4.9)$$

After perturbation and linearization of above state equations, control-to-inductor current and inductor current-to-voltage small signal transfer functions are obtained as follows.

$$\begin{aligned}
G_{i_{sc}d_{sc}} &= \frac{i_{sc}(s)}{d_{sc}(s)} \\
&= \frac{V_{DC}(1+D_{sc})}{R(1-D_{sc})^3} \left[ \frac{1+s \frac{RC}{1+D_{sc}}}{s^2 \frac{L_{sc}C}{(1-D_{sc})^2} + s \frac{L_{sc}}{R(1-D_{sc})^2} + 1} \right] \\
G_{v_{DC}i_{sc}} &= \frac{v_{DC}(s)}{i_{sc}(s)} = \frac{R(1-D_{sc})}{(1+D_{sc})} \left[ \frac{1-s \frac{D_{sc}L_{sc}}{R(1-D_{sc})^2}}{1+s \frac{RC}{1+D_{sc}}} \right]
\end{aligned} \tag{4. 10}$$

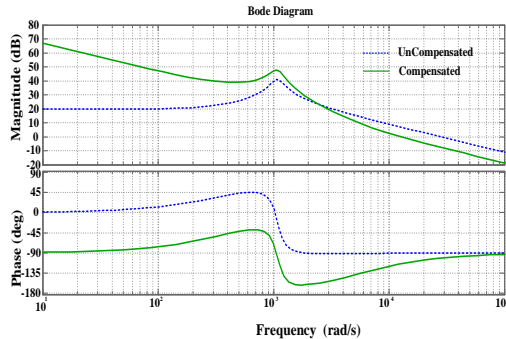


**Figure 4.10.** Bode plot of inner current controller Of SC Control logic, with and without controller

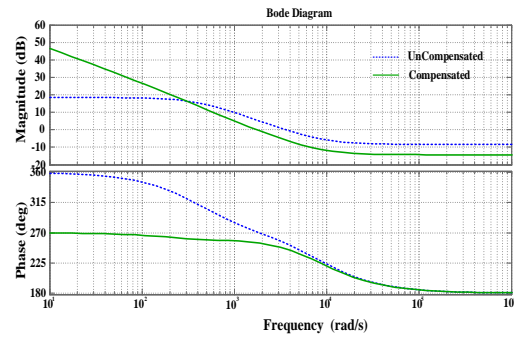


**Figure 4.11.** Bode plot of outer voltage controller of SC control logic, with and without controller

PI controller for inner current loop is designed based on above model with bandwidth of 1.6 kHz and phase margin of 60°. Bode plot for compensated and uncompensated transfer functions is shown in Figure 4.10. The transfer function is given by

$$G_{pi\_i_s} = 0.4124 + \frac{2291}{s} \tag{4.11}$$

PI controller for outer voltage loop is also designed based on the averaged model. Bandwidth has to be less than right half plane zero. The designed voltage controller has a bandwidth of 200 Hz and phase margin of 60°. Bode plot for the same is as shown in Figure 4.11. The transfer function is given by

$$G_{pi\_v} = 0.5054 + \frac{266}{s} \tag{4.12}$$

### 4.3.2. Small Signal Linear Averaged Model of Battery-DC Microgrid Stage

Discharge operation of battery is completed in three time intervals as shown in Figure 4.4. As explained in Section 4.2, during time interval (t<sub>0</sub>~t<sub>1</sub>), the state equations are as follows.

$$\begin{aligned}
L_B \frac{di_B}{dt} &= v_B \\
C \frac{dv_{DC}}{dt} &= -\frac{v_{DC}}{R}
\end{aligned} \tag{4.13}$$

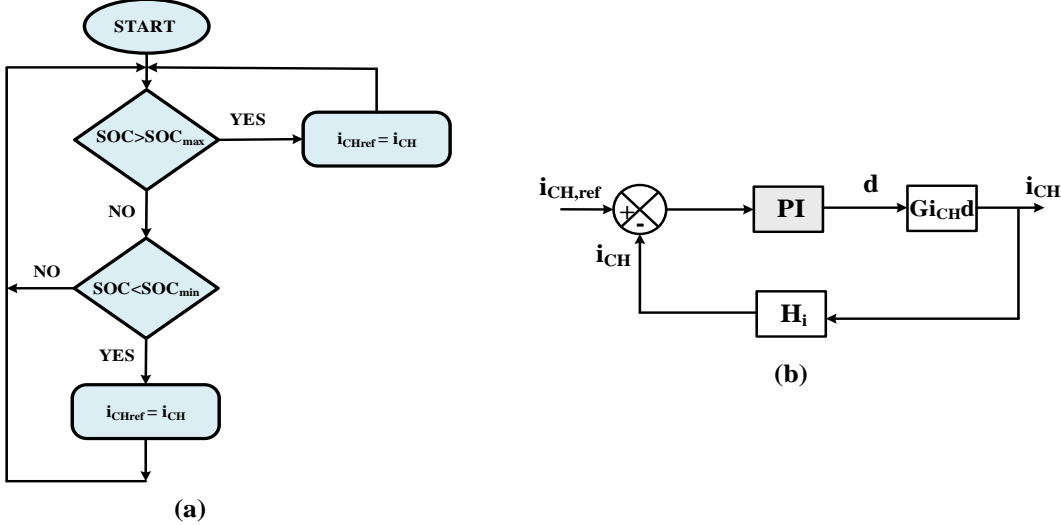


**Figure 4.12.** SOC charge controller for supercapacitor. (a) Logic to select between charging/discharging. (b) Control logic diagram

The above system of state equations can be represented in matrix form after converting to frequency domain which takes the following form

$$\begin{aligned}
\frac{dX}{dt} &= AX + BU \\
Y &= CX + EU
\end{aligned} \tag{4.14}$$

Where X is a matrix containing all state variables (i<sub>B</sub>, v<sub>DC</sub>), U is a matrix containing inputs and Y is a matrix containing all the system outputs. Equation (4.13) can be rewritten in matrix form as

$$\begin{aligned}
\begin{bmatrix} \frac{di_B}{dt} \\ \frac{dv_{DC}}{dt} \end{bmatrix} &= [A_1] \begin{bmatrix} i_B \\ v_{DC} \end{bmatrix} + [B_1] \begin{bmatrix} v_{DC} \end{bmatrix} \\
\begin{bmatrix} i_B \\ v_{DC} \end{bmatrix} &= [C_1] \begin{bmatrix} i_B \\ v_{DC} \end{bmatrix} + [E_1] \begin{bmatrix} v_{DC} \end{bmatrix}
\end{aligned} \tag{4.15}$$

$$\text{Where } A_1 = \begin{bmatrix} 0 & 0 \\ 0 & -\frac{1}{RC} \end{bmatrix}, B_1 = \begin{bmatrix} 1 \\ \frac{1}{L_B} \end{bmatrix}, C_1 = \begin{bmatrix} 1 & 0 \end{bmatrix} \text{ and } E_1 = \begin{bmatrix} 0 \end{bmatrix}.$$

Similarly, for second time interval (t<sub>1</sub>~t<sub>2</sub>), the state equations and its matrix form can be represented as follows.

$$\begin{aligned} L_B \frac{di_B}{dt} &= 0 \\ C \frac{dv_{DC}}{dt} &= -\frac{v_{DC}}{R} \end{aligned} \quad (4.16)$$

$$\begin{bmatrix} \frac{di_B}{dt} \\ \frac{dv_{DC}}{dt} \end{bmatrix} = [A_2] \begin{bmatrix} i_B \\ v_{DC} \end{bmatrix} + [B_2] \begin{bmatrix} v_{DC} \end{bmatrix}$$

$$[i_B] = [C_2] \begin{bmatrix} i_B \\ v_{DC} \end{bmatrix} + [E_2] \begin{bmatrix} v_{DC} \end{bmatrix}$$

(4.17)

$$\text{Where } A_2 = \begin{bmatrix} 0 & 0 \\ 0 & -\frac{1}{RC} \end{bmatrix}, B_2 = \begin{bmatrix} 0 \\ 0 \end{bmatrix}, C_2 = \begin{bmatrix} 1 & 0 \end{bmatrix} \text{ and } E_2 = \begin{bmatrix} 0 \end{bmatrix}.$$

In third time interval ( $t_2 \sim t_3$ ), the state equations and state model in matrix form are expressed as follows.

$$\begin{aligned} L_B \frac{di_B}{dt} &= -v_{DC} \\ C \frac{dv_{DC}}{dt} &= i_B - \frac{v_{DC}}{R} \end{aligned} \quad (4.18)$$

$$\begin{bmatrix} \frac{di_B}{dt} \\ \frac{dv_{DC}}{dt} \end{bmatrix} = [A_3] \begin{bmatrix} i_B \\ v_{DC} \end{bmatrix} + [B_3] \begin{bmatrix} v_{DC} \end{bmatrix}$$

$$[i_B] = [C_3] \begin{bmatrix} i_B \\ v_{DC} \end{bmatrix} + [E_3] \begin{bmatrix} v_{DC} \end{bmatrix}$$

$$\text{Where } A_3 = \begin{bmatrix} 0 & -\frac{1}{L_B} \\ \frac{1}{C} & -\frac{1}{RC} \end{bmatrix}, B_3 = \begin{bmatrix} 0 \\ 0 \end{bmatrix}, C_3 = \begin{bmatrix} 1 & 0 \end{bmatrix} \text{ and } E_3 = \begin{bmatrix} 0 \end{bmatrix}.$$

From Figure 4.4 it is evident that the bidirectional converter will be subjected to state model represented by (4.15) for a time duration of  $(d_B \cdot T_S)$  after which it will undergo transition to the model represented by (4.17) where it stays for a duration of  $[(d_S - d_B) \cdot T_S]$ . The duration of third time interval is  $[(1 - d_S) \cdot T_S]$  for which the model is (4.19). Thus, averaged state model of the converter is obtained as follows.

$$\begin{aligned}
A &= A_1 \cdot d_B + A_2 \cdot (d_S - d_B) + A_3 \cdot (1 - d_S) \\
B &= B_1 \cdot d_B + B_2 \cdot (d_S - d_B) + B_3 \cdot (1 - d_S) \\
C &= C_1 \cdot d_B + C_2 \cdot (d_S - d_B) + C_3 \cdot (1 - d_S) \\
E &= E_1 \cdot d_B + E_2 \cdot (d_S - d_B) + E_3 \cdot (1 - d_S)
\end{aligned}$$

$$\begin{aligned}
\frac{dx}{dt} &= Ax + Bu \\
y &= Cx + Eu
\end{aligned} \tag{4.20}$$

Assuming perturbations in state variables  $\hat{x}$  around the steady state DC value of X, then

$$x = X + \hat{x} \tag{4.21}$$

Similarly, assuming perturbations in duty cycles ( $d_B$  and  $d_S$ ) and input (u),

$$\begin{aligned}
d_S &= D_S + \hat{d}_S \\
d_B &= D_B + \hat{d}_B \\
u &= U + \hat{u}
\end{aligned} \tag{4.22}$$

For obtaining small signal model, the perturbations are assumed to be very small compared to steady state DC values, i.e.,  $\hat{d}_S \ll D_S$ ,  $\hat{d}_B \ll D_B$  and  $\hat{u} \ll U$ . Also, these perturbations are assumed to be constant during one switching period. Substituting (4.21) and (4.22) into (4.20) and linearizing by neglecting second-order terms, the state space model of the converter is obtained as below.

$$\begin{aligned}
\dot{\hat{x}} &= \frac{d\hat{x}}{dt} = A\hat{x} + B\hat{u} + F\hat{d}_B + G\hat{d}_S \\
\hat{y} &= C\hat{x} + (C_1 - C_2)X\hat{d}_B + (C_2 - C_3)X\hat{d}_S
\end{aligned} \tag{4.23}$$

where  $F = (A_1 - A_2)X + (B_1 - B_2)U$ ,  $G = (A_2 - A_3)X + (B_2 - B_3)U$  and  $X = -A^{-1}BU$ . Applying Laplace transform to (4.23) and rearranging, control-to-output transfer function of battery stage is obtained as

$$\frac{\hat{y}(s)}{\hat{d}_B(s)} = C(sI - A)^{-1}F + (C_1 - C_2)X \tag{4.24}$$

Where I is identity matrix. Substituting the values for C, A, F,  $C_1$ ,  $C_2$  and X from (4.20), (4.23), (4.15) and (4.17), the control-to-inductor current transfer function for battery stage is given by

$$G_{i_B d_B} = \frac{\hat{i}_B(s)}{\hat{d}_B(s)} = \frac{V_{DC}}{D_B R(1 - D_S)} \cdot \left[ \frac{1 + sRC}{s^2 \frac{L_B C}{(1 - D_S)^2} + s \frac{L_B}{R(1 - D_S)^2} + 1} \right] \tag{4.25}$$

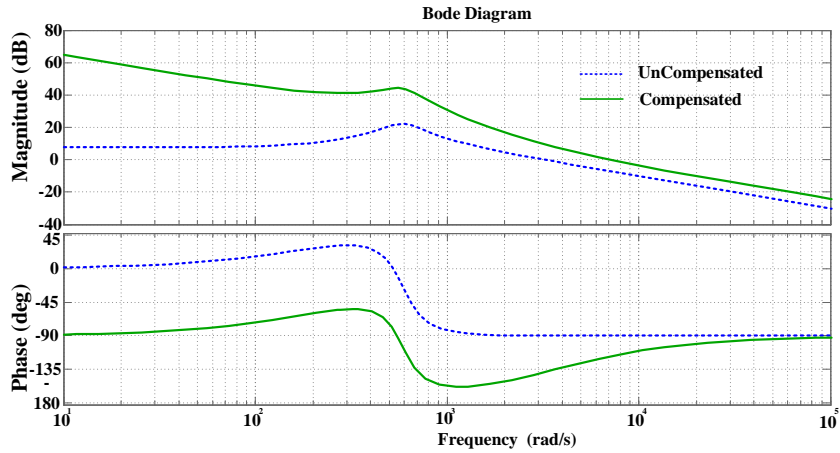


**Figure 4.13.** Bode plot of current controller of battery control logic.

PI controller to regulate battery current is designed based on above transfer function. Bandwidth of the controller is made less than that of supercapacitor stage. The designed controller has a bandwidth of 1 kHz with phase margin of  $60^\circ$ . Bode plot of compensated and uncompensated plant is shown in Figure 4.13. Transfer function of PI controller is given by

$$G_{pi\_i_B} = 1.971 + \frac{7300}{s} \quad (4.26)$$

### 4.3.3 Supercapacitor State-of-Charge Controller

Unlike batteries, supercapacitors have low ESR. So it cannot retain energy for long duration. In order to prevent supercapacitor energy from getting depleted beyond a minimum permissible point, a control logic is devised to maintain the SOC within required limits of (4.6). Whenever this desired range of SOC is violated, the converter enters into HESS Energy exchange mode explained in Section 4.2. When SOC of supercapacitor falls below prescribed minimum limit, it is charged with a constant current,  $I_{CH}$ , with battery power. When SOC exceeds the maximum safe limit, supercapacitor is allowed to discharge its excess energy to battery with a constant current  $-I_{CH}$ . Thus SOC of supercapacitor is maintained within the limits by either buck (SC charging) or boost (SC discharging) operation as explained in Section 4.2. The control logic for SOC controller is shown in Figure 4.12. A PI controller is used to regulate the supercapacitor current. The controller is designed based on buck mode control-to-output transfer function. Since its design is not within the scope, it is not shown here. Same controller is sufficient for buck and boost operation in HESS Energy exchange mode explained above since transfer function is same

for both the operations. It is to be noted that whenever HESS Energy exchange mode is active, either due to low SOC or high SOC, DC microgrid is isolated from HESS electrically.

#### 4.4 Simulation Study and Discussion

In this segment, the simulation results are displayed for two test cases. The nominal parameters for simulation study are presented in Table 4.1. The entire model is implemented using MATLAB. The PV array is a unidirectional, which is connected to the boost converter. The two operating cases are presented in the following sections for step change in PV generation and load demand.

**Table 4.1** Nominal parameters for simulation study

S. No	Parameters	Value
1	MPPT Voltage ( $V_{mpp}$ )	32 V
2	MPPT Current ( $I_{mpp}$ )	3 A
3	MPPT Power ( $P_{mpp}$ )	96 W
3	SC Voltage ( $V_{sc}$ )	32 V
4	SC inductance ( $L_s$ )	0.355mH
5	Battery Voltage( $V_B$ )	24 V
6	Battery inductance ( $L_B$ )	0.3mH
7	Boost inductance ( $L$ )	4.1mH
8	Resistance ( $R$ )	24 $\Omega$
9	DC grid voltage( $V_{DC}$ )	48 V
10	Capacitance ( $C$ )	300 $\mu$ F

##### 4.4.1 Case-I: Step change in PV generation

The simulation results for step change in PV generation as shown in Figure 4.14. Due to atmosphere variations power produced by the PV panel increases from 96W to 192W at  $t=0.3$ sec and bring back to 96W at  $t=0.6$ sec. In this case load power requirement constant at 96W. As PV power is more than the load power requirement, DC grid voltage increases more than 48V. Immediately SC absorbs the excess power of 96W in short duration until battery can regulate the grid voltage to 48V. Thus, the battery and SC charge according to energy management strategy to maintain the DC grid voltage constant at 48V.

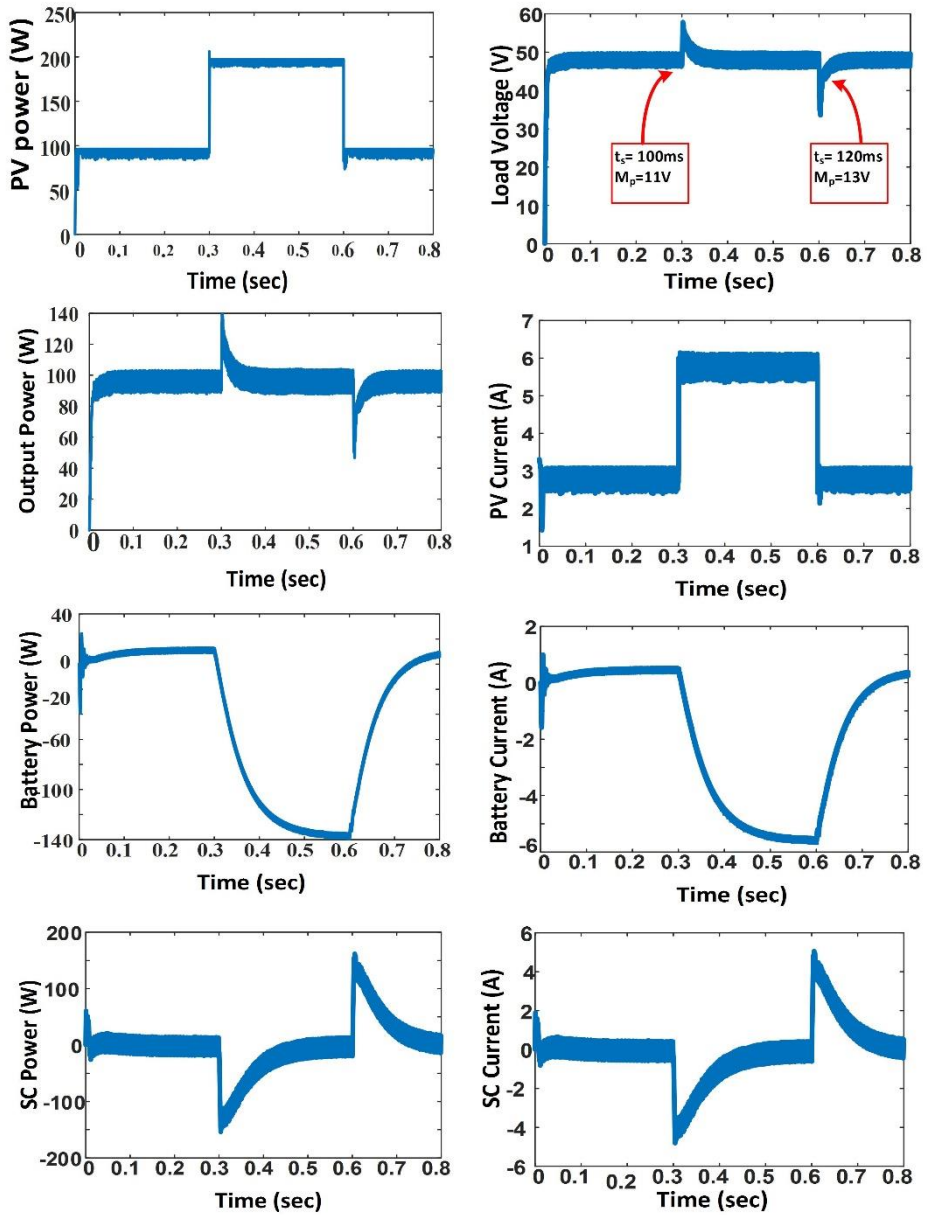


**Figure 4.14** Simulation results for step change in PV generation

#### 4.4.2 Case-II: Step change in load demand

Simulation results for step change in load demand as shown in Figure 4.15. In this case PV power generation constant at 96W. The load power demand increases from 96W to 192W and bring back to 96W at  $t=0.3\text{sec}$  and  $t=0.6\text{sec}$  respectively. Between 0.3 to 0.6 sec, the load demand increases to 192W, which is beyond the power range of PV panel. This creates a power imbalance between source power and load power. Immediately HESS respond, SC supply transient component of power demand and battery supplies steady state component of power demand. The DC grid voltage regulated for step increase and decrease in load demand for 100msec and 80msec respectively.

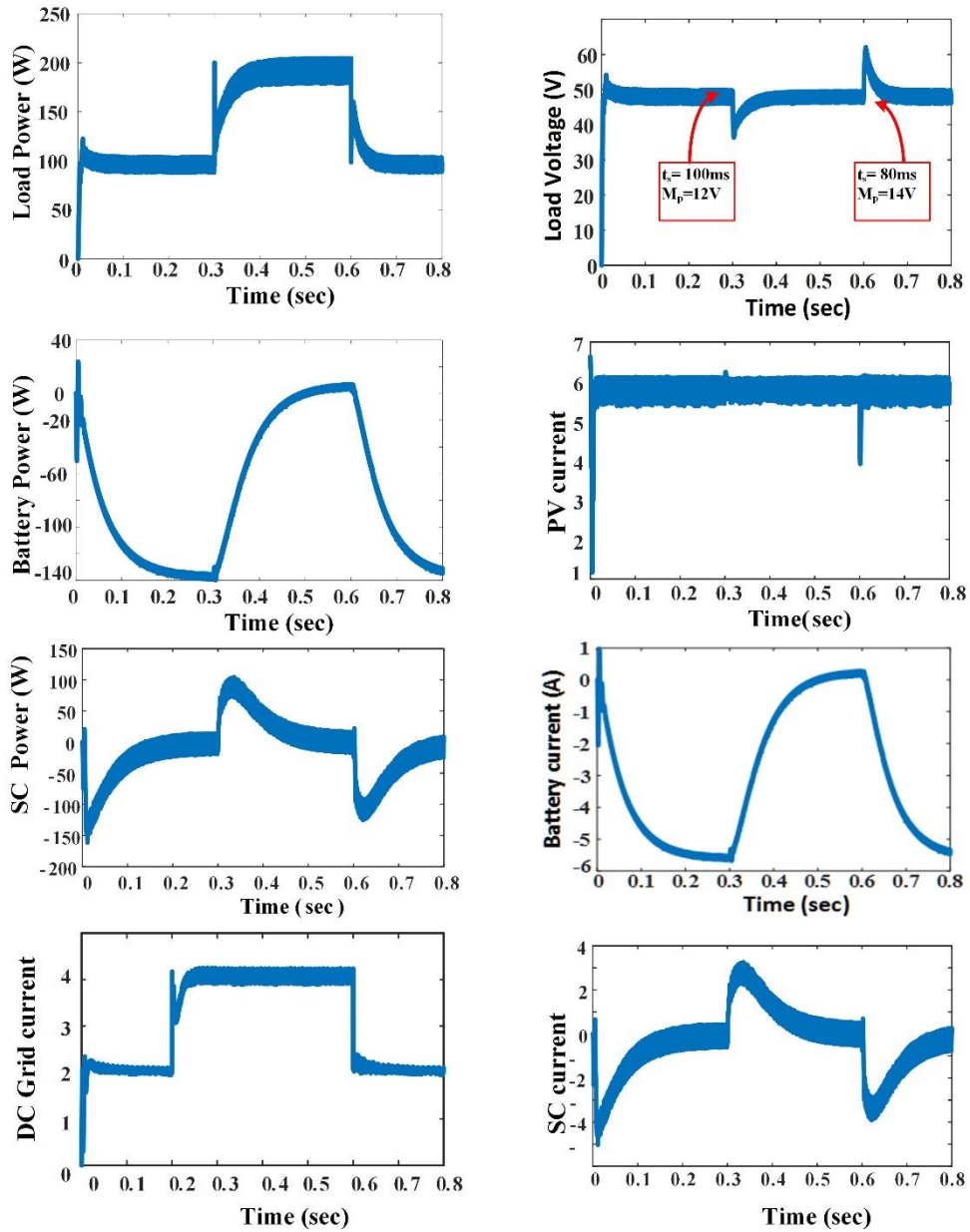


Figure 4.15 Simulation results for step change in load demand

## 4.5 Experimental Results

A low power hardware prototype is developed to validate the performance of proposed unified controller for two-input bidirectional converter as shown in Figure 4.16. The digital controller used is dSPACE DS1104. The PV source is emulated by a regulated power supply (RPS) whose current is controlled by a boost converter. HESS is wired up using a single unit each of Exide Chloride Safe power 12 V, 7 Ah lead-acid battery and Maxwell BMOD0058 16 V, 58 F supercapacitor. The double-input bidirectional converter is built using six mosfet switches IRF540N.

**Table 4.2** Parameters of the experimental system

S. No	Parameter	Value
1	MPPT Voltage ( $V_{pv}$ )	12 V
2	MPPT Current ( $i_{pv}$ )	1.4 A
3	SC Voltage ( $V_{sc}$ )	10 V
4	SC inductance ( $L_s$ )	1.43mH
5	Battery Voltage( $V_B$ )	12 V
6	Battery inductance ( $L_B$ )	4.8mH
7	Boost inductance (L)	4.1mH
8	Resistance (R)	$25 \Omega$
9	DC grid voltage( $V_{dc}$ )	20 V
10	Capacitance (C)	$150 \mu F$

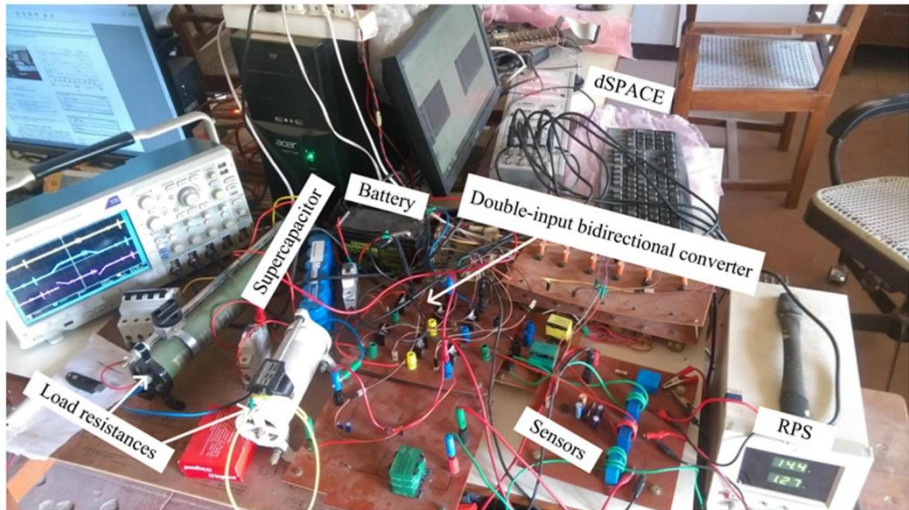


**Figure 4.16.** Low power hardware prototype developed

The performance of DC microgrid, powered by emulated PV source, supported by HESS is verified for all the three cases mentioned in Section 4.2, i.e., 1) HESS charging mode, 2) HESS discharging mode and 3) HESS Energy exchange mode. DC grid specifications are given in Table 4.2. DC microgrid is setup at a nominal voltage of 20 V.

#### 4.5.1 HESS Charging Mode

Here performance of designed controller in the scenario of surge in microgrid voltage either due to increased PV generation or due to decrease in load is analysed. Waveforms are given in Figure 4.17. In this case, surge in microgrid voltage is realized by increasing load resistance. Initially load resistance  $R=25 \Omega$  up till instant  $t_1$ . At  $t_1$ , load resistance is increased

to  $35 \Omega$  and as a result in decrease in load demand, the excess energy in dc grid causes a surge in grid voltage. Immediately HESS responds in such a manner that transient component of current is charging supercapacitor and battery charging current is allowed to increase slowly till steady state value at instant  $t_2$ .

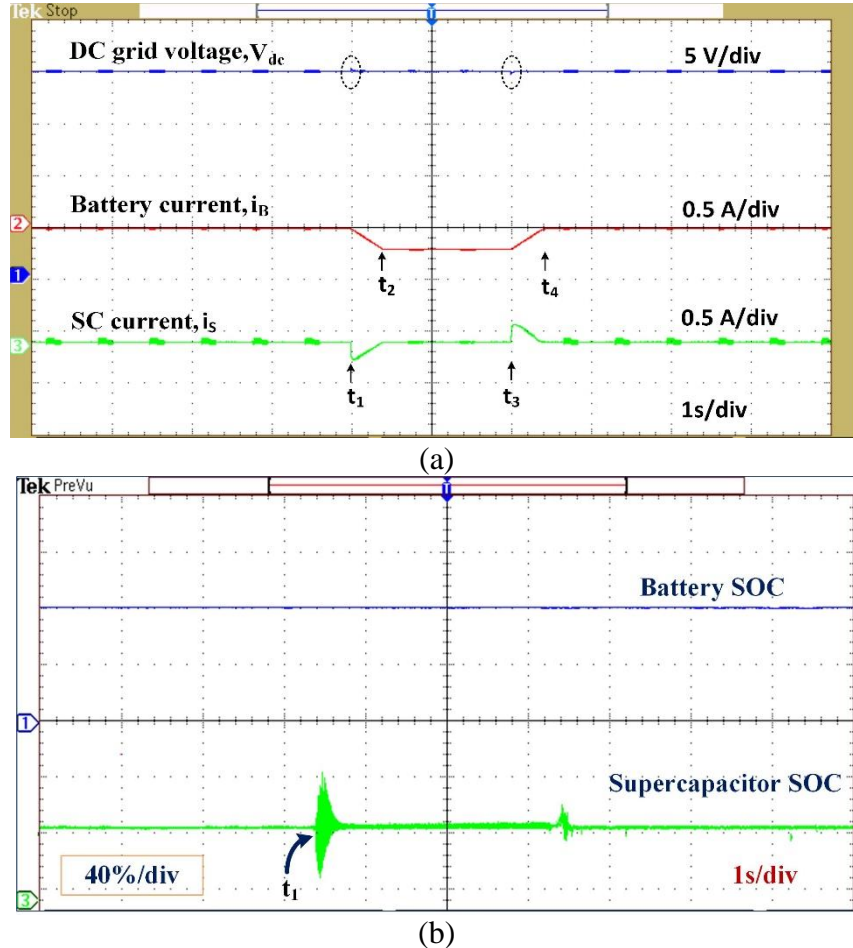


**Figure 4.17.** Experimental results for HESS Charging mode. (a) DC microgrid voltage ( $V_{dc}$ ), battery current ( $i_B$ ) and supercapacitor current ( $i_S$ ). (b) Battery and Supercapacitor SOC waveform.

The load resistance is brought back to original condition of  $R = 25 \Omega$  at instant  $t_3$ . Battery and supercapacitor then return to its floating state as it was before  $t_1$ . At instants  $t_1$  and  $t_3$ , dc microgrid voltage is retained at 20 V almost instantly as indicated by small spikes in the figure. Battery and Supercapacitor SOC is shown in Figure 4.17(b). At instant  $t_1$ ,  $SOC_{SC}$  is shown to be increasing indicating charging of supercapacitor. After the transient current has died out, supercapacitor remains idle as indicated by constant SOC. Battery SOC is almost constant, its energy not depleted fast compared to supercapacitor.

#### 4.5.2 HESS Discharging Mode

In this case, performance of controller is pitted against decrease in microgrid voltage either due to decrease in PV generation or due to increase in load. Waveforms are shown in Figure 4.18. Here, dip in microgrid voltage is realized by a decrease in PV generation. Decrease in PV generation is implemented by decreasing the input current (IPV) of boost converter connected to RPS while maintaining input voltage (VPV) constant at 12 V.

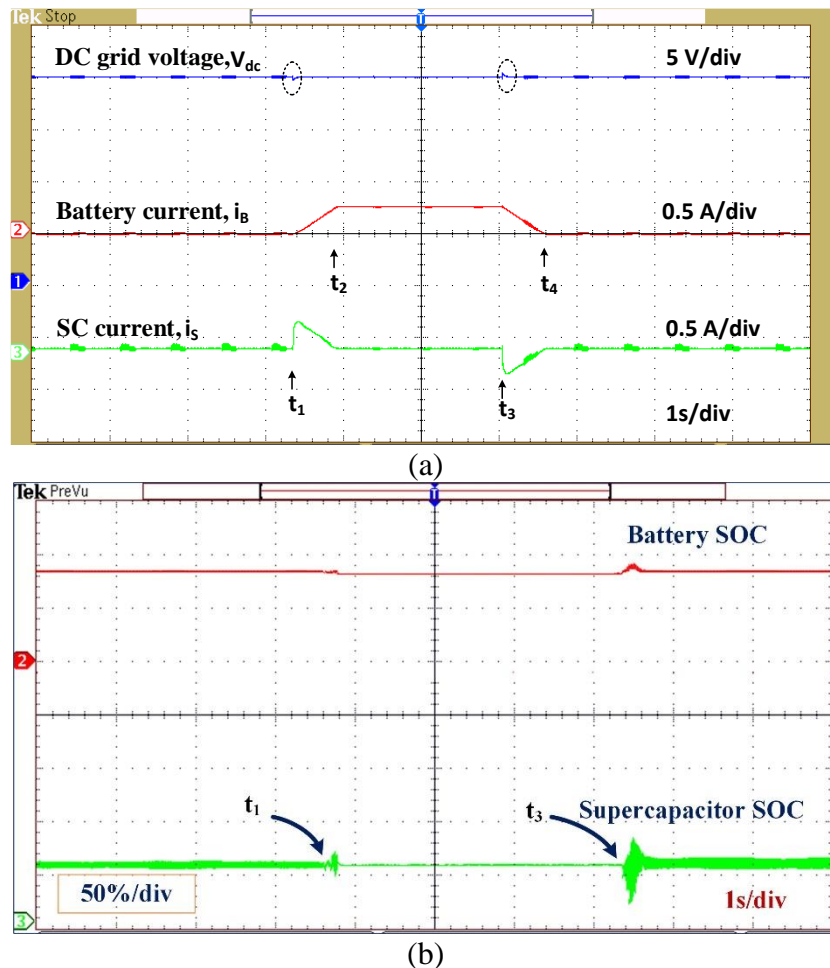


**Figure 4.18.** Experimental results for HESS discharging mode. (a) DC microgrid voltage ( $V_{dc}$ ), battery current ( $i_B$ ) and supercapacitor current ( $i_S$ ). (b) Battery and Supercapacitor SOC waveform.

At instant  $t_1$ , IPV is decreased from 1.3 A to 1.1 A. This causes dc microgrid voltage to dip since there exists a power mismatch between source and load. The deficient power is then fed by HESS by discharging battery and supercapacitor. Transient current is met by supercapacitor and steady state current is supplied by battery as is evident from current waveforms in Figure 4.18(a). Combined action of battery and supercapacitor maintain dc microgrid voltage constant at nominal value of 20 V. Small spike in voltage waveform is negligible due to fast dynamics of HESS.

At instant  $t_3$ , PV generation is reverted back to normal by setting  $I_{PV} = 1.3$  A. Battery current now slowly reduces to zero whereas supercapacitor instantly responds to bring dc microgrid voltage back to nominal value almost instantly. Battery and Supercapacitor SOC waveform is also shown in Figure 4.18(b) to validate the above explained operation. When PV generation is decreased at instant  $t_1$ ,  $SOC_{SC}$  is found to decrease as long as supercapacitor supplies current indicating discharge operation of supercapacitor. After that supercapacitor is idle as indicated by constant SOC waveform. Similarly at instant  $t_3$ , SOC is increased to indicate charging of supercapacitor after which it stays idle.

#### 4.5.3 HESS Energy Exchange Mode

In this mode, power flow from battery to supercapacitor is illustrated. Waveforms are shown in Figure 4.19. Before time instant  $t_1$  HESS is disconnected from dc microgrid. Due to reduced PV generation grid voltage is now 18 V. At instant  $t_1$ , HESS is active to make grid voltage at nominal value of 20 V.

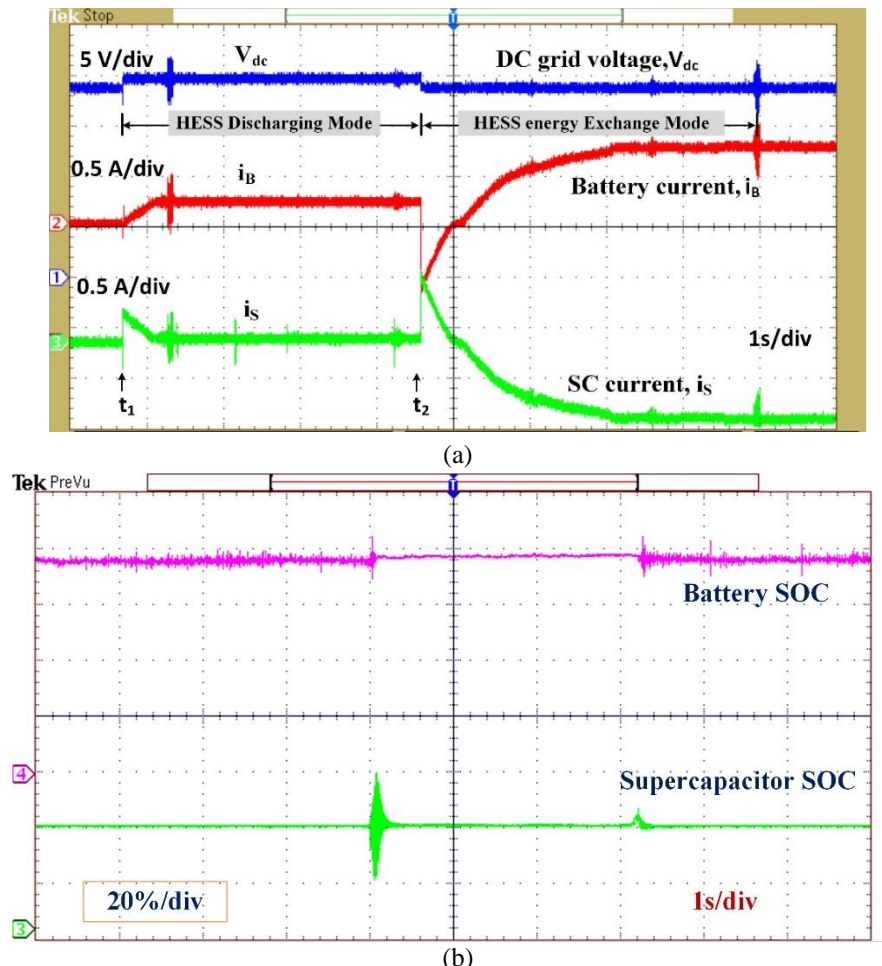


**Figure 4.19(a).** Experimental results for HESS Energy exchange mode. DC microgrid voltage ( $V_{dc}$ ), battery current ( $i_B$ ) and supercapacitor current ( $i_S$ ). Transition from discharging mode to energy exchange mode is shown. (b) Battery and Supercapacitor SOC waveform.

Battery and supercapacitor waveforms are as explained in HESS discharging mode. Current waveforms in Figure 4.19 (a) prove the same. SOC waveform is also given in Figure 4.19 (b). SOC is at 50% just before  $t_2$ .

At  $t_2$ , SOC falls below 50%, which is taken as prescribed lower limit of SOC range, and HESS mode now shifts from HESS discharging mode to HESS Energy exchange mode. Battery will now charge supercapacitor at a constant current of  $I_{CH} = 0.8$  A. SOC is found to be increasing indicating continuous charging of supercapacitor. During energy exchange mode, HESS is disconnected from DC microgrid which is now evident from voltage waveform not being at nominal value of 20 V.

## 4.6 Summary

A controller was designed for the two-input bidirectional converter for HESS control. The performance of designed controller is analyzed in various cases for the application of voltage regulation in DC microgrid. Controller could effectively stabilize DC microgrid against disturbances from source PV generation as well as load variations. It could utilize inherent fast dynamics of supercapacitor for absorbing incoming transients to the microgrid. This unified controller proved to be enough for both charging and discharging operation of HESS. Moreover, decoupled, separate and independent control of supercapacitor and battery power was achieved as well as power flow between them. It can also be used in the case of hybrid electric vehicle applications where two or more sources supply power. Operation mode of HESS converter for maintaining SOC of supercapacitor always within desired limit was also demonstrated.

# **Chapter-5**

## **Modelling, Analysis and Design of Novel Control Scheme for Two-input Bidirectional DC-DC Converter for HESS in DC Microgrid Applications**

# Chapter-5

## Modelling, Analysis and Design of Novel Control Scheme for Two-input Bidirectional DC-DC Converter for HESS in DC Microgrid Applications

### 5.1 Introduction

This chapter presents with an advanced controller for multiple input bidirectional DC-DC power converter (MIPC) for HESS. This MIPC not only provides decoupled control of battery and SC power but also provides energy exchange between storage devices within the system. In conventional control scheme, neglects uncompensated power from the battery system and power sharing entirely depends on low pass filter (LPF). The uncompensated power from the battery system is used to improve the SC system in the proposed control scheme. This improves the current stresses, increase life cycle of the battery and improve the overall system performance to the step change in PV generation and load demand provides faster DC grid voltage. The results of the simulation and experiments are developed.

### 5.2 HESS Supported RES Configuration

The architecture of two-input bidirectional converter configuration of HESS aided RES is illustrated in Figure.5.1. In Figure.5.1 includes off-grid RES involving PV and HESS with the arrangement of battery-supercapacitor bank. For DC microgrid, PV generation is one of the most important RES. Boost converter is used to extract maximum power from PV panel and to interface with the DC microgrid. Combination of battery-SC bank make the HESS configuration and in case of any mismatch of PV generation and load demand, HESS responds immediately to provide fast regulation of DC grid voltage.

Various modes of operation are presented in detail [113]. Modified converter operation is explained here. It consists of three switching legs. Battery ( $V_B$ ) and supercapacitor ( $V_s$ ) modules are connected to legs 2 and 3 respectively. DC microgrid ( $V_{DC}$ ) is connected to leg 1. In this converter topology, battery voltage is taken as greater than SC voltage and less than DC grid voltage. The high frequency inductors  $L_B$  and  $L_s$  are connected

between legs 1, 2 and 1, 3 respectively. Different modes of operations are explained in the following sections.

### 5.2.1 Power flow from HESS to DC grid

The switching sequence of the power semiconductor devices in this mode of operation is given in Table 5.1. The converter operation in this mode can be divided into three time intervals in an overall cycle time of  $T_S$  as shown in Figure 5.2(d). The switching devices  $S_5$ ,  $S_2$  are operated with duty cycle  $d_S$  and complimentary of these signals drives switches  $S_6$ ,  $S_1$ . Switch  $S_3$  is operated with duty cycle  $d_B$  and  $S_4$  is operated with its complementary.

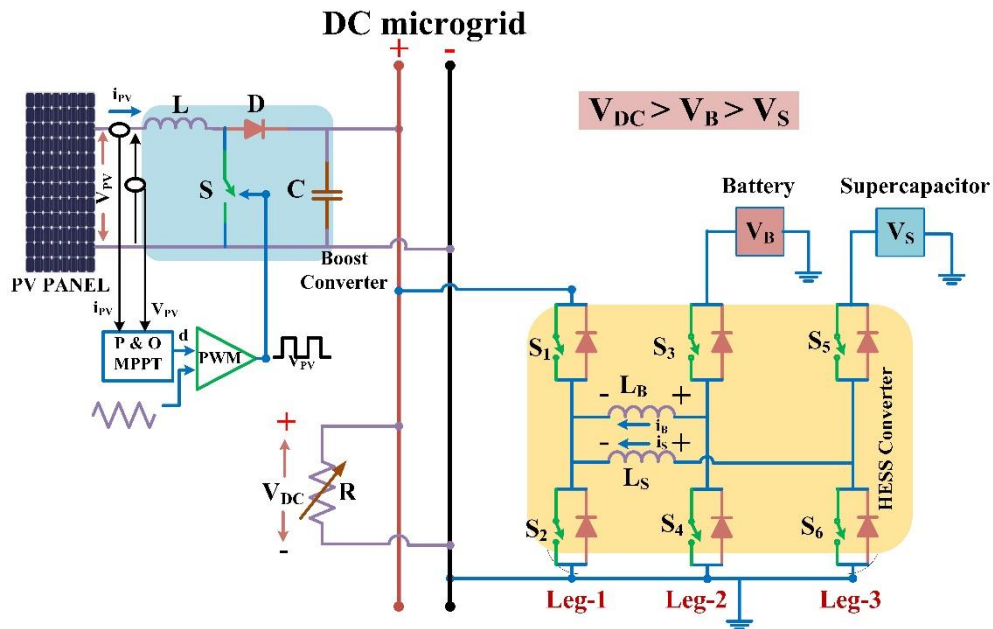


Figure 5.1 DC microgrid architecture operation of HESS with PV system

DC microgrid voltage varies from steady state value whenever there exist a mismatch between PV output power and load power. DC microgrid voltage reduces, if PV power generation falls due to reduced solar irradiance or load exceeds PV generation capability. During this mode, HESS supplies deficient power required by the load to balance the DC microgrid. By properly controlling the bidirectional converter, power can flow from battery and SC bank to DC microgrid in this mode, equivalent circuit of power flow from HESS to DC microgrid is represented in Figure 5.2 (a) (b) (c). At time  $t=t_0$ , switching devices  $S_2$ ,  $S_3$  and  $S_5$  are turned on which will increase the inductor currents  $i_B$  and  $i_S$  linearly with a slopes  $V_B/L_B$  and  $V_S/L_S$  respectively. At time  $t_1$ , switch  $S_3$  is turned off to provide free-wheeling path for battery current  $i_B$  through body diode of  $S_4$ . After dead time interval for switches  $S_3/S_4$ , the switch  $S_4$  is turned on. At time  $t_2$ , the switches  $S_2$  and  $S_5$  are turned off, SC current is to flow through the body diodes of switches  $S_1$  and  $S_6$  with a negative slope of  $V_{DC}/L_S$ .

Battery current  $i_B$  also flows through body diode of  $S_1$  with a negative slope of  $V_{DC}/L_B$ . At time  $t_3$ , switches  $S_1$ ,  $S_4$  and  $S_6$  are turned off. Consequently, body diodes of switches  $S_2$ ,  $S_3$  and  $S_5$  will conduct in order to maintain flow of inductor currents. The currents,  $i_B$  and  $i_S$  flow through with a positive slope of  $V_B/L_B$  and  $V_S/L_S$  respectively. After dead time interval, switching pulses are given to switches  $S_2$ ,  $S_3$  and  $S_5$  turn on with ZVS. Where  $d_B$  is the duty ratio of switch  $S_3$  and  $d_S$  is the duty ratio of switches  $S_2$  and  $S_5$ .

**Table: 5.1** switching states in different time intervals

Time scale	T <sub>1</sub>	T <sub>2</sub>	T <sub>3</sub>
Operating switches	$S_2, S_3, S_5$	$S_2, S_4, S_5$	$S_1, S_4, S_6$

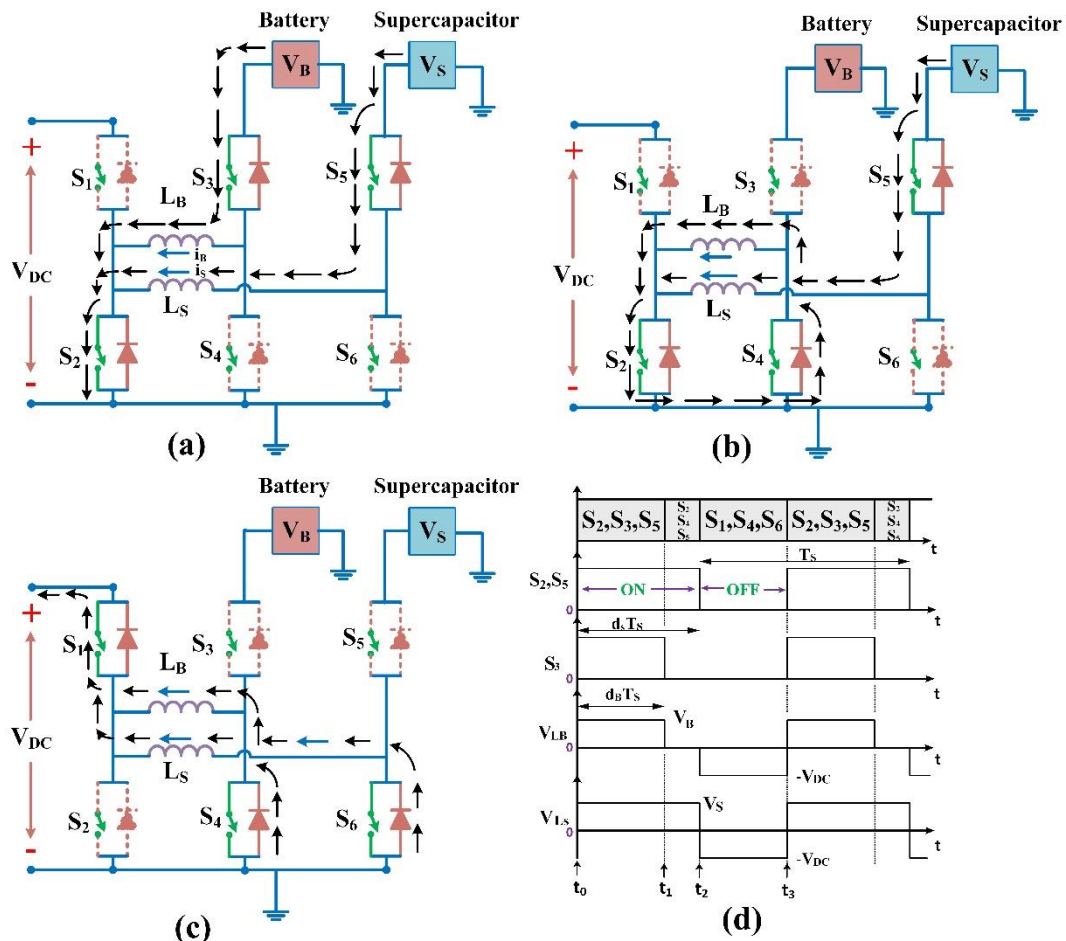


**Figure 5.2.** Equivalent circuit of two-input bi-directional converter (a)  $S_2, S_3, S_5$  operates (b)  $S_2, S_4, S_5$  operates (c)  $S_1, S_4, S_6$  operates (d) steady state waveforms in discharging mode

After applying volt-second balance to inductors  $L_B$  and  $L_S$  gives the relation between DC grid voltage to the battery and SC as shown in Table 5.3. Since battery voltage  $V_B$  is

greater than SC voltage  $V_S$ ,  $d_B$  will always be less than  $d_S$ . Power flow between battery and SC to DC microgrid can be controlled independently by controlling  $d_B$  and  $d_S$ .

### 5.2.2 Power flow from DC grid to HESS

Whenever PV generated power exceeds that required by the load or when load demand decreases, there is excess power existing in the DC microgrid which results in increase of DC grid voltage. The battery and SC will store extra power generated from PV panel. Hence, in this condition power flows from DC microgrid to HESS. The converter operation using equivalent circuits in this mode can be explained in three switching time intervals as shown in Figure 5.3(a-d). Operating switches in each time interval is tabulated in Table 5.2.

**Table: 5.2** switching states in different time intervals

Time scale	$T_1$	$T_2$	$T_3$
Operating switches	$S_1, S_4, S_6$	$S_2, S_4, S_5$	$S_2, S_3, S_5$

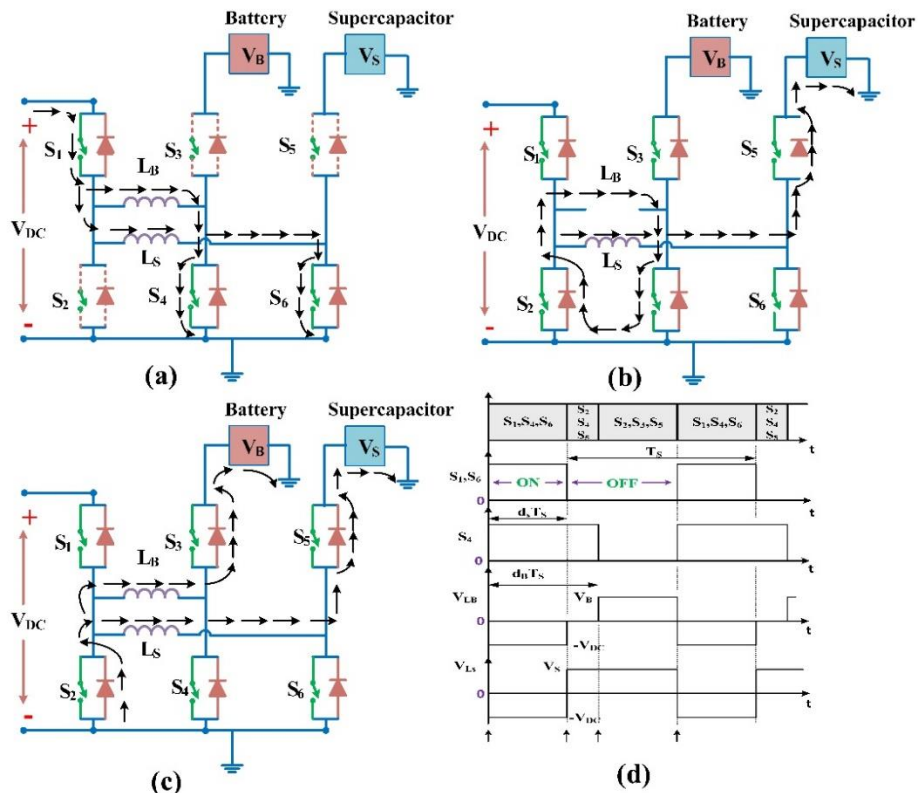


**Figure 5.3.** Equivalent circuit of two-input bi-directional converter (a)  $S_1, S_4, S_6$  operates (b)  $S_2, S_4, S_5$  operates (c)  $S_2, S_3, S_5$  operates (d) steady state waveforms in charging mode

At time  $t_0$ , switches  $S_1$ ,  $S_4$  and  $S_6$  are operated to increase the inductor currents  $i_B$  and  $i_S$  with a negative slope of  $V_{DC}/L_B$  and  $V_{DC}/L_S$  respectively. In between the time  $t_0$  to  $t_1$  inductors

stores energy. At time  $t_1$ , switches  $S_1$  and  $S_6$  are turned off. Body diodes of  $S_2$  and  $S_5$  are turned on to maintain inductor current  $i_s$ . Now supercapacitor will charge by using energy stored in the inductor  $L_s$ . Inductor current  $i_B$  free-wheels through body diode of switch  $S_2$ . At time instant  $t_2$ , switch  $S_4$  is turned off. Inductor current  $i_s$  flows through the body diode of switch  $S_3$  with a slope of  $V_s/L_s$ . Now battery gets charged using the energy stored in inductor  $L_B$ . At time instant  $t_3$ , switches  $S_2$ ,  $S_3$  and  $S_5$  are turned off, consequently body diodes of switches  $S_1$ ,  $S_4$  and  $S_6$  turned on to maintain flow of inductor currents. If  $d_B$  is the duty cycle of switch  $S_4$  and  $d_s$  is the duty cycle of switches  $S_1$  and  $S_6$ , apply volt-second balance to the inductors  $L_B$  and  $L_s$  gives the relation between SC and battery voltage to DC grid voltage as presented in Table 5.3.

### 5.2.3 Power flow from Battery to SC (Energy Exchange mode)

Supercapacitor is a high power density unit, it can't deliver power supply for longer duration like battery. To maintain supercapacitor charge within the limits, it has to be charged using battery for proper functioning of HESS. In this mode power flow from battery to supercapacitor. Equivalent circuit and steady-state waveforms in energy exchange mode operation have been shown in Figure 5.4.

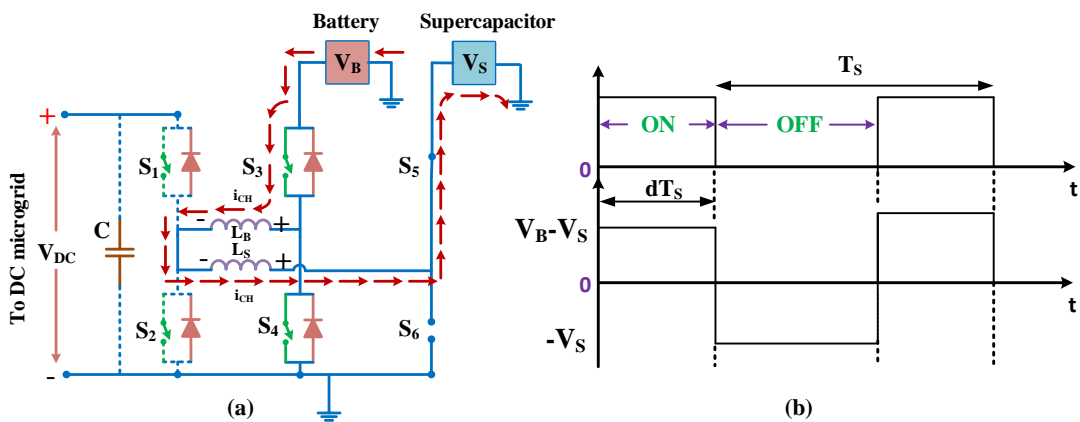


Figure 5.4. HESS Energy exchange mode of operation (a) equivalent circuit (b) Steady-state waveforms

In energy exchange mode, DC microgrid is disconnected from HESS by opening switches  $S_1$  and  $S_2$ . In this mode switching pairs  $S_3/S_4$  and  $S_5/S_6$  are works in complementary manner. Switch  $S_5$  is completely ON in this mode which causes switch  $S_6$  is completely open circuited as shown in Figure 5.4. Switch  $S_3$  is operated with duty cycle of  $d$  and switch  $S_5$  is completely on to make power flow from battery to supercapacitor involves like buck operation. The two inductors are connected in series to make reduce the current ripple. By

controlling duty cycle  $d$ , power flow from battery to supercapacitor can be controlled. Applying volt-second balance to equivalent inductance  $L_{eq}$  ( $L_{eq}=L_B+L_S$ ) gives the relation between battery voltage and SC voltage as presented in Table 5.3.

**Table 5.3:** Relation between different voltages in each mode

<b>Power flow from HESS to DC grid</b>
$V_{DC} = \frac{d_S}{1-d_S} \cdot V_S \quad , \quad V_{DC} = \frac{d_B}{1-d_B} \cdot V_B$
<b>Power flow from DC grid to HESS</b>
$V_S = \frac{d_S}{1-d_S} \cdot V_{DC} \quad , \quad V_B = \frac{d_B}{1-d_B} \cdot V_{DC}$
<b>Power flow from Battery to SC (Energy Exchange mode)</b>
$V_S = d \cdot V_B$

#### 5.2.4 Mathematical design calculations of filter parameters

For design of filter inductor for bidirectional DC-DC converter is assumed to be always operated at continuous conduction mode (CCM). The mathematical design of filter inductor and capacitor for various converters is given in [114-115].

The calculation of peak-to-peak inductor current ( $\Delta i_L$ ) of boost converter during switch ON period is calculated as

$$\begin{aligned} \Delta i_L &= i_L(DT) - i_L(0) \\ \Delta i_L(ON) &= \frac{V_{PV} \cdot DT}{L} = \frac{V_{PV} \cdot D}{f_S L} = \frac{V_{DC} \cdot D \cdot (1-D)}{f_S L} \end{aligned} \quad (5.1)$$

Similarly,  $\Delta i_L$  during switch OFF period of time

$$\begin{aligned} \Delta i_L &= i_L(DT) - i_L(T) \\ \Delta i_L(OFF) &= \frac{(V_{DC} - V_{PV})(1-D)T}{L} = \frac{V_{DC} \cdot D \cdot (1-D)}{f_S L} \end{aligned} \quad (5.2)$$

For designing DC microgrid voltage ( $V_{DC}$ ) to 20V, load resistance can be selected as follows

$$R_{load} = \frac{V_{DC}^2}{P_{max}} = \frac{20^2}{16} = 25 \Omega$$

For designing filter inductor, the peak-to-peak inductor current ( $\Delta i_L$ ) is limited to 5% of total current in this work, inductor ( $L$ ) is defined as follows

$$L = \frac{V_{PV} \cdot D}{f_S \cdot \Delta i_L} \quad (5.3)$$

Similarly, the output filter capacitor( $C$ ) reduces the voltage ripple, thus can be calculated as

$$C = \frac{D \cdot V_{DC}}{f_s \cdot R_{load} \cdot \Delta V_{DC}} \quad (5.4)$$

### 5.3 Proposed Control System Scheme of HESS

The control system block diagram representation of conventional and proposed control scheme is shown in Figure 5.5(a), (b). The proposed control scheme will contribute a controller which will not only provide good closed loop performance but also provide stable operation amidst converter dynamics and external disturbances. The nominal value of DC link voltage ( $V_{DC}$ ) is compared with a reference voltage ( $V_{DC,ref}$ ) and the error is offered to the PI controller in both schemes, which generates total current ( $i_{tot}$ ) from ESS in this process. In the conventional control scheme total current is divided in to low-frequency ( $I_{LOW}$ ) and high-frequency ( $I_{HIGH}$ ) components of current using low pass filter, which is given as reference currents to battery and supercapacitor loops respectively and it is represented in Figure 5.5 (a). In the conventional control scheme, SC current reference consists of high frequency component and battery error component which is explained in proposed control scheme. Conventional control scheme neglects battery current error arising due to the battery controller.

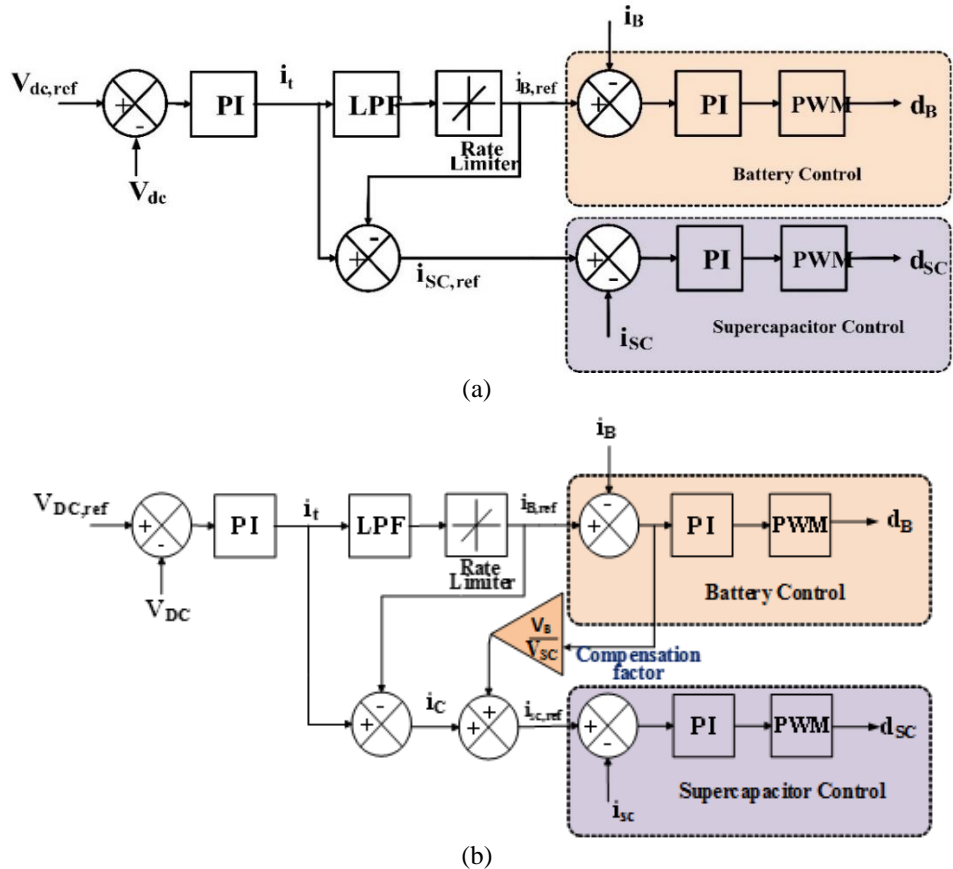


**Figure 5.5.** Overall control system description for current bifurcation b/w SC and battery unit (a) conventional control scheme (b) proposed control scheme

The proposed control scheme is represented in Figure 5.5(b). The power flow in DC grid under PV generation and load changes are classified into two types (i) steady state power component ( $P_{std}$ ), and (ii) transient power component ( $P_{tran}$ ). The power balance equation given as

$$P_{dc}(t) - P_{ren}(t) = P_B(t) + P_{SC}(t) = P_{std}(t) + P_{tran}(t) \quad (5.5)$$

Where,  $P_{dc}(t)$ ,  $P_{ren}(t)$ ,  $P_B(t)$  and  $P_{SC}(t)$  are the DC grid power, RES power, battery and SC power respectively. The HESS charges and discharges, maintaining the DC grid voltage in predefined limits. The sum of battery and SC powers are given as

$$P_B(t) + P_{SC}(t) = P_{std}(t) + P_{tran}(t) = V_{DC} \cdot i_{tot}(t) \quad (5.6)$$

Regulates the DC link voltage by controlling total current demand represented as follows

$$i_{tot} = \frac{P_{std}(t) + P_{tran}(t)}{V_{DC}(t)} = i_{std}(t) + i_{tran}(t) \quad (5.7)$$

Voltage control loop calculates the total current ( $i_{tot}$ ) demand as follows:

$$i_{tot}(t) = i_{std}(t) + i_{tran}(t) = K_{p,v} \cdot v_{err} + K_{i,v} \cdot \int v_{err} dt \quad (5.8)$$

Where  $K_{p,v}$  and  $K_{i,v}$  are the proportional and integral constants of the outer voltage control loop.  $v_{err}$  represents voltage error. For achieving better DC bus voltage regulation by effective sharing of total current demand( $i_{tot}$ ). In conventional control scheme, low pass filter (LPF) extract steady state part from total current( $i_{tot}$ ).

$$i_{B,ref}(s) = i_{std}(t) = \frac{w_c}{s+w_c} \cdot i_{tot}(s) \quad (5.9)$$

Where  $w_c$  represents LPF cut-off frequency and  $i_{B,ref}(s)$  represents the battery current reference for the battery control loop. Steady state current is controlled by battery system. Due to slow response of battery system, uncompensated power is observed from the battery system. The battery uncompensated power is given as follows.

$$P_{B\_un}(s) = (i_{B,ref}(s) - i_B(s)) \cdot V_B(s) \quad (5.10)$$

$$P_{B\_un}(s) = i_{B,err}(s) \cdot V_B(s) \quad (5.11)$$

Where  $P_{B\_un}(s)$  is the uncompensated power from the battery system. In the proposed control strategy, uncompensated power is utilized to improve the performance of

the SC. Utilizing both uncompensated power and transient current component to design new SC reference current, is given as follows.

$$i_{tran}(s) = \left(1 - \frac{w_c}{s+w_c}\right) \cdot i_{tot}(s) \quad (5.12)$$

$$i_{SC,ref}(s) = i_{tran}(s) + (i_{B,ref}(s) - i_B(s)) \cdot \frac{V_B(s)}{V_{SC}(s)} \quad (5.13)$$

The battery and SC reference currents are compared with actual currents. Battery and SC error current are fed to PI controller. The duty cycle is calculated for the respective current references.  $d_B$  and  $d_{SC}$  are the duty cycle for battery control and SC control as shown in Figure 5.5(a) (b).

#### 5.4 Controller Design for HESS

The control system block diagram representation consists of an inner SC current loop and outer voltage loop as shown in Figure 5.6. Similarly, battery current reference is regulated by using current control as shown in Figure 5.7. SC current control loop bandwidth is higher compared to battery current control for the fast response. Inner SC current loop operates faster compared to outer voltage loop. Hence, current loop bandwidth is maintained more than voltage loop. Switching frequency is selected as 10 kHz in this work.

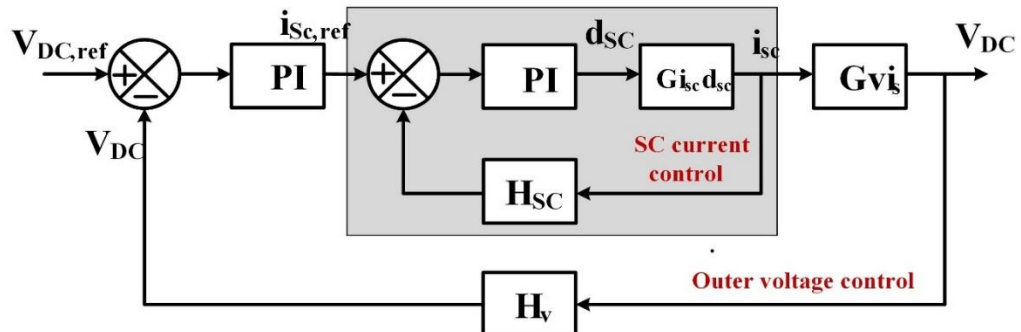


Figure 5.6 Block diagram representation of SC control logic.

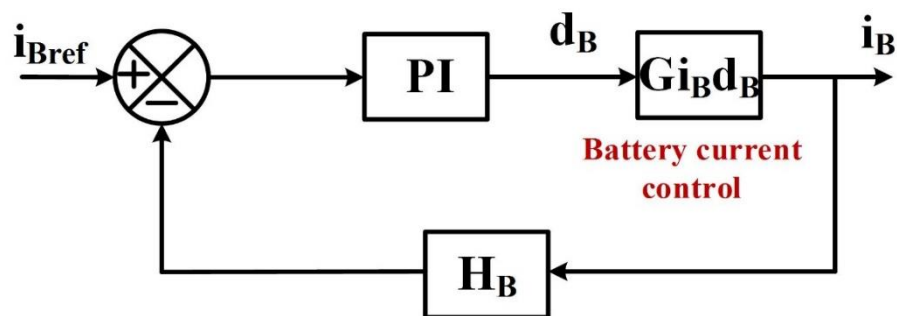


Figure 5.7 Block diagram of battery control logic

### 5.4.1 Design of SC current control loop

The small signal transfer functions, calculated for the control parameters of SC control loop are represented in Table 5.4. In Table 5.4,  $V_{DC}$  represents DC grid voltage,  $i_B$ : battery current,  $i_{SC}$ : SC current,  $d_B$ : duty cycle of battery current controller and  $d_{SC}$ : duty cycle of SC current controller respectively. The open loop transfer function  $G_{i_{SC}d_{SC}}$  is used to determine current compensated parameters. In Table 5.4,  $K_{p,SC}$  and  $K_{i,SC}$  are the proportional and integral gains for the SC current controller. PI controller parameters for SC inner current control are obtained by selecting bandwidth of 1.6 kHz and phase margin of 60°. By using MATLAB SISO tool box, the SC current compensated parameters computed are  $K_{p,SC} = 0.4124$  and  $K_{i,SC} = 2291$ .

**Table 5.4:** small signal linear averaged transfer functions

control to SC current transfer function
$G_{i_{SC}d_{SC}} = \frac{i_{SC}(s)}{d_{SC}(s)} = \frac{V_{DC}(1 + D_{SC})}{R(1 - D_{SC})^3} \left[ \frac{1 + S \frac{RC}{(1 + D_{SC})}}{S^2 - \frac{L_{SC}C}{(1 - D_{SC})^2} + S \frac{L_{SC}}{R(1 - D_{SC})^2 + 1}} \right]$
SC current to output voltage of transfer function
$G_{v_{DC}i_{SC}} = \frac{V_{DC}(s)}{i_{SC}(s)} = \frac{R(1 - D_{SC})}{(1 + D_{SC})} \left[ \frac{1 - S \frac{D_{SC}L_{SC}}{R(1 - D_{SC})^2}}{1 + S \frac{RC}{1 + D_{SC}}} \right]$
control to battery current transfer function
$G_{i_Bd_B} = \frac{i_B(s)}{d_B(s)} = \frac{V_{DC}}{D_B R (1 - D_{SC})^2} \cdot \left[ \frac{1 + SRC}{S^2 \frac{L_B C}{(1 - D_{SC})^2} + S \frac{L_B}{R(1 - D_{SC})^2} + 1} \right]$
PI controller transfer function of inner SC current loop
$G_{pi,SC} = K_{p,SC} + \frac{K_{i,SC}}{S}$
PI controller transfer function of battery current loop
$G_{pi,BAT} = K_{p,BAT} + \frac{K_{i,BAT}}{S}$
PI controller transfer function of outer voltage control loop
$G_{pi,v} = K_{p,v} + \frac{K_{i,v}}{S}$

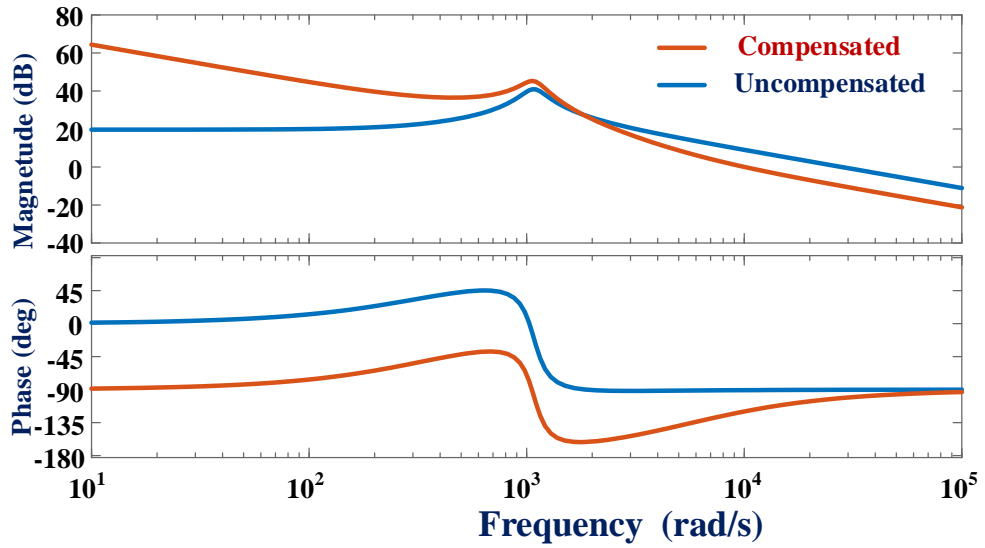


**Figure 5.8.** Bode plot of inner SC current logic for with and without compensation

The open loop and closed loop transfer functions for SC current control loop are determined for stability analysis of the system.

$$G_{ol\_SC} = G_{pi,sc} \cdot G_{i_{SC}d_{SC}} \cdot H_{SC}$$

$$G_{cl\_SC} = \frac{G_{pi,sc} \cdot G_{i_{SC}d_{SC}} \cdot H_{SC}}{1 + G_{pi,sc} \cdot G_{i_{SC}d_{SC}} \cdot H_{SC}}$$

Where  $G_{ol\_SC}$  represents open loop transfer function,  $G_{cl\_SC}$  represents closed loop transfer function and  $H_{SC}$  represents feedback gain of SC current control loop. The compensated and uncompensated bode plots for open loop SC current control loop are as shown in Figure 5.8. The bode plot representing designed controller is stable for a given phase margin and gain margin.

#### 5.4.2 Design of battery current control loop

The battery current control loop small signal transfer functions are given in Table 5.4. The open loop transfer function of battery control  $G_{i_Bd_B}$  is used to determine control gains. In Table 5.4,  $K_{p\_b}$  and  $K_{i\_b}$  represent proportional and integral gains for battery control loop. The battery controller gains are calculated using phase margin of  $59.2^\circ$  and bandwidth of 1 kHz. By using MATLAB SISO toolbox control parameters are calculated to be  $k_{p\_b}=1.971$  and  $k_{i\_b}=7300$ .

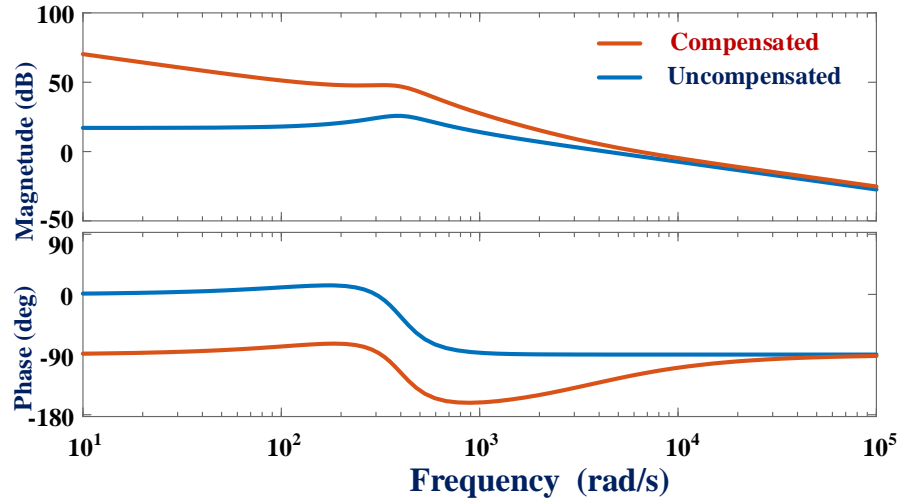


**Figure 5.9.** Open loop bode plot of battery current logic for with and without compensation

$$G_{ol\_B} = G_{pi,B} \cdot G_{i_B d_B} \cdot H_B$$

$$G_{cl\_B} = \frac{G_{pi,B} \cdot G_{i_B d_B}}{1 + G_{pi,B} \cdot G_{i_B d_B} \cdot H_B}$$

Where  $G_{ol\_B}$  represents open loop transfer function and  $H_B$  represents feedback gain for battery control loop. The compensated and uncompensated bode plots for open loop transfer functions are shown in Figure 5.9. Bode plot shows that designed control is stable for given phase margin and gain margin.

#### 5.4.3 Overall outer voltage control loop

Battery and SC current compensated values are required for design of voltage control loop. Bandwidth of 200 Hz and phase margin of  $60^\circ$  are selected for designing of outer voltage control loop. The proportional and integral gains for the outer voltage loop are obtained as  $K_{p,v} = 0.5054$  and  $K_{i,v} = 266$ . Open loop transfer function of outer voltage control loop is calculated as follows.

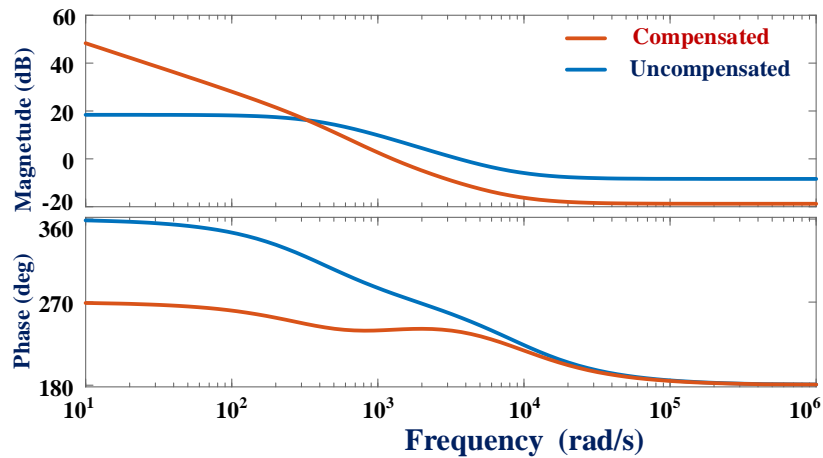


**Figure 5.10.** Open loop bode plot of outer voltage logic for with and without compensation

Stability of the system calculated by using  $G_{ol\_v_{DC}}$ . Where  $H_V$  represents feedback gain of voltage control loop. The open loop transfer function of voltage control system for compensated and uncompensated bode plot is shown in Figure 5.10. For the required phase margin and gain margin, the bode plot shows that system is stable for the given operating point.

## 5.5 Simulation Study and Discussion

In this segment, the results of the conventional and proposed control schemes are displayed for four test cases. The nominal parameters for simulation study are presented in Table 5.5. The entire model is implemented using MATLAB. The model consists of two bidirectional converters - one for battery and other for SC. The PV array is a unidirectional, which is connected to the boost converter. The four operating cases are presented in the following sections for step change in PV generation and load demand.

**Table 5.5** Nominal parameters for simulation study

S. No	Parameters	Value
1	MPPT Voltage ( $V_{mppt}$ )	32 V
2	MPPT Current ( $I_{mppt}$ )	3 A
3	MPPT Power ( $P_{mppt}$ )	96 W
3	SC Voltage ( $V_{sc}$ )	32 V
4	SC inductance ( $L_s$ )	0.355mH
5	Battery Voltage ( $V_B$ )	24 V
6	Battery inductance ( $L_B$ )	0.3mH
7	Boost inductance ( $L$ )	4.1mH
8	Resistance ( $R$ )	24 $\Omega$
9	DC grid voltage ( $V_{DC}$ )	48 V
10	Capacitance ( $C$ )	300 $\mu$ F

### 5.5.1 Case I: Step increase in PV generation

The simulation results for step change in PV generation, conventional and proposed control schemes are shown in Figure 4.14 and Figure 5.11 respectively. In both control schemes, due to atmospheric variations power produced by the PV panel increases from 96W to 192W at  $t=0.3$ sec. Due to this PV current increases from 3A to 6A at  $t=0.3$ sec. In this case load power requirement is constant at 96W. As PV power is more than the load power requirement, DC grid voltage increases more than 48V. Immediately SC absorbs excess

power of 96W in short duration until battery can regulate the grid voltage to 48V. Thus, the battery and SC charge according to energy management scheme to maintain the grid voltage constant at 48V. The simulation shows a settling time of 100ms for conventional control scheme and 35ms for proposed control scheme. The proposed control scheme has better dynamic performance and fast DC grid voltage regulation due to the utilization of uncompensated power from the battery system to improve the SC system.

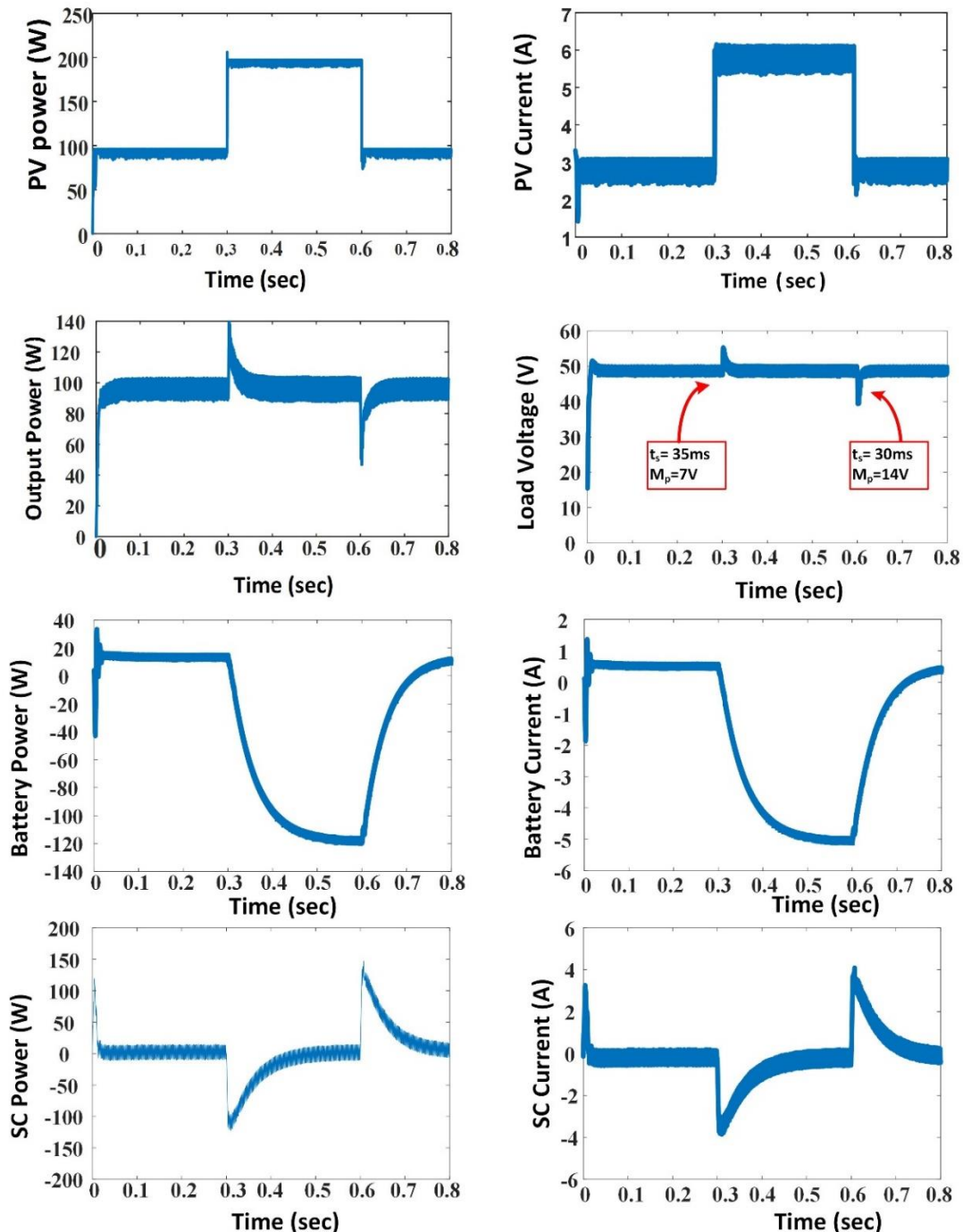


**Figure 5.11** Simulation results for step change in PV generation

### **5.5.2 Case II: Step decrease in PV generation**

Figure 4.14 and Figure 5.11 show the simulation results for a step decrease in PV generation for conventional and proposed control schemes respectively. In both control schemes, due to atmospheric variations power produced by the PV panel changes from 96W to 192W at  $t= 0.6\text{sec}$ . The step decrease in PV generation causes step decrease in PV current from 6A to 3A. The sudden decrease in PV generation causes decrease in DC grid voltage. The settling time for conventional and proposed schemes are 120 msec and 30msec respectively. Proposed control scheme is approximately 4 times faster compared to conventional control scheme. From the results, it can be observed that performance of proposed scheme is better compared to conventional control scheme.

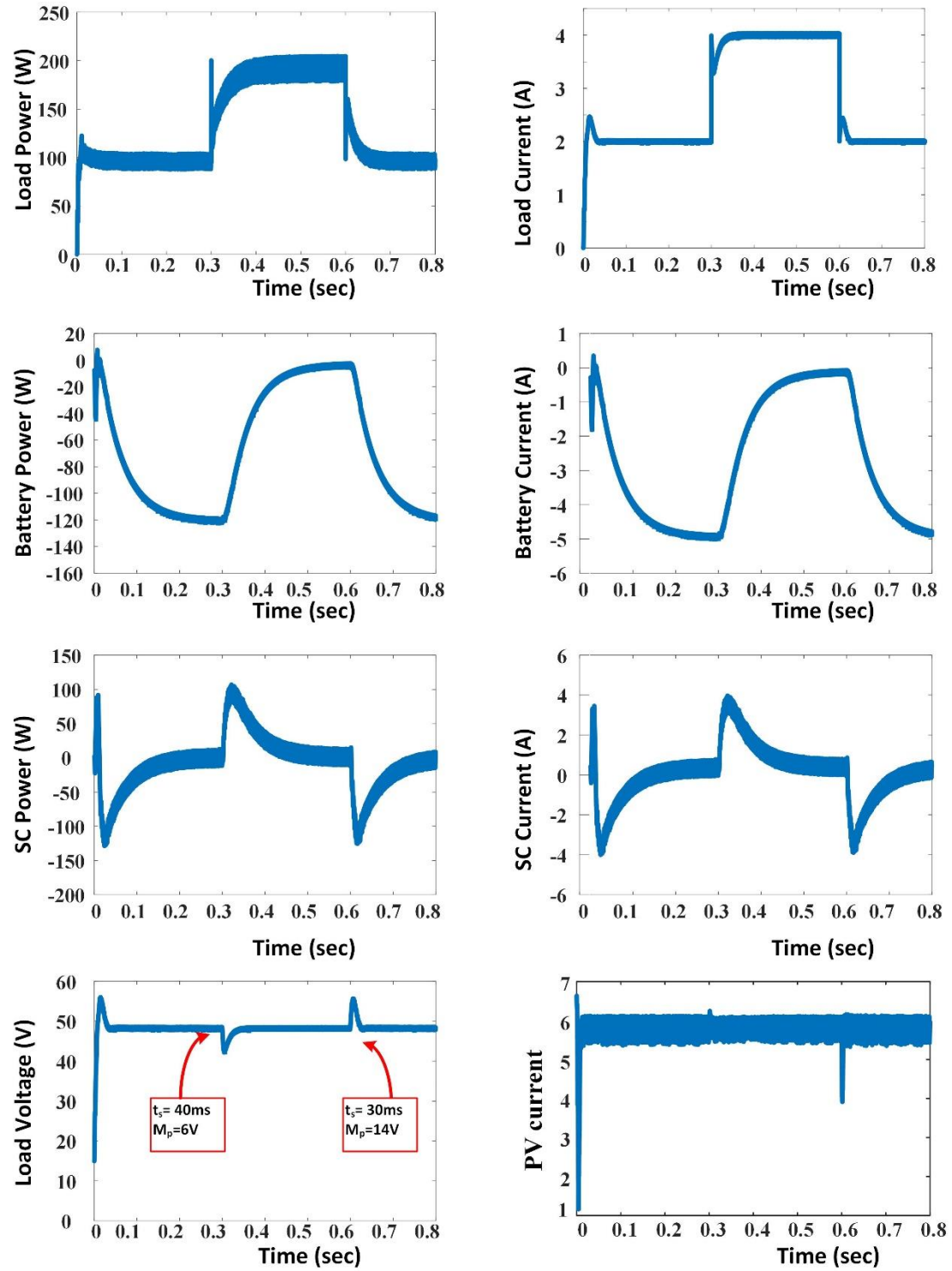
### **5.5.3 Case III: Step increase in load demand**

Figure 4.15 and Figure 5.12 show the Simulation results for a step increase in load demand for conventional and proposed control schemes respectively. At an instant  $t=0.3\text{sec}$  load demand increases from 96W to 192W. This increases the load current from 2A to 4A. During this case PV current is constant at 3A. Before  $t=0.3\text{sec}$ , the steady state values of  $V_{DC}=48\text{V}$ ,  $i_{PV}=3\text{A}$ ,  $i_o=2\text{A}$ . At  $t=0.3\text{sec}$ , the load demand increases to 192W, which is beyond the power range of PV generation. This creates a power imbalance between source power and load power. Immediately HESS responds, SC supply transient component of power demand and battery supplies steady state component of power demand. The DC grid voltage is regulated in 100msec in conventional control scheme and 40msec in proposed control scheme.

### **5.5.4 Case IV: Step decrease in load demand**

Figure 4.15 and 5.12 show the simulation results for a step decrease in load demand for conventional and proposed control schemes respectively. At  $t=0.3\text{sec}$ , load power demand decreases from 192W to 96W. This causes load current changes from 4A to 2A. The sudden change in load current affects the DC grid voltage. HESS responds immediately to these fluctuations to handle the excess power in the DC microgrid. The transient component of power handled is by the SC and average or steady state component of power is handled by the battery in both the control schemes. The times taken to restore the voltage, in conventional and proposed control scheme are 80msec and 30msec. From the results, it can

be seen that the proposed control scheme is faster with less peak overshoot DC grid voltage compared to conventional control scheme.



**Figure 5.12** Simulation results for step change in load demand

## 5.6 Experimental Results

The experimental setup developed for validation of proposed controller for two-input bidirectional converter as shown in Figure 5.13. The dSPACE-DS1104 digital controller board used in this work. The current sensor LA 55-P and voltage sensor LV 25-P are used for current and voltage measurements in the experimental validation. The regulated power supply (RPS) acts like PV emulator whose current controlled by boost converter. HESS is wired up using one unit of Exide Chloride 12V, 7 Ah lead-acid battery and Maxwell BMOD0058 16V, 58F supercapacitor. The bidirectional converter is connected using six MOSFET switches IRFP460.

The performance of DC microgrid supported by HESS is verified for different cases. 1) Step variation of PV generation 2) Step variation of load demand 3) Energy exchange mode. System implementation parameters for DC grid are given Table.5.6. DC microgrid is designed at a nominal value of 20 V.

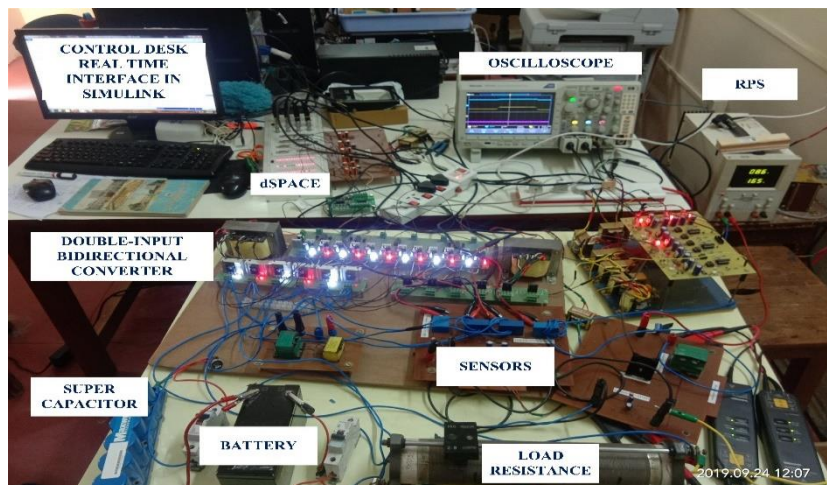


**Figure 5.13** Hardware prototype developed for HESS

**Table. 5.6:** DC microgrid implementation parameters

S. No	Parameters	Value
1	SC Voltage ( $V_{SC}$ )	10 V
2	SC inductance ( $L_S$ )	1.43mH
3	Battery Voltage( $V_B$ )	12 V
4	Battery inductance ( $L_B$ )	4.8mH
5	Boost inductance ( $L$ )	4.1mH
6	Resistance ( $R$ )	$25 \Omega$
7	DC grid voltage( $V_{DC}$ )	20 V
8	Capacitance ( $C$ )	$150 \mu F$

### 5.6.1 Step Change in PV generation

The experimental results for step change in PV generation waveforms are given in Figure 5.14. At time  $t_1$ , PV generation suddenly increases, this can be emulated by increasing PV current to 1A from 1.4A as shown in Figure 5.14(a). Than immediately HESS responds to store excess power in short duration of time, transient component of current charge SC until battery can regulate the DC grid voltage to 20V.

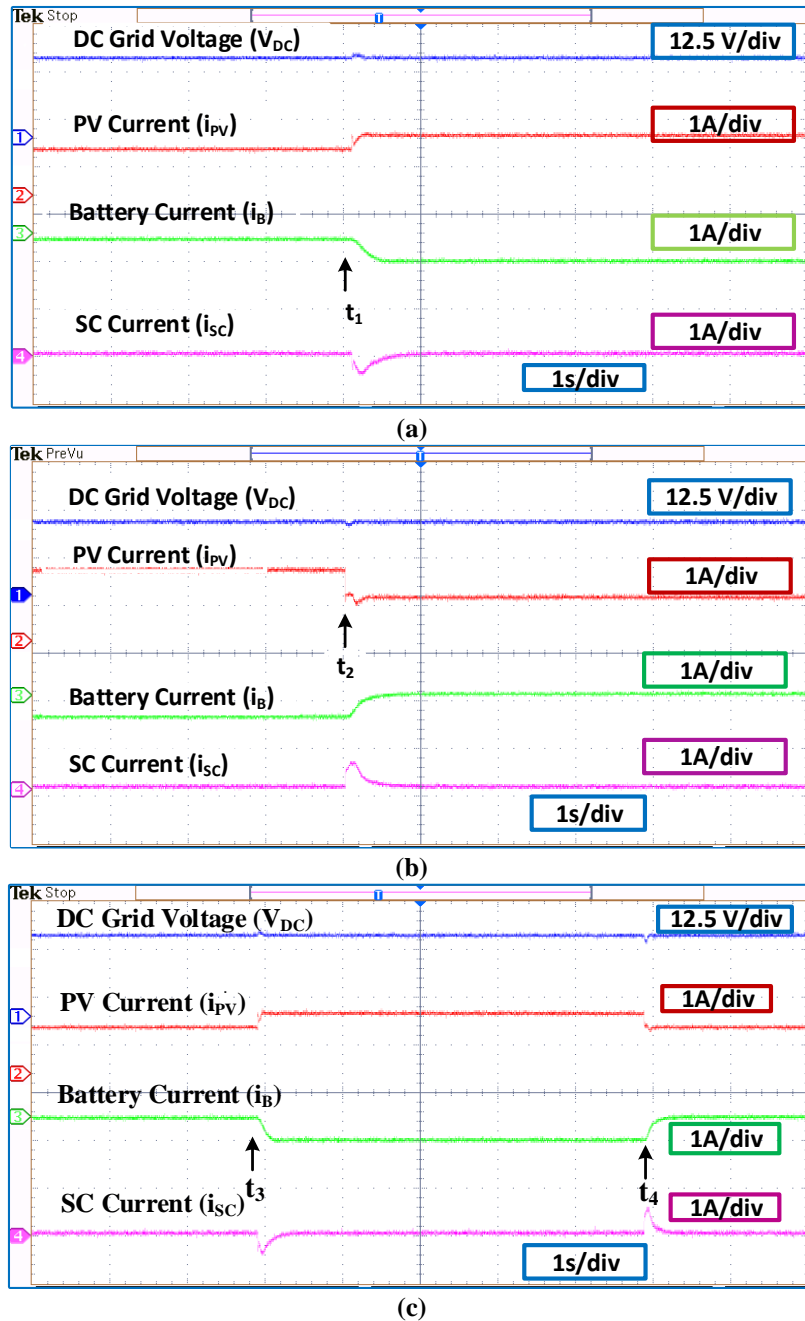


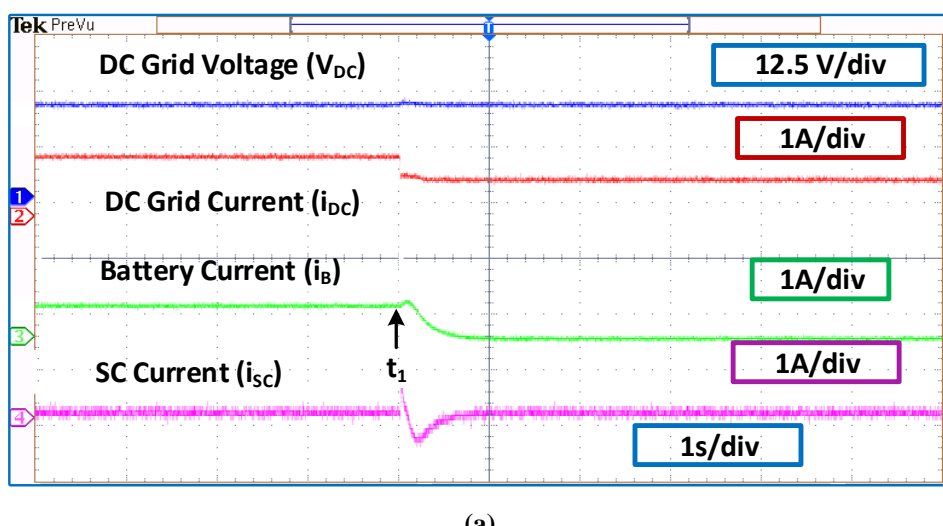
**Figure 5.14** Experimental results for step change in PV generation (a) step increase in PV generation (b) step decrease in PV generation (c) step increase and decrease in PV generation

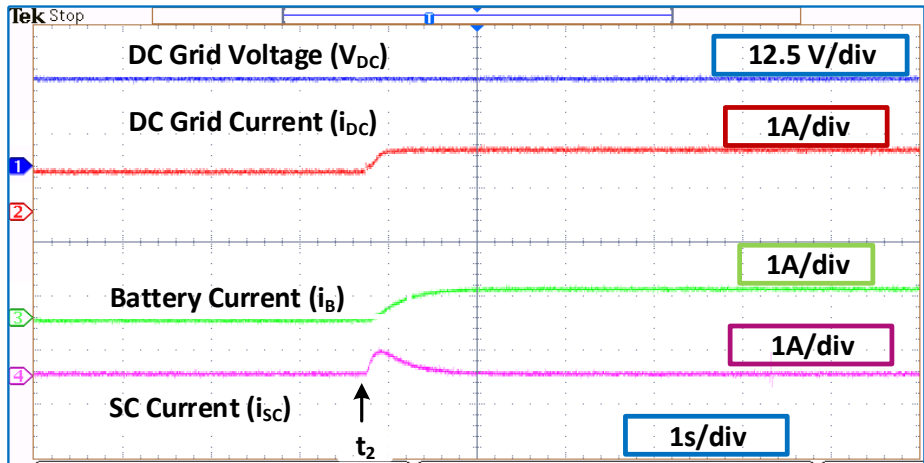
At time  $t_2$ , PV generation brought back to original condition as shown in Figure 5.14(b). Then immediately HESS responds such way that supplies deficient power in short duration of time. At time instants  $t_1$  and  $t_2$ , DC grid voltage is almost stable at 20V as shown in Figure 5.14(a) (b). Figure 5.14(c) shows the experimental results for sudden increase and decrease for PV generation at time  $t_3$  and  $t_4$  respectively. With the implementation of proposed control strategy better DC grid voltage regulation is achieved.

### 5.6.2 Step change in Load demand

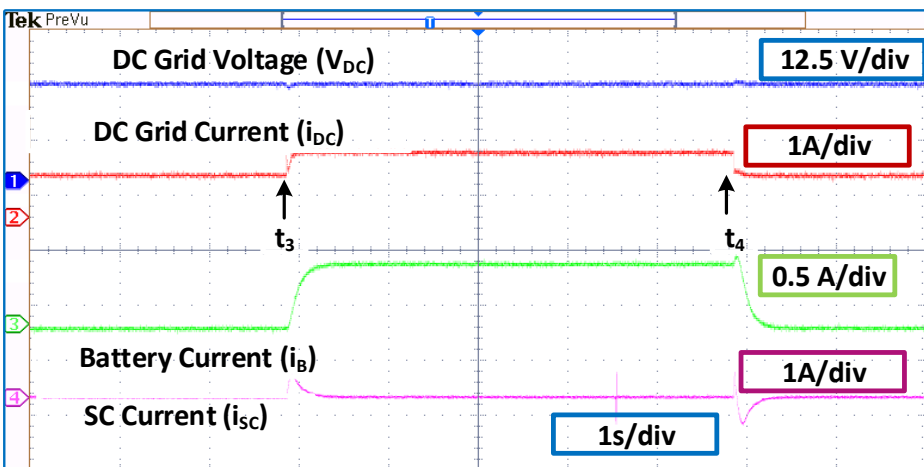
Experimental results for step change in load demand as shown in Figure 5.15. In this case  $i_{PV}$  is kept constant at 1.3A and RPS connected to the boost converter maintaining input voltage to 12V. Initially load resistance is  $20\Omega$  up to instant  $t_1$ . At time  $t_1$ , load resistance increased to  $35\Omega$  as result decrease in load demand as shown in Figure 5.15(a). The surge in grid voltage due to excess energy at DC microgrid. At that instant HESS stores excess energy at DC microgrid to maintain grid voltage constant at 20V. Transient component of current is charging SC and battery charging current is slowly increasing to steady state value.

The load resistance is brought back to original condition  $R=20\Omega$  at instant  $t_2$  as shown in Figure 5.15(b). As a result increase in load demand is analyzed. At instant  $t_2$ , small dip in DC grid voltage due to power mismatch between PV generation and load demand. The HESS supplies deficient power to maintain grid voltage constant by discharging battery and SC. Transient component of current met by SC and steady state component of current supplies battery can be shown by using current waveforms. The experimental study for both increase in load and decrease in load as shown in Figure 5.15(c). DC grid voltage is almost constant at 20V, small spikes due to fast dynamics of power semiconductor devices.





(b)



(c)

**Figure 5.15** Experimental results for step change in load demand (a) step increase in load demand (b) step decrease in load demand (c) step increase and decrease in load demand

### 5.6.3 Energy exchange Mode

In this mode, power flow from battery to SC is illustrated. Waveforms are shown in Figure 5.16. Initially HESS is disconnected from DC microgrid, due to the reduced PV generation grid voltage is 18V. At time instant  $t_1$ , HESS is connected to make DC grid voltage is 20V. The battery and SC current waveforms are shown in discharging mode. At  $t_2$ , SC SOC falls below 50%, which is taken as prescribed lower limit of SOC range, and HESS mode now shifts from HESS discharge mode to HESS Energy exchange mode. Now battery will charge SC. During energy exchange mode, HESS is disconnected from DC microgrid.

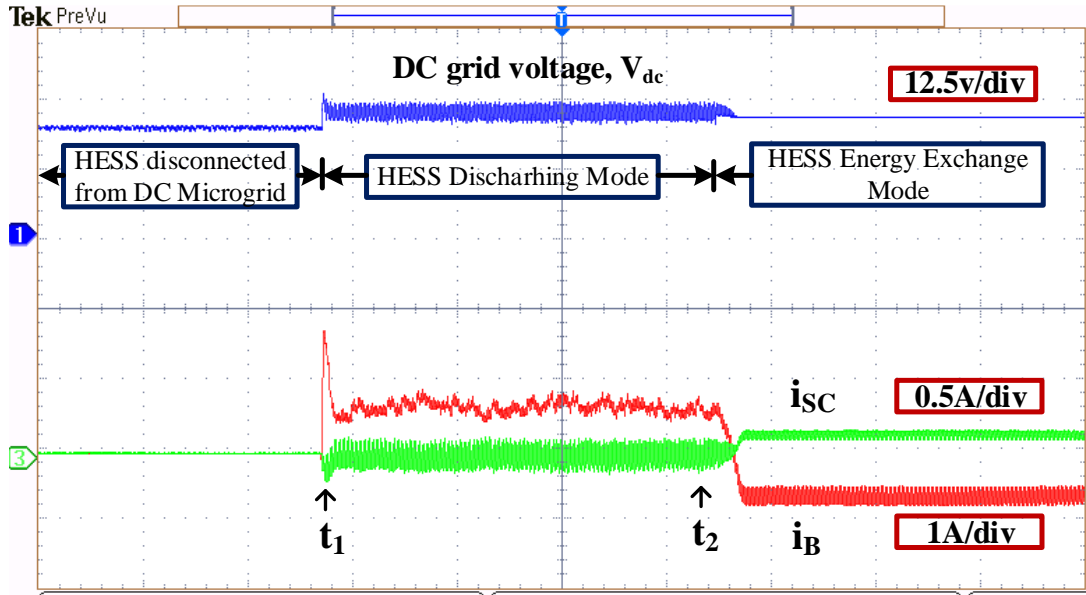


**Figure 5.16** Experimental results for HESS energy exchange mode. DC microgrid voltage ( $V_{DC}$ ), battery current ( $i_B$ ), SC current ( $i_{SC}$ ). Transition from discharge mode to energy exchange mode.

## 5.7 Comparative Performance evaluation

The performance of the proposed control scheme is evaluated in comparison to the conventional control scheme with step change in PV generation as well as load demand for the peak overshoot and settling time to restore grid voltage. During step variation of PV generation and load demand, the maximum peak overshoot can be calculated as follows.

$$\%MP = \frac{|V_{DC,ref} - V_{max}|}{V_{DC,ref}} \times 100$$

The comparative performance of conventional and proposed scheme is shown in Figure 5.17. It can be seen from the graphical representation that the proposed scheme is three times faster compared to conventional scheme. In the proposed control scheme, the maximum peak overshoot is also reduced in all four cases. Proposed control scheme is designed such that SC supports the HESS up to the time the battery reaches steady state condition. The proposed scheme offers faster DC grid regulation with robust operation.

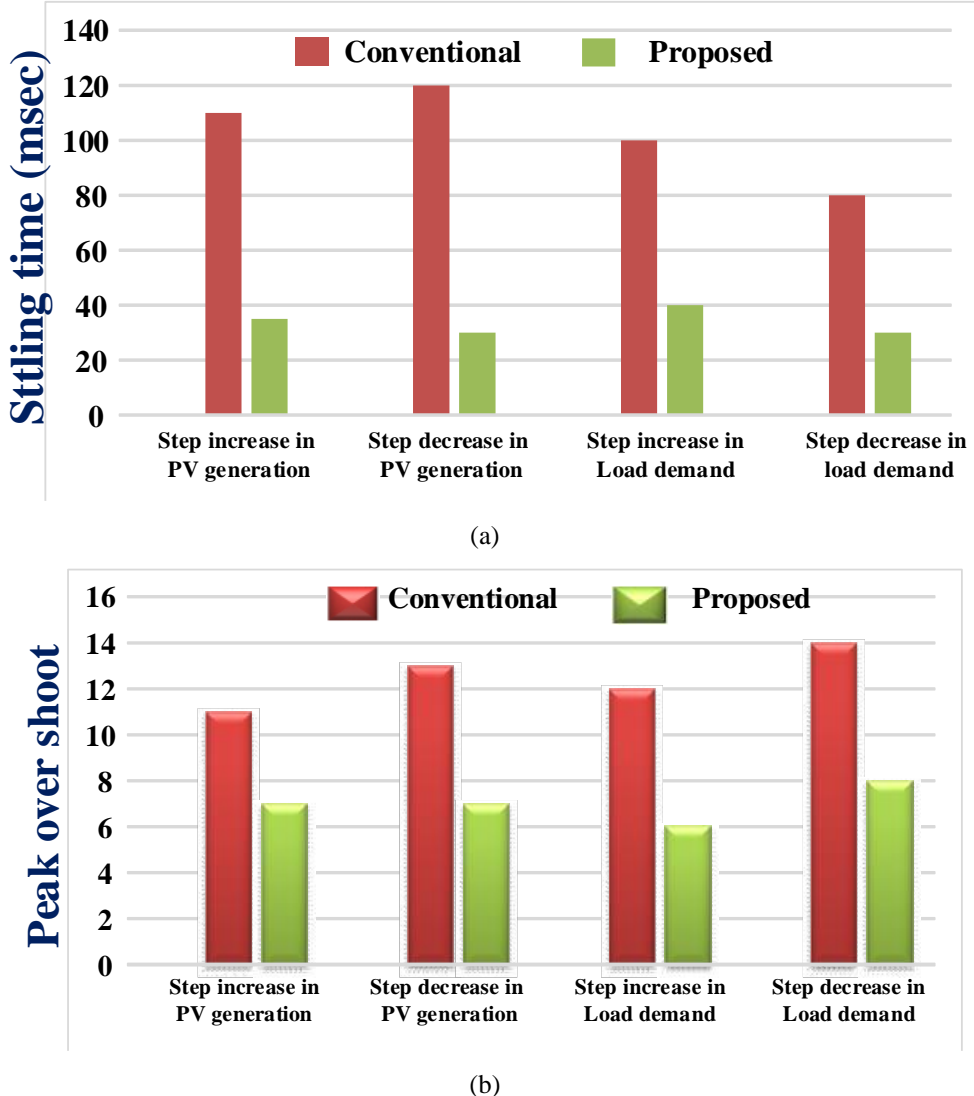


**Figure 5.17** Graphical comparative performance of proposed and conventional control scheme. (a) Settling time (b) Peak overshoot

## 5.8 Summary

The performance of controller design, HESS modelling, converter design and stabilization of DC microgrid against disturbances from PV generation as well as load variations are tested. The proposed system consists of PI controller, MIPC, DC sources and battery, and an SC based HESS. Battery current tracking error is observed in conventional control strategy. The error due to battery current controller slows battery response. To address aforementioned issues, a proposed control strategy was developed, which provides fast DC grid voltage regulation compared with conventional control strategy. It utilizes battery error current to overcome slow dynamics of battery system. It decreases stress on battery and increases battery lifetime. Moreover, decoupled, separate and independent

control of battery and SC power was achieved as well as power flow between them. Low power experimental setup is developed for two input bidirectional converter for step change in PV generation and load demand. This system can be applied in hybrid electric vehicles where more than two sources can supply power to the motor.

# **Chapter-6**

**A Comparative Analysis of PI and Predictive  
Control Strategy for HESS Based Bi-Directional  
DC-DC Converter for DC Microgrid Applications**

# Chapter-6

## A Comparative Analysis of PI and Predictive Control Strategy for HESS Based Bi-Directional DC-DC Converter for DC Microgrid Applications

### 6.1 Introduction

The use PI controllers for HESS has drawbacks such as controller parameter tuning is difficult and the additional filters are required to share the high and low frequency power fluctuations. For controlling power electronics converters, the MPC method is widely used.

This work proposes a model predictive control (MPC) based method to control two-input bidirectional DC-DC converter for HESS in DC microgrid applications. For more than two decades, the MPC approach has been used in industrial process control applications. Many power electronics applications, such as boost converters [116,117,118], bi-directional DC-DC converters [119] and single inductor based multi-port converters [120] have been used the MPC method in the last decade.

There are few works implemented for DC microgrid using MPC control scheme. The MPC is a new technique that predicts the future states of a system using a discrete model of the system and present state of the system, to get optimal control action to be performed at every sampling instant. In this work, an MPC control scheme is proposed for a multiple-input bidirectional DC-DC converter of HESS in DC grid voltage regulation, battery charge discharge rate control and power splitting between battery and SC. The proposed work has following objectives

1. Less computational complexity.
2. Simple two-loop control structure with outer voltage loop generating dynamic references and inner current control loop for references splitting without low pass filters and reference tracking with MPC concepts.
3. Better dynamic performance and reduction in DC grid voltage variation compared to the conventional PI control method.

## 6.2 MPC Control Strategy

In order to control the DC grid voltage stabilization, the control structure includes two layers of control: outer voltage control and inner current control. The purpose of the outer voltage control loop is to calculate dynamic reference current supplied by HESS for DC grid voltage regulation. The power management algorithm which splits the reference current ensuring reduction in battery discharge rate and power balance between the load and PV generation. The prediction of battery and SC inductor currents from a discrete model of DC-DC converter and generation of modelling signals that ensures the least error between predicted and reference values. The block diagram representation of MPC control scheme as shown in Figure 6.1.

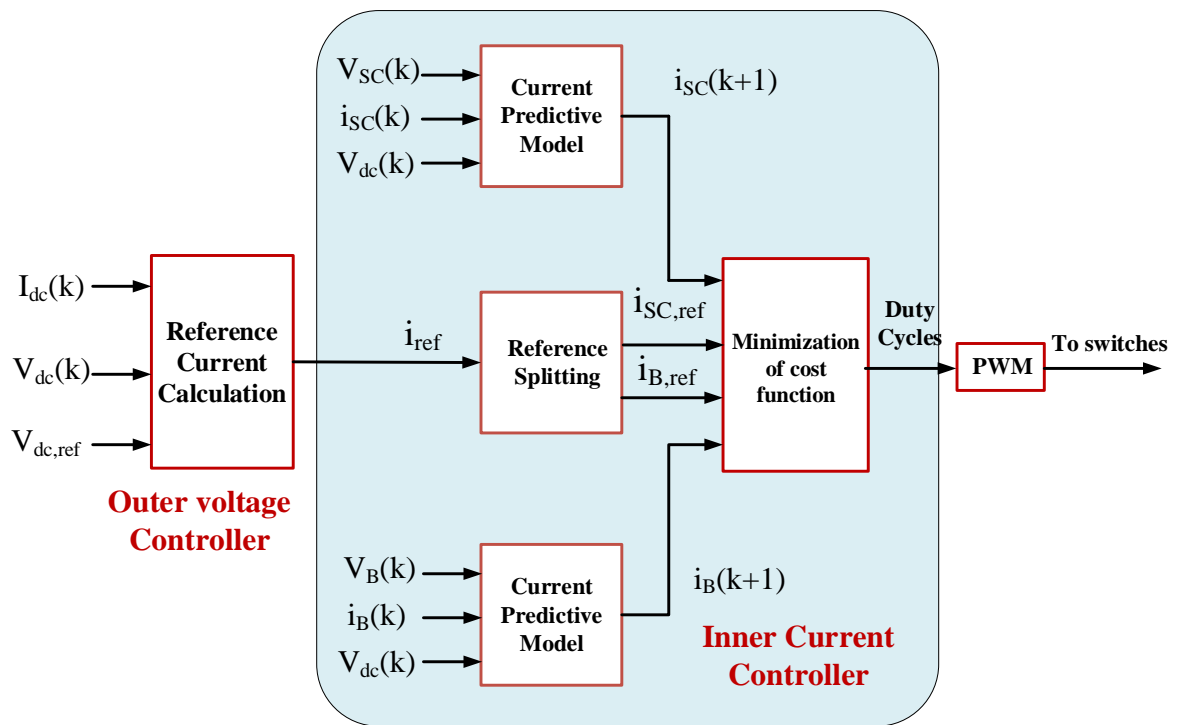


Figure 6.1 Block diagram representation of MPC for HESS

### 6.2.1 Outer voltage control loop

The current through the DC link capacitor is given by the formula the variation of DC grid voltage will directly affect the charging current ( $i_c$ )

$$i_c = C \frac{dV_{dc}}{dt} \quad (6.1)$$

By using Euler's difference law, the above equation can be expanded with small sampling period

$$i_c(k) = C \times \frac{V_{dc}(k) - V_{dc}(k-1)}{T_s} \quad (6.2)$$

Where  $T_s$  denotes the sampling period,  $V_{dc}(k)$  denotes the present sampling DC grid voltage and  $V_{dc}(k-1)$  denotes the previous sampled DC grid voltage.

$$i_c(k+1) = C \times \frac{V_{dc}(k+1) - V_{dc}(k)}{T_s} \quad (6.3)$$

For  $V_{dc}(k+1)$  to be  $V_{ref}$ , the calculation of  $i_c(k+1)$  value from the above equation will be large initially to limit this value an integer coefficient  $N$  as a prediction horizon [121] is introduced such that

$$i_c(k+1) = C \times \frac{V_{ref} - V_{dc}(k)}{N \cdot T_s} \quad (6.4)$$

The total reference current to be supplied by the HESS for DC grid voltage regulation is given by

$$i_{ref}(k+1) = i_c(k+1) + i_{dc}(k) \quad (6.5)$$

Where  $i_{dc}(k)$  is the total load current

### 6.2.2 Inner current control

For prediction of battery and SC inductor currents an averaged voltage balance equation across these inductors is developed, for  $L_b$

$$L_b \frac{di_b}{dt} = V_b d_b - V_{dc}(1 - d_b) \quad (6.6)$$

By using Euler's difference law

$$L_b \frac{i_b(k+1) - i_b(k)}{T_s} = V_b(k) d_b(i) - V_{dc}(k)(1 - d_b(i)) \quad (6.7)$$

The above equation  $i_b(k+1)$  is calculated

$$i_b(k+1) = \frac{T_s}{L_b} \times [V_b(k) d_b(i) - V_{dc}(k)(1 - d_b(i))] + i_b(k) \quad (6.8)$$

Similarly, the SC inductor current model is derived as follows

$$L_{sc} \frac{di_{sc}}{dt} = V_{sc} d_{sc} - V_{dc}(1 - d_{sc}) \quad (6.9)$$

From the above equation  $i_{sc}(k + 1)$  is derived as

$$i_{sc}(k + 1) = \frac{T_s}{L_{sc}} \times [V_{sc}(k)d_{sc}(i) - V_{dc}(k)(1 - d_b(i))] + i_{sc}(k) \quad (6.10)$$

The cost functions for battery and SC current control are

$$J_b = ((i_{bref} - i_b(k + 1))^2 \quad (6.11)$$

$$J_{sc} = ((i_{scref} - i_{sc}(k + 1))^2 \quad (6.12)$$

Using  $i_b(k + 1)$  and  $i_{sc}(k + 1)$  equations calculated iteratively for duty cycles  $d_b$  and  $d_{sc}$  from 0 to 1 with an increment of 0.01 and each of this value compared with  $i_{bref}$  and  $i_{scref}$  during every sampling interval and the duty cycle which gives the least cost function value is selected.

### 6.3 Simulation Study and Discussion

In this segment, the results for the proposed MPC control schemes are displayed for two test cases. The nominal parameters for simulation study are presented in Table.6.1. The entire model is implemented using MATLAB. The model consists of two bidirectional converters - one for battery and other for SC. The PV array is a unidirectional, which is connected to the boost converter. The two operating cases are presented in the following sections for step change in PV generation and load demand.

**Table 6.1** Nominal parameters for simulation study

S. No	Parameters	Value
1	MPPT Voltage ( $V_{mppt}$ )	32 V
2	MPPT Current ( $I_{mppt}$ )	3 A
3	MPPT Power ( $P_{mppt}$ )	96 W
3	SC Voltage ( $V_{sc}$ )	32 V
4	SC inductance ( $L_s$ )	0.355mH
5	Battery Voltage( $V_B$ )	24 V
6	Battery inductance ( $L_B$ )	0.3mH
7	Boost inductance (L)	4.1mH
8	Resistance (R)	24 $\Omega$
9	DC grid voltage( $V_{DC}$ )	48 V
10	Capacitance (C)	300 $\mu$ F

### 6.3.1 Case-I step change in PV generation

A step change in PV current is examined in this case. The peak overshoot ( $M_p$ ), settling time ( $t_{ss}$ ) of DC grid voltage during a step change in PV generation was examined. The load demand is kept constant in this case, by keeping  $R_{dc}=24 \Omega$ . By changing the PV current control reference, a step change in PV generation is applied to the steady state system.

The simulation results for a step increase and decrease in PV generation are represented in Figure 6.2. Due to the atmosphere variations power produced by the PV panel increases to 192W from 96W at  $t= 0.2$ sec and back to 96W at  $t=0.6$ sec. As PV power is more than the load power requirements, grid voltage increases beyond 48V. The SC absorbs the excess power of 96W in short duration and until battery can regulate the grid voltage to 48V

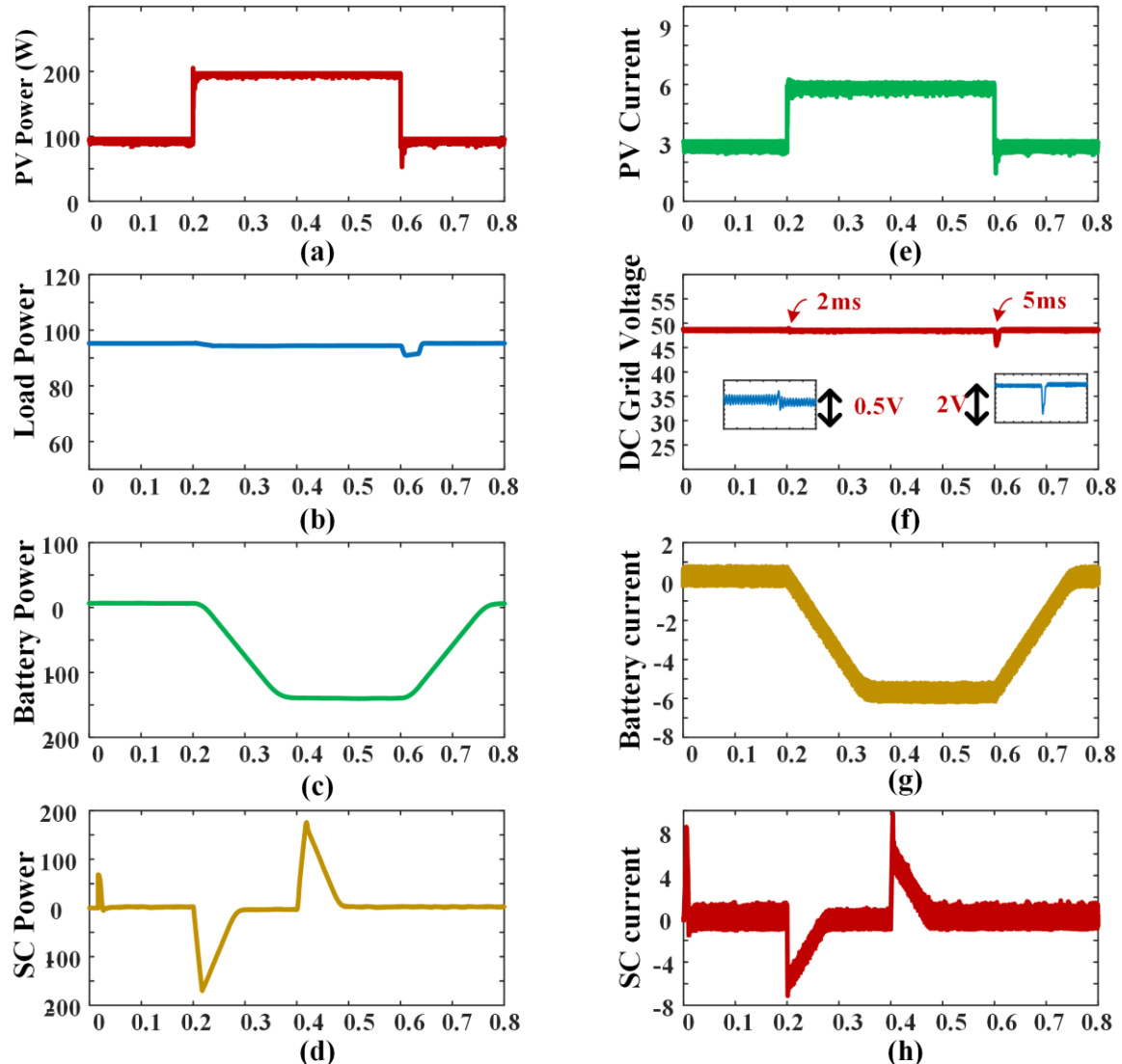
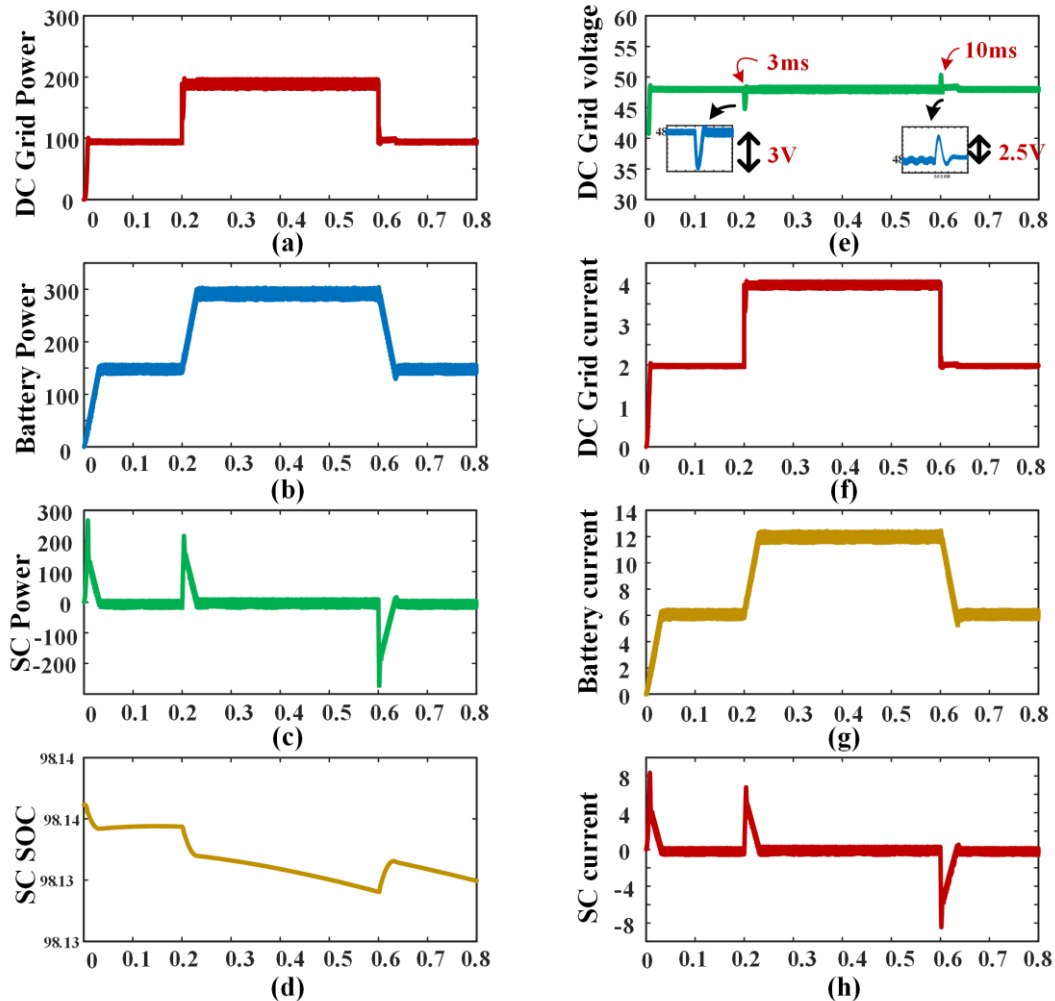


Figure 6.2 Simulation results for step change in PV generation

In this cases, transient current component handled by the SC and steady state current component supplied by the battery system. As PV generation increases or decreases, the change in DC bus voltage ( $\Delta V_{DC}$ ) are 0.5 V and 2V, respectively. The corresponding %MP values are 1.04% and 4.1% respectively. Step increases and decreases in PV generation have settling time ( $t_{ss}$ ) of 2ms and 5msec, respectively.

### 6.3.2 Case-II Step change in load demand

The power developed by the PV panel is 96W in maximum power region. To absorb this PV power, a load resistance of  $24 \Omega$  connected to 48V DC microgrid. For consuming entire power from the PV panel, load requires 2A current at steady state. At  $t=0.2$ sec, load demand increases from 96W to 192W and bring back to 96W at  $t=0.6$ sec as shown in Figure 6.3, which is beyond the power range of PV panel. This creates a power imbalance between PV generation and load demand.



**Figure 6.3** Simulation results for step change in load demand

Immediately HESS responds, SC supply transient component of power and battery supplies steady state component of power demand. As load demand increases or decreases, the change in DC bus voltage ( $\Delta V_{DC}$ ) are 3 V and 2.5 V, respectively. The corresponding %MP values are 6.25% and 5.2% respectively. Step increases and decreases in load demand have settling time ( $t_{ss}$ ) of 3ms and 10msec, respectively.

## 6.4 Experimental Results

A low power scaled down experimental results are used to validate the proposed MPC control strategy as shown in Figure 6.4. A dSPACE-DS1104 digital controller used in this work. The current sensor LA 55-P and voltage sensor LV 25-P are used for current and voltage measurements in experimental validation. The regulated power supply (RPS) acts like PV emulator whose current controlled by boost converter. HESS is wired up using a single unit each of Exide Chloride Safe power 12 V, 7 Ah lead-acid battery and Maxwell BMOD0058 16 V, 58 F supercapacitor. The double-input bidirectional converter is built using six MOSFET switches IRF540N.

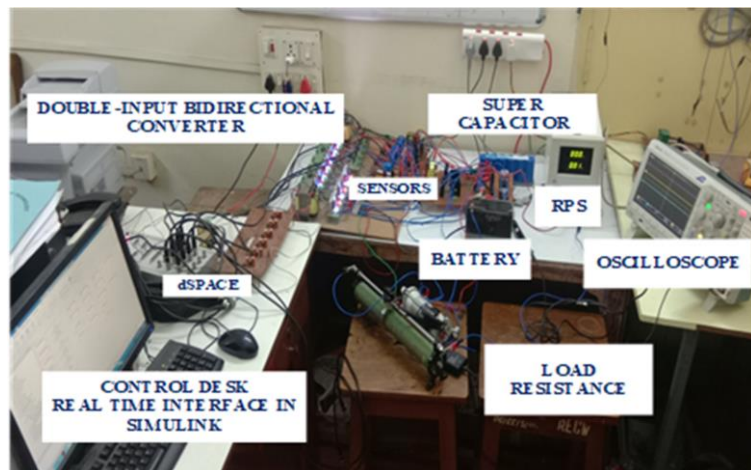


Figure 6.4 Hardware prototype developed for HESS

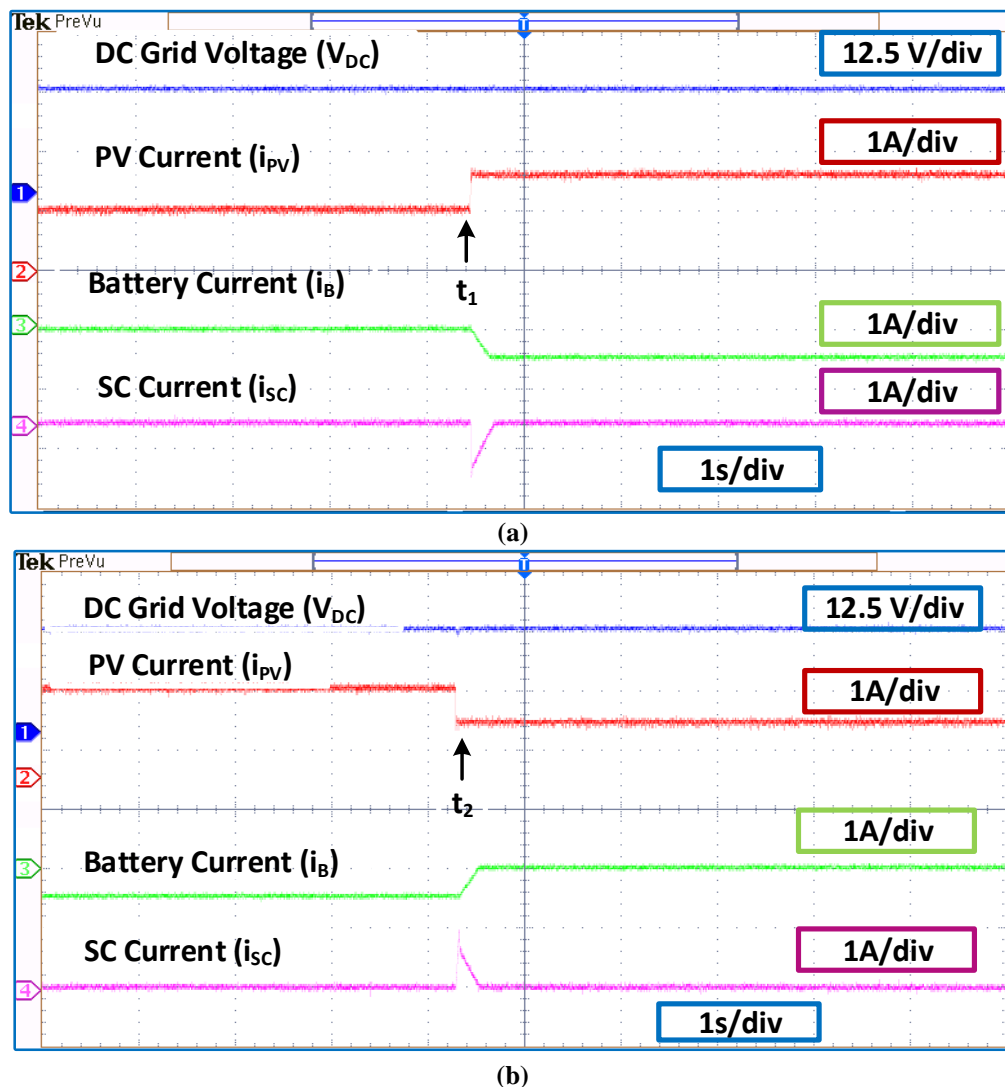
Table 6.2: DC microgrid implementation parameters

S. No	Parameters	Value
1	SC Voltage ( $V_{sc}$ )	10 V
2	SC inductance ( $L_s$ )	1.43mH
3	Battery Voltage( $V_B$ )	12 V
4	Battery inductance ( $L_B$ )	4.8mH
5	Boost inductance ( $L$ )	4.1mH
6	Resistance ( $R$ )	$25 \Omega$
7	DC grid voltage( $V_{DC}$ )	20 V
8	Capacitance ( $C$ )	$150 \mu F$

The performance of DC microgrid, powered by emulated PV source, supported by HESS is verified for, i.e., 1) Step change in PV generation, 2) Step change in load demand. DC grid specifications are given in Table 6.2. DC microgrid is setup at a nominal voltage of 20 V.

#### 6.4.1 Case-I step change in PV generation

The experimental results for step change in PV generation as shown in Figure 6.5. In this case, the load power demand is kept constant. The step increase in PV generation is applied to the steady state system by changing PV current from 1A to 1.5A at  $t=t_1$  as shown in Figure 6.5(a). At instant  $t_2$ , PV current is decreased from 1.5A to 1A as shown in Figure 6.5(b). The experimental results for step increase and decrease in PV generation as shown in Figure 6.5(c). In all the cases, the high frequency component of power demand handled by the SC system and steady state component power handled by the battery system to maintain the DC grid voltage regulated quickly.



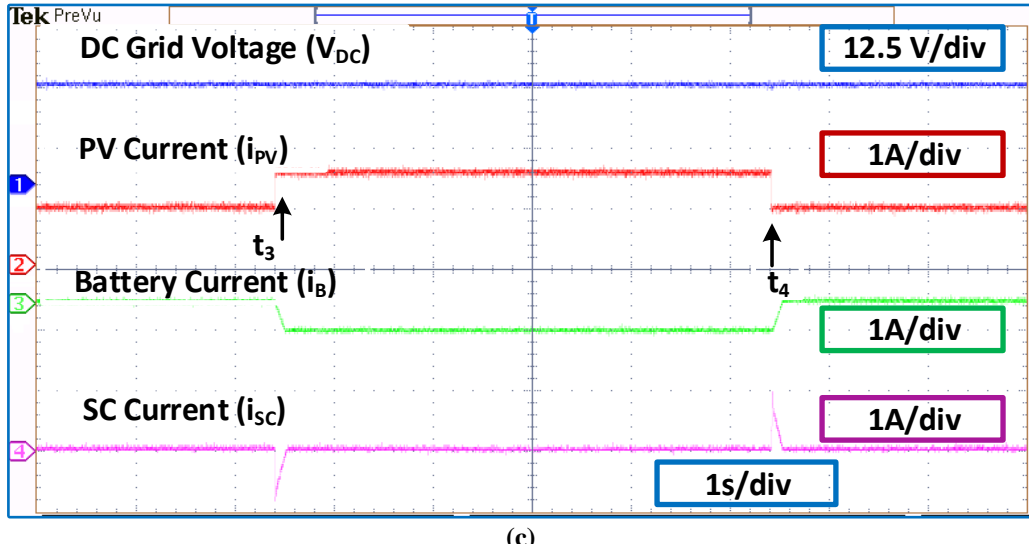
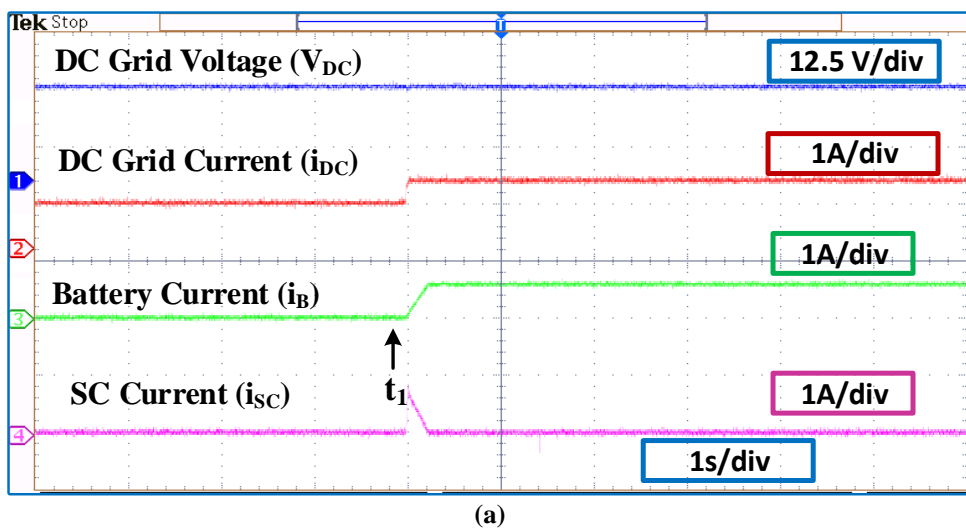


Figure 6.5 Experimental results for step change in PV generation (a) step increase in PV generation (b) step decrease in PV generation (c) step increase and decrease in PV generation.

#### 6.4.2 Case-II Step change in load demand

The experimental results for step change in load demand as shown in Figure 6.6. The PV generation is kept constant during step change in load demand. The load resistance decreased from  $25\Omega$  to  $16\Omega$  which increases the load current from  $0.8A$  to  $1.25A$  at  $t=t_1$  as shown in Figure 6.6 (a). At instant  $t_2$ , the load resistance brought back to original value as shown in Figure 6.6(b). The experimental results for step increase and decrease of load demand as shown in Figure 6.6(c). Due to sudden change in load demand, this creates power imbalance between PV generation and load demand. Immediately HESS responds, SC supply transient power demand and battery supplies steady state component of power demand to maintain the DC grid voltage stable.



(a)

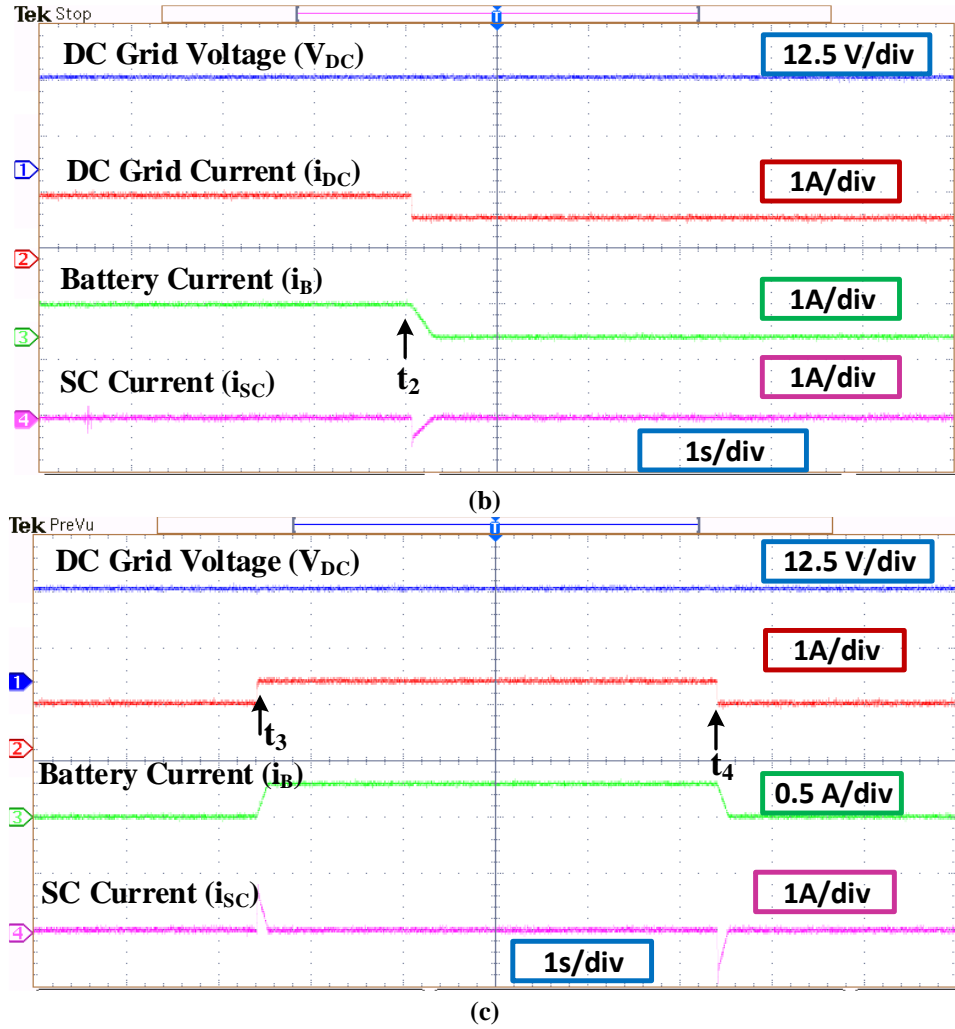


**Figure 6.6** Experimental results for step change in load demand (a) step increase in load demand (b) step decrease in load demand (c) step increase and decrease in load demand.

## 6.5 Comparative performance evaluation

The performance evaluation of MPC scheme over PI control scheme with step change in PV generation and load demand for peak overshoot and settling time to restore grid voltage. The graphical results representation of MPC over PI control schemes are presented in Figure 6.7 and Figure 6.8. The proposed MPC scheme provides lesser overshoot, undershoot and faster regulation with less settling time. Figure 6.7 (a) and Figure 6.7 (b) shows the DC grid voltage variation with step change in PV generation and load demand. Figure 6.7 (c) and Figure 6.7 (d) shows the battery and SC current response with MPC over PI control strategies. In Figure 6.7 (d), we can see that the SC current is faster and higher compared to PI control methods. Hence, SC utilization is faster and higher compared to PI methods. From the results, the performance of MPC control method is better in terms of DC grid voltage regulation and SC utilization.

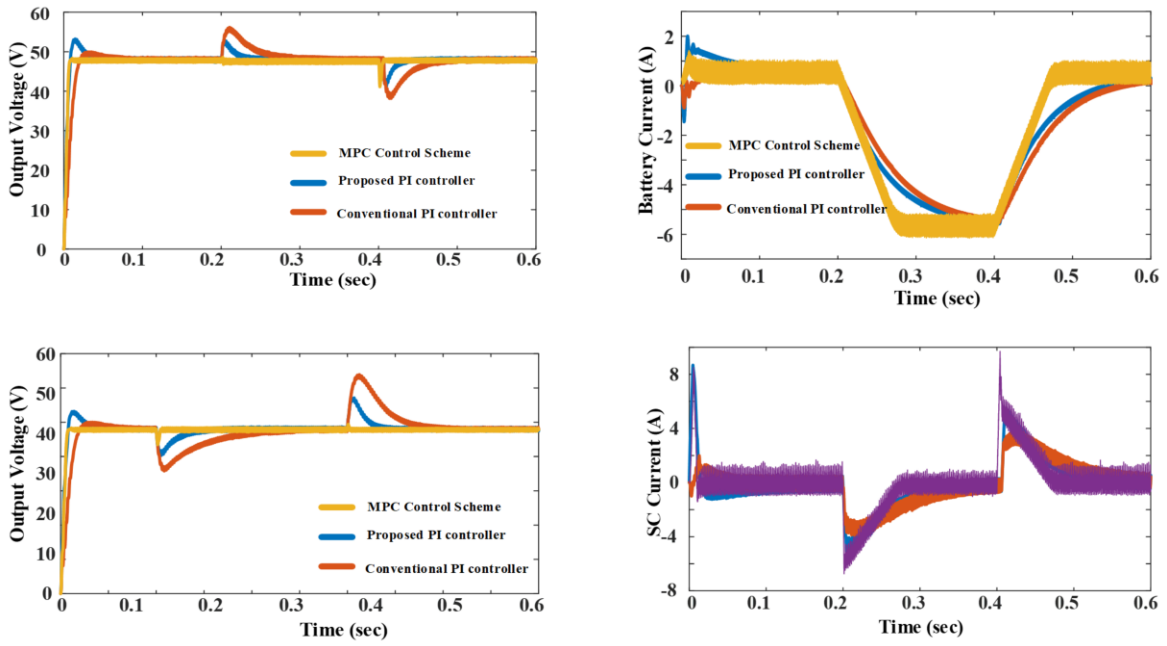


**Figure 6.7** Comparative analysis of MPC over PI control methods (a) Step change in PV generation (b) Step change in load demand (c) battery current (d) SC current

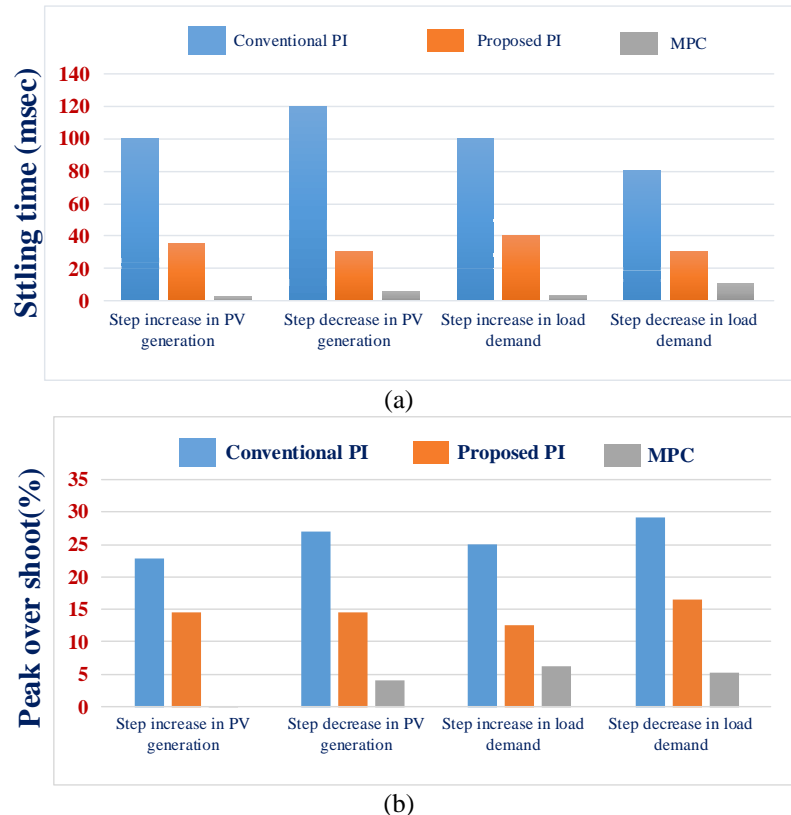


**Figure 6.8** Graphical comparative performance of MPC over conventional PI control scheme (a) Settling time (b) Peak overshoot

## 6.6 Summary

The implementation of proposed MPC for the HESS in DC microgrid applications has been presented in this chapter. As traditional PI-control methods have tuning complications, dependency on operating point and optimal performance cannot be achieved. Hence, to overcome these issues we proposed an MPC based control strategy with comparatively lower complexity to other MPC based methods that are employed for DC-DC converters. The proposed power management scheme designed and proven by comparing it with the conventional PI method by simulation and experimental analysis.

Experimental results for MPC control method performed for different test cases such as (i) step change in PV generation (ii) step change in load demand. The results validate that proposed MPC power management scheme monitors and control the HESS for DC microgrid effectively with lower DC grid voltage variation and better battery charge/discharge control rate without low pass filters for reliable operation.

# **Chapter-7**

## **Conclusion**

# Chapter-7

## Conclusion

### 7.1 General Overview

In this thesis, various converters and control strategies have been designed, discussed with simulation and experimental validation. The main objective of control methods is to enhance the HESS response with less computational complexity. The proposed power management schemes' effectiveness is proven by comparing with conventional methods. The proposed control methods can be implemented for HESS in DC microgrids, AC microgrids, EVs and UPS applications.

### 7.2 Summary of Important Findings

#### i. Optimum design and analysis of a dynamic energy management scheme for HESS in renewable power generation applications

A novel control strategy for a HESS is discussed in detail. In the proposed system, the battery is utilized to stabilize the moderate changing of power surges, whereas the supercapacitor is utilized to stabilize the rapidly changing of power surges. A two-loop proportional-integral controller is designed for the closed-loop operation of HESS. The source power and load power is not balanced because of the fluctuating conditions of PV power generation and load demand. This power imbalance causes fluctuations in DC grid voltage. The DC bus voltage variations are mitigated using HESS, which is connected to DC grid through bi-directional DC-DC converter to enable the bidirectional power flow between energy storage devices and the DC bus. To enhance the life span and to reduce the current stress on the battery, the proposed method is employed with charge/discharge rate control feature. The proposed control procedure is realized in MATLAB/Simulink and the results are presented for different case studies. Experimental results are obtained for a two-input bi-directional converter at the sudden change in PV generation and load demand with the proposed controller. The proposed control strategy is effective for maintaining constant DC microgrid voltage under source and load fluctuations.

ii. **Modelling of a Double-Input Bidirectional DC-DC Converter for HESS and Unified Controller Design for DC Microgrid Applications**

Due to high penetration of renewable energy sources in dc microgrids, these microgrids are highly susceptible to fluctuations in power generation. To absorb these fluctuations within, a HESS consisting of battery and supercapacitor is used. The contrasting characteristics of battery and supercapacitors make them a perfect combination for HESS applications. The HESS is interfaced to DC microgrid using a double-input bidirectional converter. This bidirectional converter not only provide decoupled control of battery and supercapacitor power but also provide energy exchange between the storage components within. This work presents a converter modeling method for double-input bidirectional converter. A controller was designed based on this for voltage regulation application for a DC microgrid. The modified operation of converter made it possible to use same controller for both HESS charging/discharging operation thus making it a unified controller. The controller was designed to provide improved DC link voltage restoration to PV generation and load interruptions, as well as effective power balance between the battery and the SC.

iii. **Modelling, Analysis and Control of a Two-Input Bidirectional DC-DC Converter for HESS in DC Microgrid Applications**

The proposed advanced controller designed for multi input bidirectional DC-DC Power Converter for HESS. In the proposed control scheme, uncompensated power from the battery system is utilized to improve the SC system. This approach reduces the current stresses, increases the life cycle of the battery and improves the overall system performance to the step change in PV generation and load demand, and provides faster DC grid voltage regulation.

iv. **A Comparative Analysis of PI and Predictive Control Strategy for HESS Based Bi- Directional DC-DC Converter for DC Microgrid Applications**

The traditional PI controller for a HESS has drawbacks such as difficult tuning of the controller parameters and the additional filters to allocate high and low frequency power fluctuations. In this work proposed a MPC method to control two-input bidirectional DC-DC converters for HESS in a DC microgrid applications. MPC uses the current state of system and considers the effect of present control and action of

future outputs. MPC controllers solves the optimization problem at each sampling interval. MPC controller provides the effective power sharing between battery and SCs in such a way that regulates the grid voltage as quick as possible.

**Table 7.1** Comparative performance of various control methods

	Conventional PI		Proposed PI		MPC	
	Settling Time (t <sub>ss</sub> )	%MP	Settling Time (t <sub>ss</sub> )	%MP	Settling Time (t <sub>ss</sub> )	%MP
Step increase in PV generation	100msec	22.9%	35msec	14.58%	2msec	0.01%
Step decrease in PV generation	120msec	27%	30msec	14.5%	5msec	4.1%
Step increase in load demand	100msec	25%	40msec	12.5%	3msec	6.25%
Step decrease in load demand	80msec	29.16%	30msec	16.6%	10msec	5.2%

The simulation comparison between the conventional over proposed MPC methods are tabulated in Table 7.1. From the results, the MPC control method provides faster response compared to PI control method.

### 7.3 Future Scope

Any research never ends without leaving an open window for further research. The following aspects may be looked at by future researchers:

- The MPC method for grid-connected operation of HESS service is a suggested research area.
- The application of the MPC approach to hybrid AC/DC microgrid is another suggested research area.

## References

- [1] M. S. Whittingham. History, evolution, and future status of energy storage. *Proceedings of the IEEE*, 100 (Special Centennial Issue): 1518-1534, May 2012.
- [2] S. Chu and A. Majumdar. Opportunities and challenges for a sustainable energy future. *nature*, 488(7411):294, Aug 2012.
- [3] Enerdata. Global energy statistical yearbook 2018. [Online; 7.December 2018].
- [4] C. Klessmann, A. Held, and M. Rathmann, and M. Ragwitz. Status and perspectives of renewable energy policy and deployment in the European union-what is needed to reach the 2020 targets? *Energy policy*, 39(12):7637-7657, Dec 2011.
- [5] M.J. Barradale. Impact of public policy uncertainty on renewable energy investment: Wind power and the production tax credit. *Energy policy*, 38(12): 7698-7709, Dec 2010.
- [6] A.E. Jones, M. Irwin and A. Izadian, "Incentives for microgeneration development in the U.S. and Europe," IECON 2010 - 36th Annual Conference on *IEEE Industrial Electronics Society*, Glendale, AZ, USA, 2010, pp. 3018-3021, doi: 10.1109/IECON.2010.5674952.
- [7] K. Malmedal, B. Kroposki, and P. K. Sen, "Energy Policy Act of 2005 and Its Impact on Renewable Energy Applications in USA," 2007 *IEEE Power Engineering Society General Meeting*, Tampa, FL, USA, 2007, pp. 1-8, doi: 10.1109/PES.2007.386060.
- [8] J. Wu and Chou, "A Solar Power Generation System With a Seven-Level Inverter," in *IEEE Transactions on Power Electronics*, vol. 29, no. 7, pp. 3454-3462, July 2014, doi: 10.1109/TPEL.2013.2279880.
- [9] J.C. Wu, K. D. Wu, H. L. Jou, and S.K. Chang. Small-capacity grid-connected solar power generation system. *IET Power Electronics*, 7(11):2717-2725, July 2014.
- [10] G. J. Shirek and B. A. Lassiter, "Photovoltaic Power Generation: Modeling Solar Plants' Load Levels and Their Effects on the Distribution System," in *IEEE Industry Applications Magazine*, vol. 19, no. 4, pp. 63-72, July-Aug. 2013, doi: 10.1109/MIAS.2012.2216000.
- [11] J.C. Wu and Y.H. Wang. Power conversion interface for small-capacity wind power generation system. *IET Generation, Transmission Distribution*, 8(4): 689-696, Apr 2014.

[12] X. Sun, M. Cheng, Y. Zhu and L. Xu, "Application of Electrical Variable Transmission in Wind Power Generation System," in *IEEE Transactions on Industry Applications*, vol. 49, no. 3, pp. 1299-1307, May-June 2013, doi: 10.1109/TIA.2013.2253079.

[13] Y. Duan and R. G. Harley. Present and future trends in wind turbine generation design. In *IEEE Power Electronics and Machines in Wind Applications*, pages 1-6, June 2009.

[14] J. Ribrant and L. Bertling, "Survey of failures in wind power systems with focus on Swedish wind power plants during 1997-2005," 2007 *IEEE Power Engineering Society General Meeting*, Tampa, FL, USA, 2007, pp. 1-8, doi: 10.1109/PES.2007.386112.

[15] O. Barambones, J. A. Cortajarena, P. Alkorta, J. M. Gonzalez de Durana, I. Calvo and J. A. Ramos, "Adaptive sliding mode control scheme for a wave power generation plant," 2017 *IEEE International Conference on Environment and Electrical Engineering and 2017 IEEE Industrial and Commercial Power Systems Europe (EEEIC / I&CPS Europe)*, Milan, Italy, 2017, pp. 1-6, doi: 10.1109/EEEIC.2017.7977608.

[16] T. K. A. Brekken, H. T. Ozkan-Haller and A. Simmons, "A Methodology for Large-Scale Ocean Wave Power Time-Series Generation," in *IEEE Journal of Oceanic Engineering*, vol. 37, no. 2, pp. 294-300, April 2012, doi: 10.1109/JOE.2012.2187393.

[17] A. J. Garrido, I. Garrido, M. Amundarain, M. Alberdi and M. De la Sen, "Sliding-Mode Control of Wave Power Generation Plants," in *IEEE Transactions on Industry Applications*, vol. 48, no. 6, pp. 2372-2381, Nov.-Dec. 2012, doi: 10.1109/TIA.2012.2227096.

[18] T. Bocklisch. Hybrid energy storage systems for renewable energy applications. *Energy Procedia*, 73:103-111, June 2015.

[19] F. Nejabatkhah and Y. W. Li, "Overview of Power Management Strategies of Hybrid AC/DC Microgrid," in *IEEE Transactions on Power Electronics*, vol. 30, no. 12, pp. 7072-7089, Dec. 2015, doi: 10.1109/TPEL.2014.2384999.

[20] D. A.J Rand and P.T. Moseley. Chapter 13 –energy storage with lead-acid batteries. In *Electrochemical Energy Storage for Renewable Sources and Grid Balancing*, Pages 201-222. Elsevier, Amsterdam, 2015.

[21] P. Kurzweil. Chapter 19-electrochemical double-layer capacitors. In *Electrochemical Energy Storage for Renewable Sources and Grid Balancing*, pages 345-407. Elsevier, Amsterdam, 2015.

[22] Sergio Vazquez, Srdjan M. Lukic, Eduardo Galvan, Leopoldo G. Franquelo, and Juan M. Carrasco "Energy Storage Systems for Transport and Grid Applications." *IEEE transactions on industrial electronics*, vol. 57, no. 12, december 2010.

[23] Tuohy, Aidan, Ben Kaun, and Robert Entriken. "Storage and demand-side options for integrating wind power: Demand side and storage options for integrating wind power", *Wiley Interdisciplinary Reviews Energy and Environment*, 2013.

[24] Energy Storage in Power Systems, First Edition. Francisco D'iaz-González, Andreas Sumper and Oriol Gomis-Bellmunt. 2016 *John Wiley & Sons*, Ltd.

[25] Furquan Nadeem, S. M. Suhail Hussain, Prashant Kumar Tiwari, Arup Kumar Goswami, Taha Selim Ustun. "Comparative Review of Energy Storage Systems, Their Roles and Impacts on Future Power Systems", *IEEE Access*, 2018.

[26] Salwa Elouarouar, Hicham Medromi, Fouad Moutaouakkil. "Energy Management in Multi-Rotors Unmanned Aerial Systems", 2017 *International Renewable and Sustainable Energy Conference* (IRSEC), 2017.

[27] Alireza Khaligh, Zhihao Li. "Battery, ultracapacitor, fuel cell, and hybrid energy storage systems for electric, hybrid electric, fuel cell, and plug-in hybrid electric vehicles: state of the art." *IEEE Transactions on Vehicular Technology* Vol: 59, Issue: 6, July 2010.

[28] H. Chen, T. N. Cong, W. Y., C. Tan. Y. Li, and Y. Ding. Progress in electrical energy storage system: A critical review. *Progress in Natural Sciences*, 19(3):291-312, Mar 2009.

[29] D. I Stroe, A.I. Stan, R. Diosi, R. Teodorescu, and S. J. Andreasen. Short term energy storage for grid supported in wind power applications. In *13<sup>th</sup> International conference on Optimization of Electrical and Electronic Equipment (OPTIM)*, pages 1012-1021, May 2012.

[30] H. Alloui, M. Becherif, and K. Marouani. Modelling and frequency separation energy management of fuel cell-battery hybrid sources system for hybrid electric vehicle. In *21<sup>st</sup> Mediterranean Conference on control and Automation*, pages 646-651, June 2013.

[31] F. Diaz-Gonzalez, A. Sumper, O. Gomin-Bullmunt, and R. Villafafila-Robles. A review of energy storage technologies for wind power applications. *Renewable and Sustainable Energy Reviews*, 16(4):2154-2171, May 2012.

[32] I. Hadjipaschlis A. Poullikkas, and V. Efthimiou. Overview of current and future energy storage technologies for electric power applications. *Renewable and Sustainable Energy Reviews*, 13(6): 1513-1522, Aug 2009.

[33] G. J. May, A. Davidson, and B. Monahov. Lead batteries for utility energy storage: A review. *Journal of Energy Storage*, 15 (Supplement C): 145-157, Feb 2018.

[34] A. Khaligh and Z. Li. Battery, Ultracapacitor, fuel cell, and hybrid energy storage systems for electric, hybrid electric, fuel cell, and plug-in hybrid electric vehicles: State of the art. *IEEE Transactions on Vehicular Technology*, 59(6): 2806-2814, July 2010.

[35] A. Cooper and P. Moseley, "Progress in the Development of Lead-Acid Batteries for Hybrid Electric Vehicles," 2006 *IEEE Vehicle Power and Propulsion Conference*, Windsor, UK, 2006, pp. 1-6, doi: 10.1109/VPPC.2006.364282.

[36] D. B. Edwards and C. Kinney. Advanced lead acid battery designs for hybrid electric vehicles. In *16<sup>th</sup> Annual Battery Conference on Applications and Advances*, pages 207-212, 2001.

[37] M. Saakes, R. Woortmeijer, and D. Schmal. Bipolar lead-acid battery for hybrid vehicles. *Journal of Power Sources*, 144(2): 536-545, June 2005. Selected papers from the *Ninth European Lead Battery Conference*.

[38] M. Fetcenko, J. Koch, and M. Zelinsky. Nickel-metal hydride and nickel zinc batteries for hybrid electric vehicles and battery electric vehicles. In *Advances in Battery Technologies for Electric Vehicles, Woodhead Publishing Series in Energy*, pages 103-126. Woodhead Publishing, 2015.

[39] M. A. Fetcenko, S. R. Ovshinsky, B. Reichman, K. Young, C. Fierro, J. Koch, A. Zallen, W. Mays, and T. Ouchi. Recent advances in nimh battery technology. *Journal of Power sources*, 165 (2): 544-551, Mar 2007.

[40] M.A. Hannan, M. M. Hoque, A. Mohamed, and A. Ayob. Review of energy storage systems for electric vehicle applications: Issues and challenges. *Renewable and Sustainable Energy Reviews*, 69 (Supplement C):771-789, Mar 2017.

[41] D. O. Akinyele and R. K. Rayudu. Review of energy storage technologies for sustainable power networks. *Sustainable Energy Technologies and Assessments*, 8:74-91, Dec 2014.

[42] Malhotra, A., Battke, B., Beuse, M., Stephan, A., Schmidt, T. S. (2016). Use cases for stationary battery technologies: *A review of the literature and existing projects*. *Renewable and Sustainable Energy Reviews* 56, 705-721.

[43] X. Luo, J. Wang, M. Dooner, and J. Clarke. Overview of current development in electrical energy storage technologies and the application potential in power system operation. *Applied Energy*, 137(Supplement C): 511-536, Jan 2015.

[44] X. Chen, W. Shen, T.T. Vo, Z. Cao, and A. Kapoor. An overview of lithium-ion batteries for electric vehicles. In *10<sup>th</sup> International Power Energy Conference (IPEC)*, pages 230-235, Dec 2012.

[45] Om Krishan, Sathans Suhag. "An updated review of energy storage systems: Classification and applications in distributed generation power systems incorporating renewable energy resources." *Int J Energy Res.* 2018.

[46] Acar C. "A comprehensive evaluation of energy storage options for better sustainability." *Int J Energy Res.* 2018.

[47] Salwa Elouarouar, Hicham Medromi, Fouad Moutaouakkil. "Energy Management in Multi-Rotors Unmanned Aerial Systems", 2017 *International Renewable and Sustainable Energy Conference (IRSEC)*, 2017.

[48] M. Aneke and M. Wang. Energy storage technologies and real life applications- a state of the art review. *Applied Energy*, 179 (Supplement C): 350-377, Mar 2016.

[49] H. Zhou, T. Bhattacharya, D. Tran, T. S. T. Siew and A. M. Khambadkone, "Composite Energy Storage System Involving Battery and Ultracapacitor With Dynamic Energy Management in Microgrid Applications," in *IEEE Transactions on Power Electronics*, vol. 26, no. 3, pp. 923-930, March 2011, doi: 10.1109/TPEL.2010.2095040.

[50] T. Christen and M. W. Carlen. Theory of ragone plots. *Journal of power sources*, 91(2): 210-216, Dec 2000.

[51] O. Laldin, M. Moshirvaziri and O. Trescases, "Predictive Algorithm for Optimizing Power Flow in Hybrid Ultracapacitor/Battery Storage Systems for Light Electric Vehicles," in *IEEE Transactions on Power Electronics*, vol. 28, no. 8, pp. 3882-3895, Aug. 2013, doi: 10.1109/TPEL.2012.2226474.

[52] W. Jing, C. Hung Lai, S.H.W. Wong, and M. L.D. Wong. Battery-supercapacitor hybrid energy storage system in standalone dc microgrids: a review. *IET Renewable Power Generation*, 11(4):461-469, 2017.

[53] H. Zhou, T. Bhattacharya, D. Tran, T. S. T. Siew and A. M. Khambadkone, "Composite Energy Storage System Involving Battery and Ultracapacitor With Dynamic Energy Management in Microgrid Applications," in *IEEE Transactions on Power Electronics*, vol. 26, no. 3, pp. 923-930, March 2011, doi: 10.1109/TPEL.2010.2095040.

[54] R. Sathishkumar, S. K. Kollimalla and M. K. Mishra, "Dynamic energy management of micro grids using battery super capacitor combined storage," 2012 Annual *IEEE India Conference (INDICON)*, Kochi, India, 2012, pp. 1078-1083, doi: 10.1109/INDCON.2012.6420777.

[55] S.K. Kollimalla, A. Ukil, G. H. Beng, U. Manandhar and N. R. Tummuru, "Optimization of charge/discharge rates of a battery using a two stage rate-limit control," 2017 *IEEE Power & Energy Society General Meeting*, Chicago, IL, USA, 2017, pp. 1-1, doi: 10.1109/PESGM.2017.8273807.

[56] B. Hredzak, V. G. Agelidis and M. Jang, "A Model Predictive Control System for a Hybrid Battery-Ultracapacitor Power Source," in *IEEE Transactions on Power Electronics*, vol. 29, no. 3, pp. 1469-1479, March 2014, doi: 10.1109/TPEL.2013.2262003.

[57] X. Feng, H. B. Gooi and S. X. Chen, "Hybrid Energy Storage With Multimode Fuzzy Power Allocator for PV Systems," in *IEEE Transactions on Sustainable Energy*, vol. 5, no. 2, pp. 389-397, April 2014, doi: 10.1109/TSTE.2013.2290543.

[58] H. Yin, W. Zhou, M. Li, C. Ma and C. Zhao, "An Adaptive Fuzzy Logic-Based Energy Management Strategy on Battery/Ultracapacitor Hybrid Electric Vehicles," in *IEEE Transactions on Transportation Electrification*, vol. 2, no. 3, pp. 300-311, Sept. 2016, doi: 10.1109/TTE.2016.2552721.

[59] Torreglosa J.P., Garcia P., Fernandez L.M., Jurado F. "Predictive control for the energy management of a fuel-cell–battery–supercapacitor tramway". *IEEE Transactions on Industrial Informatics*, 2014. 10. pp. 276-285.

[60] Bhomik P, Chandak S, Rout P K, State of Charge and State of Power Management in a Hybrid Energy Storage Systems by the Self-tuned Dynamic Exponent and the

Fuzzy-Based Dynamic PI Controller. *Int Trans Electr Energ Syst.* 2019; e2848, doi; 10.1002/2050-7038.2848.

[61] C. Zhao, S.D Road and J.W. Kolar, “ An Isolated Three-Port Bidirectional DC-DC Converter With Decoupled Power Flow Management,” in *IEEE Transactions on Power Electronics*, vol.23,no.5,pp.2443-2453,Sept. 2008.

[62] J. Zeng, W. Qiao, L.Qu and Y. Jiao,” An Isolated Multiport DC-DC Converter for Simultaneous Power Management of Multiple Different Renewable Energy Sources,” in *IEEE Journal of Emerging and selected Topics in Power Electronics*, vol.2,no.1,pp.70-78,March 2014.

[63] Yifeng Wang, Fuqiang Han, Liang Yang, Rong xu, Ruixin liu, “A Three-Port Bidirectional Multi-Element Resonant Converter With Decoupled Power Flow Management for Hybrid Energy Storage Systems” *IEEE Access* volume 6, November 2018.

[64] P. Yang, C. K. Tse, J.Xu and G. Zhou, “Synthesis and Analysis of Double-Input Single-Output DC/DC Converter,” in *IEEE Transaction on Industrial Electronics*, vol. 62, no.10,pp.6284-6295,Oct.2015.

[65] A. Khaligh, J. Cao and Y. J. Lee, “A Multiple-Input DC-DC Converter Topology,” in *IEEE Transactions on Power Electronics*, vol. 24, no. 3, pp. 862-868, March 2009.

[66] Benfei Wang, Liang Xian, Ujjal Manandhar, Jian Ye, Xinan Zhang, Hoay Beng Gooi, Abhisek ukil, “Hybrid energy storage system using bidirectional single-inductor multipleport converter with model predictive control in DC microgrids” *Electric Power Systems Research*, 173 (April-2019),38-47.

[67] Rasoul Faraji, Hosein Farzanehfard,” Soft-switching Nonisolated High step-up three-port DC-DC converter for Hybrid energy systems” *IEEE Transactions on Power Electronics*.vol.33, Dec-2018.

[68] Yusuke Sato, Masatoshi Uno, Hikaru Nagata, “Nonisolated Multiport Converters Based on Integration of PWM Converter and Phase-Shift-Switched Capacitor Converter” *IEEE Transactions on Power Electronics*, vol.35, no.1 January 2020.

[69] Zhehan Yi, Wanxin Dong, Amir H. Etemadi, “A Unified Control and Power Management Scheme for PV-Battery-Based Hybrid Microgrids for Both Grid-Connected and Islanded Modes,” *IEEE Transactions on Smart grid*, vol.9, no.6, November 2018.

[70] H. Behjati and A. Davoudi," Power Budgeting Between Diversified Energy Sources and Loads Using a Multiple-Input Multiple-Output DC-DC Converter," in *IEEE Transactions on Industry Applications*, vol.49,no.6,pp. 2761-2772, Nov-Dec.2013.

[71] K.Filsoof and P. W. Lehn, " A Bidirectional Multiple-Input Multiple-Output Modular Multilevel DC-DC Converter and its Control Design," in *IEEE Transactions on Power Electronics*, vol.31,no.4,pp.2767-2779, April 2016.

[72] R. J. Wai, C. Y. Lin and B. H. Chen, "High-Efficiency DC-DC Converter With Two Input Power Sources," in *IEEE Transactions on power Electronics*, vol.27,no.4,pp.1862-1875,April 2012

[73] F. Nejabatkhah, S. Danyali, S.H. Hosseini, M. Sabahi and S. M. Niapour, "Modeling and Control of a New Three-Input DC-DC Boost Converter for Hybrid PV/FC/Battery Power System," in *IEEE Transactions on Power Electronics*, vol. 27, no. 5, pp. 2309-2324, May 2012.

[74] R. J. Wai B. H. Chen, "High-Efficiency Dual-Input Interleaved DC-DC Converter for Reversible Power Sources," in *IEEE Transactions on Power Electronics*, vol.29,no. 6,pp.2903-2921, June 2014.

[75] C. W. Chen, C. Y. Liao, K.H. Chen and Y. M. Chen, "Modeling and Controller Design of a Semiisolated Multiinput Converter for a Hybrid PV/Wind Power Charger System," in *IEEE Transactions on Power Electronics*, vol. 30, no. 9, pp. 4843-4853, Sept. 2015.

[76] S. Danyali, S. H. Hosseini and G. B. Gharehpetian, " New Extendable Single-Stage Multi-input DC-DC/AC Boost Converter," in *IEEE Transactions on Power Electronics*, vol. 29, no. 2, pp. 775-788, Feb. 2014.

[77] F. Guo, L. Fu, X. Zhang, C. Yao, H. Li and J. Wang, " A Family of Quasi-Switched-Capacitor Circuit-Based Dual-Input DC/DC Converters for Photovoltaic Systems Integrated With Battery Energy Storage," in *IEEE Transactions on Power Electronics*, vol. 31, no. 12, pp. 8237-8246, Dec. 2016.

[78] K. Gummi and M. Ferdowsi, " Double-Input DC-DC Power Electronic Converters for Electric-Drive Vehicles—Topology Exploration and Synthesis Using a Single-Pole Triple-Throw Switch," in *IEEE Transactions on Industrial Electronics*, vol. 57, no. 2, pp. 617-623.Feb.2010.

[79] R. R. Ahrabi, H. Ardi, M. Elmi and A. Ajami, "A Novel Step-Up Multiinput DC–DC Converter for Hybrid Electric Vehicles Application," in *IEEE Transactions on Power Electronics*, vol. 32, no. 5, pp. 3549-3561, May 2017.

[80] F. Akar, Y. Tavlasoglu, E. Ugur, B. Vural and I. Aksoy, "A Bidirectional Nonisolated Multi-Input DC–DC Converter for Hybrid Energy Storage Systems in Electric Vehicles," in *IEEE Transactions on Vehicular Technology*, vol. 65, no. 10, pp. 7944-7955, Oct. 2016.

[81] A. Nahavandi, M. T. Hagh, M.B. B. Sharifian and S. Danyali," A Nonisolated Multiinput Multioutput DC–DC Boost Converter for Electric Vehicle Applications," in *IEEE Transactions on Power Electronics*, vol. 30, no. 4, pp. 1818-1835, April 2015.

[82] Rezzak. D and Boudjerda. N (2016), Management and Control Strategy of a hybrid energy source fuel cell/supercapacitor in electric vehicles, *Int Trans Electr Energ Syst*, doi;10.1002/etep.2308.

[83] Babaei E, Saadatizadesh Z, Ranjbarizad V. "A new non isolated bidirectional DC–DC converter with ripple-free Input current at low-voltage side and high conversion ratio", *Int Trans Electr Energ Syst*. 2017; e2494. Doi; 10.1002/etep.2494.

[84] Suresh K, Chellammal N, Bharatiraja C, Sanjeevikumar P, Blaabjerg F, Nielsen JBH," Cost-efficient nonisolated three-port DC-DC converter for EV/HEV applications with energy storage", *Int Trans Electr Energ Syst*.2019; e12008,doi;10.1002/2050-7038.120088.

[85] Predictive Control of Power Converters and Electrical Drives by Jose Rodriguez and Patricio Cortes.

[86] B. Hredzak, V. G. Agelidis and M. Jang, "A Model Predictive Control System for a Hybrid Battery-Ultracapacitor Power Source," in *IEEE Transactions on Power Electronics*, vol. 29, no. 3, pp. 1469-1479, March 2014, doi: 10.1109/TPEL.2013.2262003.

[87] Amin, R. T. Bambang, A. S. Rohman, C. J. Dronkers, R. Ortega and A. Sasongko, "Energy Management of Fuel Cell/Battery/Supercapacitor Hybrid Power Sources Using Model Predictive Control," in *IEEE Transactions on Industrial Informatics*, vol. 10, no. 4, pp. 1992-2002, Nov. 2014, doi: 10.1109/TII.2014.2333873.

[88] Ahmad Dehghanzadeh, Gholamreza Farahani, Hani Vahedi, Kamal AI-Haddad, " Model predictive control design for DC-DC converters applied to a photovoltaic

systems" *International Journal of Electrical Power & Energy Systems*, Volume 103,2018, pages 537-544, ISSN 0142-0615.

[89] S. Chen, Q. Yang, J. Zhou and X. Chen, "Hybrid energy storage system control method based on model predictive control," in *CSEE Journal of Power and Energy Systems*, doi: 10.17775/CSEEJPES.2019.01960.

[90] Y. Mei, X. Li and Y. Qi, "A model predictive control method for three-level bi-directional DC-DC converter in renewable generation system," 2015 *18th International Conference on Electrical Machines and Systems (ICEMS)*, Pattaya, Thailand, 2015, pp. 417-421, doi: 10.1109/ICEMS.2015.7385070.

[91] Y. Shan, J. Hu, K. W. Chan, Q. Fu and J. M. Guerrero, "Model Predictive Control of Bidirectional DC-DC Converters and AC/DC Interlinking Converters—A New Control Method for PV-Wind-Battery Microgrids," in *IEEE Transactions on Sustainable Energy*, vol. 10, no. 4, pp. 1823-1833, Oct. 2019, doi: 10.1109/TSTE.2018.2873390.

[92] D. E. Quevedo, R. P. Aguilera, M. A. Perez, P. Cortes and R. Lizana, "Model Predictive Control of an AFE Rectifier With Dynamic References," in *IEEE Transactions on Power Electronics*, vol. 27, no. 7, pp. 3128-3136, July 2012, doi: 10.1109/TPEL.2011.2179672.

[93] M. C. Joshi and S. Samanta, "Improved Energy Management Algorithm With Time-Share-Based Ultracapacitor Charging/Discharging for Hybrid Energy Storage System," in *IEEE Transactions on Industrial Electronics*, vol. 66, no. 8, pp. 6032-6043, Aug. 2019, doi: 10.1109/TIE.2018.2871799.

[94] M. C. Joshi and S. Samanta, "Modified Ultracapacitor Voltage Control Loop for Battery/UC HESS," 2018 *IEEE International Conference on Power Electronics, Drives and Energy Systems (PEDES)*, Chennai, India, 2018, pp. 1-5, doi: 10.1109/PEDES.2018.8707721.

[95] C. R. Lashway and O. A. Mohammed, "Adaptive Battery Management and Parameter Estimation Through Physics-Based Modeling and Experimental Verification," in *IEEE Transactions on Transportation Electrification*, vol. 2, no. 4, pp. 454-464, Dec. 2016, doi: 10.1109/TTE.2016.2558843.

[96] S. Tian, M. Hong and M. Ouyang, "An Experimental Study and Nonlinear Modeling of Discharge I-V Behavior of Valve-Regulated Lead-Acid Batteries," in *IEEE*

*Transactions on Energy Conversion*, vol. 24, no. 2, pp. 452-458, June 2009, doi: 10.1109/TEC.2008.2001447.

[97] G. Aurilio et al., "A battery equivalent-circuit model and an advanced technique for parameter estimation," 2015 *IEEE International Instrumentation and Measurement Technology Conference (I2MTC) Proceedings*, Pisa, Italy, 2015, pp. 1705-1710, doi: 10.1109/I2MTC.2015.7151537.

[98] O. Tremblay, L. Dessaint and A. Dekkiche, "A Generic Battery Model for the Dynamic Simulation of Hybrid Electric Vehicles," 2007 *IEEE Vehicle Power and Propulsion Conference*, Arlington, TX, USA, 2007, pp. 284-289, doi: 10.1109/VPPC.2007.4544139.

[99] C. Zhu, X. Li, R. Lu, J. Xu and G. Fan, "A comparative study of three electrochemical battery models with different operating conditions," 2017 *IEEE Transportation Electrification Conference and Expo, Asia-Pacific (ITEC Asia-Pacific)*, Harbin, 2017, pp. 1-7, doi: 10.1109/ITEC-AP.2017.8080786.

[100] Om Krishan, Sathans Suhag. "An updated review of energy storage systems: Classification and applications in distributed generation power systems incorporating renewable energy resources." *Int J Energy Res.* 2018.

[101] Acar C. "A comprehensive evaluation of energy storage options for better sustainability." *Int J Energy Res.* 2018.

[102] S. Buller, E. E. Karden, D. Kok and R. W. De Doncker, "Modeling the dynamic behavior of supercapacitors using impedance spectroscopy," in *IEEE Transactions on Industry Applications*, vol. 38, no. 6, pp. 1622-1626, Nov.-Dec. 2002, doi: 10.1109/TIA.2002.804762.

[103] L. Shi and M. L. Crow, "Comparison of ultracapacitor electric circuit models," 2008 *IEEE Power and Energy Society General Meeting - Conversion and Delivery of Electrical Energy in the 21st Century*, Pittsburgh, PA, USA, 2008, pp. 1-6, doi: 10.1109/PES.2008.4596576.

[104] M. Andriollo , M. Caramanna and A. Tortella, "Equivalent circuit models for the analysis of a commercial ultracapacitor module," 2016 *AEIT International Annual Conference (AEIT)*, Capri, 2016, pp. 1-6, doi: 10.23919/AEIT.2016.7892757.

[105] C. Farcas, D. Petreus, I. Ciocan, and N. Palaghita. "Modelling and simulation of Supercapacitors" In *International Symposium for Design and Technology of Electronics Packages (SIITME)*, pages 195-200, Sept 2009.

[106] M. A. Abdullah, A. H. M. Yatim, C. W. Tan and A. S. Samosir, " Control of a bidirectional converter to interface ultracapacitor with renewable energy sources," *2013 IEEE International Conference on Industrial Technology (ICIT)*, Cape Town, South Africa, 2013, pp. 673-678, doi: 10.1109/ICIT.2013.6505752.

[107] Junhong Zhang, Jih-Sheng Lai and Wensong Yu, "Bidirectional DC-DC converter modeling and unified controller with digital implementation," *2008 Twenty-Third Annual IEEE Applied Power Electronics Conference and Exposition*, Austin, TX, USA, 2008, pp. 1747-1753, doi: 10.1109/APEC.2008.4522963.

[108] M. Fu, D. Zhang and T. Li, "Design and Analysis of a Conductance Compensator for Keeping Constant Bandwidth and Output Impedance in Average Current Mode Control," in *IEEE Transactions on Power Electronics*, vol. 32, no. 1, pp. 837-848, Jan. 2017, doi: 10.1109/TPEL.2016.2536691.

[109] Slah F, Mansour A, Hajar M, Faouzi B (2017) Analysis, modelling and implementation of an interleaved boost DC-DC converter for fuel cell used in electric vehicle. *Int J Hydrogen Energy* 42(48): 28852-28864.

[110] Y. Jin, J. Xu, G. Zhou and Changbao Mi, "Small-signal modeling and analysis of improved digital peak current control of boost converter," *2009 IEEE 6th International Power Electronics and Motion Control Conference*, Wuhan, China, 2009, pp. 326-330, doi: 10.1109/IPEMC.2009.5157407.

[111] J. Xiao, P. Wang and L. Setyawan, " Implementation of Multipl-Slack-Terminal DC Microgrids for Smooth Transitions Between Grid-Tied and Islanded States," in *IEEE Transactions on Smart Grid*, vol. 7, no. 1, pp. 273-281, Jan. 2016, doi: 10.1109/TSG.2015.2445834.

[112] M. karbalaye Zadeh, R. Gavagsaz-Ghoachani, S. Pierfederici, B. Nahid-Mobarakeh and M. Molinas, "Stability Analysis and Dynamic Performance Evaluation of a Power Electronics-Based DC Distribution System With Active Stabilizer," in *IEEE Journal of Emerging and Selected Topics in Power Electronics*, vol. 4, no. 1, pp. 93-102, March 2016, doi: 10.1109/JESTPE.2015.2484218.

[113] A. Hintz, U. R. Prasanna and K. Rajashekara, "Novel Modular Multiple-Input Bidirectional DC-DC Power Converter (MIPC) for HEV/FCV Application," in *IEEE Transactions on Industrial Electronics*, vol. 62, no. 5, pp. 3163-3172, May 2015, doi: 10.1109/TIE.2014.2371778.

- [114] R. W. Erickson and D. Maksimovic. Fundamentals of power electronics. Springer Science and Business Media, 2007.
- [115] S. Prasanth, U. B. Manthati, V. S. P. and S. Punna, "Efficient Interleaved Buck Converter Driver for LED Applications," 2019 *IEEE International Conference on Sustainable Energy Technologies and Systems (ICSETS)*, Bhubaneswar, India, 2019, pp. 206-212, doi: 10.1109/ICSETS.2019.8744943.
- [116] P. Karamanakos, T. Geyer and S. Manias, "Direct Model Predictive Current Control Strategy of DC-DC Boost Converters," in *IEEE Journal of Emerging and Selected Topics in Power Electronics*, vol. 1, no. 4, pp. 337-346, Dec. 2013, doi: 10.1109/JESTPE.2013.2279855.
- [117] P. Karamanakos, T. Geyer and S. Manias, "Direct Voltage Control of DC-DC Boost Converters Using Enumeration-Based Model Predictive Control," in *IEEE Transactions on Power Electronics*, vol. 29, no. 2, pp. 968-978, Feb. 2014, doi: 10.1109/TPEL.2013.2256370.
- [118] S. Vazquez, J. Rodriguez, M. Rivera, L. G. Franquelo and M. Norambuena, "Model Predictive Control for Power Converters and Drives: Advances and Trends," in *IEEE Transactions on Industrial Electronics*, vol. 64, no. 2, pp. 935-947, Feb. 2017, doi: 10.1109/TIE.2016.2625238.
- [119] A. Pirooz and R. Noroozian, "Model predictive control of classic bidirectional DC-DC converter for battery applications," 2016 *7th Power Electronics and Drive Systems Technologies Conference (PEDSTC)*, Tehran, Iran, 2016, pp. 517-522, doi: 10.1109/PEDSTC.2016.7556914.
- [120] B. Wang, L. Xian, V. R. K. Kanamarlapudi, K. J. Tseng, A. Ukil and H. B. Gooi, "A Digital Method of Power-Sharing and Cross-Regulation Suppression for Single-Inductor Multiple-Input Multiple-Output DC-DC Converter," in *IEEE Transactions on Industrial Electronics*, vol. 64, no. 4, pp. 2836-2847, April 2017, doi: 10.1109/TIE.2016.2631438.
- [121] D. E. Quevedo, R. P. Aguilera, M. A. Perez, P. Cortes and R. Lizana, "Model Predictive Control of an AFE Rectifier With Dynamic References," in *IEEE Transactions on Power Electronics*, vol. 27, no. 7, pp. 3128-3136, July 2012, doi: 10.1109/TPEL.2011.2179672.

## Publications

### Journals Published:

- [1] Punna Srinivas and Udaya Bhasker Manthati "**Optimum design and analysis of a dynamic energy management scheme for HESS in renewable power generation applications.**" *SN Applied Sciences* 2.3 (2020): 1-13. doi.org/10.1007/s42452-020-2313-3
- [2] Punna Srinivas and Udaya Bhasker Manthati "**Modelling of a Double-Input Bidirectional DC-DC Converter for HESS and Unified Controller Design for DC Microgrid Applications**", to the *International Journal of Power and Energy, ACTA Press*, Canada, volume 40, issue 3,2020. <http://dx.doi.org/10.2316/J.2020.203-0196>
- [3] Punna Srinivas, Udaya Bhasker Manthati and Arunkumar C R "**Modelling, Analysis and Control of a Two-Input Bidirectional DC-DC Converter for HESS in DC Microgrid Applications**", to the *International Transaction on Electrical Energy Systems (ITEES-20-0960)*, Wiley Publications. <https://doi.org/10.1002/2050-7038.12774>
- [4] Punna Srinivas, Udaya Bhasker Manthati "**FOPID Controller for Multiple input Bidirectional DC-DC Converter for DC Microgrid Applications**" *Journal of Advanced Research in Dynamical Control Systems (JARDCS)*, USA. volume.10,2018

### Book Chapters:

- [1] Punna Srinivas, Udaya Bhasker Manthati and Arunkumar C R "**A Comparative Analysis of PI and Predictive Control Strategy for HESS Based Bi-Directional DC-DC Converter for DC Microgrid Applications**". *Lecture Notes in Electrical Engineering*, Springer Publisher, 2021.

## **Curriculum-Vitae**

Name : Punna Srinivas.

Date of birth : 30-09-1983.

Gender : Male

Contact number : +91 9985772071

Email id : [srinu240@gmail.com](mailto:srinu240@gmail.com)

### **Fellowships:**

1. MHRD fellowship for Doctoral Study at National Institute of Technology, Warangal
2. MHRD fellowship for Masters Study at National Institute of Technology, Warangal

### **Educational Qualifications:**

Examination	Discipline/ Specialization	School /College	Board/ University	Year of Passing	Percentage/ CGPA
M.Tech	Power Electronics and Drives	National Institute of Technology, Warangal.	NIT, Warangal	2009	75.20
B.Tech	Electrical & Electronics Engineering	H R D engineering college, Devarakonda.	J.N.T.U., Hyderabad.	2006	65.42